Cryo-EM resolution of immunoreceptor-pathogen effector interfaces for engineering enhanced disease resistance in crops

Inaugural-Dissertation

zur

Erlangung des Doktorgrades

der Mathematisch-Naturwissenschaftlichen

Fakultät der Universität zu Köln

vorgelegt von

Aaron W. Lawson

aus Edmonton, Kanada

Berichterstatter: Prof. Dr. Paul Schulze-Lefert
(Gutachter)

Prof. Dr. Jane Parker

Tag der mündlichen Prüfung: 07.11.2024

Cryo-EM resolution of immunoreceptor-pathogen effector interfaces for engineering enhanced disease resistance in crops

Inaugural dissertation for the award of the doctoral degree
from the Faculty of Mathematics and Natural Sciences
of the University of Cologne, Germany

Submitted by
Aaron W. Lawson
from Edmonton, Canada

First Reviewer: Prof. Dr. Paul Schulze-Lefert
Second reviewer: Prof. Dr. Jane Parker
Chair: Prof. Dr. Alga Zuccaro
Minute taker: Dr. Charles Copeland
Date of examination: 07.11.2024

The following work was carried out in the lab of Prof. Dr. Paul Schulze-Lefert at the Max Planck Institute for Plant Breeding Research, Department of Plant-Microbe Interactions, Cologne, Germany

Table of contents

Authorship contributions related to this thesis……..4

General abstract (English)……...5

General abstract (German)……..6

General introduction……..7

Chapter 1: A wheat resistosome defines common principles of immune receptor channels……11

Chapter 2: The barley MLA13-AVR$_{A13}$ heterodimer reveals principles for immunoreceptor recognition of RNase-like powdery mildew effectors……12

Chapter 3: A versatile protocol for purifying recombinant protein from *Nicotiana benthamiana*……13

General discussion……..14

References……17

Acknowledgments……21

Authorship contributions related to this thesis

Lawson, A. W. *et al*. A versatile protocol for purifying recombinant proteins from *Nicotiana benthamiana*. (to be uploaded on bioRxiv and submitted for peer review).

Lawson, A. W. *et al*. The barley MLA13-AVR_{A13} heterodimer reveals principles for immunoreceptor recognition of RNase-like powdery mildew effectors. bioRxiv, 2024.2007.2014.603419 (2024). https://doi.org/10.1101/2024.07.14.603419

Ma, S., An, C., **Lawson, A.W.** *et al*. Oligomerization-mediated autoinhibition and cofactor binding of a plant NLR. Nature (2024). https://doi.org/10.1038/s41586-024-07668-7

Cao, Y., Kümmel, F., Logemann, E., Gebauer, J., **Lawson, A.W.** *et al*. Structural polymorphisms within a common powdery mildew effector scaffold as a driver of coevolution with cereal immune receptors. Proceedings of the National Academy of Sciences 120 (2023). https://doi.org/10.1073/pnas.2307604120

Förderer, A., Li, E., **Lawson, A.W.** *et al*. A wheat resistosome defines common principles of immune receptor channels. Nature 610, 532-539 (2022). https://doi.org/10.1038/s41586-022-05231-w

Lawson, A.W. and Li, E. Structure of wheat immune receptor helps guide design of disease resistant varieties Nature (2022) https://doi.org/10.1038/10.1038/, d41586-022-02262-1

Müller, M. C., Kunz, L., Schudel, S., **Lawson, A.W.** *et al*. Ancient variation of the *AvrPm17* gene in powdery mildew limits the effectiveness of the introgressed rye *Pm17* resistance gene in wheat. Proceedings of the National Academy of Sciences 119, e2108808119 (2022). https://doi.org/doi:10.1073/pnas.2108808119

Saur, I. M. L., **Lawson, A. W.** & Schulze-Lefert, P. Buy one, get two. Nature Plants 8, 100-101 (2022). https://doi.org/10.1038/s41477-022-01097-y

General abstract (English)

Co-evolution between plants and pathogenic microbes leads to adaptive genetic changes that shape the development of the host immune system. A major component of plant innate immunity is the deployment of nucleotide-binding leucine-rich repeat receptors (NLRs) with N-terminal coiled-coil domains (CNLs). Grass species including wheat and barley encode CNLs that detect pathogenic effector proteins, an interaction that results in a potent hypersensitive response (HR) that is associated with effector-triggered immunity (ETI). ETI can be evaded due to sequence alterations in virulent effectors to escape detection by their cognate CNLs. The molecular basis of receptor-effector interaction specificity is incompletely understood. In this thesis, I present the cryogenic electron microscopy (cryo-EM) structure of the wheat Sr35 CNL in complex with its matching effector AvrSr35 from *Puccinia graminis* f sp *tritici* (*Pgt*) as the first structure of an activated NLR heterocomplex from a crop species. In addition, I report the cryo-EM structure of the barley CNL MLA13 in complex with its cognate effector AVR_{A13}-1 from *Blumeria graminis*. I demonstrate that structural elucidation of CNLs in complex with their cognate effectors, and investigation of the interface between the two, can guide the rational design of CNLs to broaden effector recognition specificity. To this end, I have developed and present here a versatile and robust protocol for the purification of proteins from leaves of *Nicotiana benthamiana*, which has been successfully applied to a range of proteins and structural studies. Taken together, I show that experimentally resolved receptor-effector structures remain indispensable for understanding crop-pathogen interactions and aiding the design of NLRs with expanded effector recognition capability to enhance resistance to crop diseases.

General abstract (German)

Die Koevolution zwischen Pflanzen und pathogenen Mikroben führt zu adaptiven genetischen Veränderungen, die die Entwicklung des Immunsystems des Wirts prägen. Ein Hauptbestandteil der angeborenen Immunität von Pflanzen ist der Einsatz von Rezeptoren mit Nukleotid-bindenden Leucin-reichen Wiederholungen (NLRs) mit N-terminalen coiled-coil-Domänen (CNLs). Grasarten wie Weizen und Gerste kodieren für CNLs, die pathogene Effektorproteine erkennen. Diese Interaktion führt zu einer starken Hypersensitivitätsreaktion (HR), die mit der Effektorausgelösten Immunität (ETI) assoziiert ist. ETI kann durch Sequenzänderungen in virulenten Effektoren umgangen werden, um der Erkennung durch ihre entsprechenden CNLs zu entgehen. Die molekulare Basis der Spezifität der Rezeptor-Effektor-Interaktion ist unvollständig verstanden. In dieser Dissertation präsentiere ich die Struktur der Weizen-Sr35 CNL im Komplex mit ihrem passenden Effektor AvrSr35 von *Puccinia graminis* f sp *tritici* (*Pgt*) mittels Kryo-Elektronenmikroskopie (cryo-EM) als die erste Struktur eines aktivierten NLR-Heterokomplexes aus einer Nutzpflanze. Darüber hinaus berichte ich über die Cryo-EM-Struktur der Gerste-CNL MLA13 im Komplex mit ihrem entsprechenden Effektor AVR_{A13}-1 von *Blumeria graminis*. Ich zeige, dass die strukturelle Aufklärung von CNLs im Komplex mit ihren entsprechenden Effektoren und die Untersuchung der Schnittstelle zwischen beiden die rationale Gestaltung von CNLs zur Erweiterung der Erkennungsspezifität von Effektoren leiten kann. Zu diesem Zweck habe ich ein vielseitiges und robustes Protokoll für die Reinigung von Proteinen aus Blättern von *Nicotiana benthamiana* entwickelt und präsentiere es hier, das erfolgreich auf eine Reihe von Proteinen und strukturellen Studien angewendet wurde. Zusammenfassend zeige ich, dass experimentell aufgeklärte Rezeptor-Effektor-Strukturen unverzichtbar bleiben, um Pflanzen-Pathogen-Interaktionen zu verstehen und die Entwicklung von NLRs mit erweiterter Effektorerkennungskapazität zur Verbesserung der Widerstandsfähigkeit gegen Pflanzenkrankheiten zu unterstützen.

General introduction

Plant immunity to pathogenic microbes is largely reliant on the detection of pathogen-associated molecular patters (PAMPs) and pathogen-derived effector proteins. PAMP-triggered immunity (PTI) is primarily mediated by the perception of PAMPS such as fungi-derived chitin or bacteria-derived peptide flg22 by pattern recognition receptors (PRRs) at the cell surface, often leading to the host production of toxic reactive oxygen species (ROSs)[1,2]. PTI also engages an additional branch of immunity that includes the deployment of intracellular nucleotide-binding leucine-rich repeat (NLR) immunoreceptors to detect and counter pathogens[3]. Plant NLRs contain a modular architecture and are categorised according to their N-terminal coiled-coil (CC; CNLs) domain or Toll-Interleukin-1 Receptor (TIR; TNLs) domain[4]. Conserved modules among the two classes include a central nucleotide binding domain (NBD) and a C-terminal leucine-rich repeat (LRR) domain[4]. It is the LRR domain that typically interacts with cognate pathogen-derived effector proteins (AVRs) and/or their pathogen-modified virulence targets, resulting in a downstream immune response that is often characterised by a localised cell death and restriction of pathogen growth, generally referred to as effector triggered immunity (ETI)[1,5]. In some cases, these so called 'sensor NLRs' also contain an integrated domain (ID) that is believed to resemble the virulence target of effectors, a molecular mimicry capable of triggering an immune response upon effector detection[6]. Some sensor CNLs and TNLs signal through downstream 'helper NLRs' that contain a HeLo-/RPW8-like domain or a CC domain at the N-terminus and act as pairs to confer immunity with the helper NLRs executing a cell death response[7-9].

Oligomerisation of high order heterocomplexes is a hallmark of NLR autoinhibition, activation and immunostimulatory output[10-13]. Resolution of the cryogenic electron microscopy (cryo-EM) structure of the *Arabidopsis thaliana* CNL ZAR1 resistosome provided the first example of how oligomerisation of plant NLRs leads to ETI[10]. The bacterial pathogen *Xanthomonas campestri*s pv *campestris* (*Xcc*) delivers the uridylytransferase effector AvrAC into the into the host cell resulting in the uridylation of its virulence target PBS1-like protein 2 (PBL2). A preformed complex comprising ZAR1 and resistance-related kinase 1 (RKS1) binds to $PBL2^{UMP}$ resulting in the exchange of ADP to ATP in the NBD and oligomerisation of a wheel-like pentamer[10,14]. Evidence suggests that at least one function of the ZAR1 resistosome is localisation at the plasma membrane where it acts as a nonselective Ca^{2+} channel suspected to contribute to cell death[15]. The helper NLR required for cell death 4 (NRC4) exhibits similar oligomerisation tendencies albeit in a hexameric conformation rather than the pentameric ZAR1 resistosome[13]. In this case, the sensor NLR Bs2 detects the bacterial pathogen effector AvrBs2, triggering the oligomerisation of an NRC4 hexamer which executes the cell death response[13]. Conversely, the homologous NRC2 was found to oligomerise as dimers, tetramers and filaments as an autoinhibitory conformation and sequestration of the cell death-inducing receptors[16]. The cryo-EM structures of the *N. benthamiana* ROQ1 and *A. thaliana* RPP1 resistosomes reveal that effector-triggered TNLs also oligomerise to form tetramers with NADase activity[11,12]. Although oligomerisation seems to be a common theme of NLRs activity, it is curious to consider alternative NLR conformations since the discovery of hexamers and autoinhibitory states.

Detection of pathogen effectors or effector-modified host molecules remains central to the efficacy of NLRs and host resistance to devastating diseases[1,5]. Revealing how NLRs interact with and are triggered by pathogen effectors broadens our understanding of co-evolutionary processes and can assist in the rational design

of NLRs for broad spectrum resistance through genetic engineering. A prime pathosystem for studying such interactions is stem rust of wheat caused by the obligate biotroph and basidiomycete *Puccinia graminis* f sp *tritici* (*Pgt*). Wheat stem rust is a globally devastating disease, in particular due to the emergence and spread of the highly virulent *Pgt* race Ug99 which is capable of overcoming many of the over 36 characterised (*Sr*) resistance genes widely deployed by conventional breeding programmes[17,18]. Among several classes of proteins, *Sr* genes encode NLRs that detect *Pgt*-derived AvrSrs and trigger ETI[18]. For example, the CNL Sr27 recognises the Zn^{2+}-bound effector AvrSr27 and two structural homologs[19,20]. While the crystal structure of AvrSr27 is available, and evidence suggests the N terminal domain of the effector is responsible for interaction with Sr27, structural information from the interface between the two is lacking[20]. The crystal structure of AvrSr50 exemplifies structural diversity among Sr-recognised effectors with highest similarity to cupin superfamily members and carbohydrate hydrolases[21]. Similar to AvrSr27, identification of key residues believed to contribute to the Sr50-AvrSr50 interaction have been identified, however, structural resolution of the interface remains incomplete[21]. The only other AvrSrs characterised to date include AvrSr35, AvrSr13 and AvrSr22, all of which are predicted to be structurally dissimilar[22,23].

Barley-powdery mildew interactions also present ample opportunity to investigate effector recognition specificity by CNLs. The ascomycete *Blumeria graminis* shares the same biotrophic lifestyle as *Pgt* although infects barley leaves and delivers effectors into the host cell, a strategy presumed to promote virulence[24]. A single *Bg* strain encodes >600 effectors and is capable of delivering hundreds into a host cell during infection, the majority of which are predicted to exhibit a conserved RNase-like fold[24]. The pathogen is countered by the allelic series of *Mildew locus a* (*Mla*) genes which were first isolated from wild barley relatives and have historically been introgressed into domesticated barley lines to confer strain-specific disease resistance to *Bg*[25]. *Mla*s encode CNLs containing >90% amino acid sequence similarity with the majority of polymorphisms existing in the LRR, a diversification believed to be the product of co-evolutionary pressures between wild barley and *Bg*[25]. To date seven *Bg* AVR_As have been characterised including AVR_{A1}, AVR_{A6}, AVR_{A7}, AVR_{A9}, AVR_{A10}, AVR_{A13}, AVR_{A22}, effectors that directly interact with and trigger a cell death response when co-expressed with their cognate MLAs MLA1, MLA6, MLA7, MLA9, MLA10, MLA13 and MLA22, respectively[26-28]. Of these AVR_As, the crystal structures of AVR_{A6}, AVR_{A7}, AVR_{A10}, and AVR_{A22} revealed RNase-like folds that are lacking some of the key residues in the conserved catalytic binding pocket[29]. Moreover, evidence suggests that AVR_{A6}, AVR_{A10}, and AVR_{A22} are all recognised by their basal loops at the LRR of their respective, cognate MLA[28,29]. Similar to Sr-AvrSr pairs, structural information of MLA-AVR_A interactions remains unresolved, limiting our understanding of how sequence similar CNLs specifically recognise structurally similar AVR_As.

The utility of *Mla*s reaches beyond immunity to *Bg* as some alleles have been found to recognise and trigger HR in response to infection by an evolutionarily diverse range of pathogenic microbes. For example, *Mla8* was found to confer dual resistance specificity to both barley powdery mildew (*Bg*) and wheat stripe rust (*Puccinia striiformis* f sp *tritici*; *Pst*) in barley[30]. Similarly, *Mla3* confers dual resistance specificity to barley powdery mildew and rice blast cause by *Magnaporthe oryzae*. Although the matching *Bg* AVR_{A3} remains uncharacterised, Pwl2 was identified as the *M. oryzae* avirulence effector responsible for triggering MLA3-mediated cell death[31,32]. Interestingly, the crystal structure of Pwl2 in complex with its virulence

target in rice (HIPP43) exhibits a MAX effector fold unlike the RNase-like folds of AVR_{A6}, AVR_{A7}, AVR_{A10}, AVR_{A22}[29,32]. Although multi resistance specificity is an alluring trait of MLAs, some pathogens can seemingly manipulate MLA-mediated resistance for their own benefit. For example, the *Mla* homologue *Susceptibility to Cochliobolus sativus 6* (*Scs6*) is believed to be 'highjacked' by the necrotrophic fungus *Bipolaris sorokiniana* isolate ND90Pr to promote cell death and proliferation of the pathogen[33]. The delivery of an uncharacterised yet presumed non-ribosomal peptide effector into the host cell results in an LRR-dependent interaction with SCS6 and cell death response[33]. The diverse range of MLA-engaging microbes highlights how these CNLs are potent for conferring multi resistance specificity yet need to be regulated by the host to avoid manipulation by necrotrophic pathogens.

Advances in AVR characterisation and structural resolution of NLR-effector interactions has spurred interest in the rationale design of NLRs for gain-of-function recognition of non-cognate effectors. One commonly reported approach to engineering resistance is the swapping or modification of the heavy metal associated (HMA) ID of rice NLRs Pik and Pia which has shown promising results of expanded effector recognition specificity for enhanced disease resistance to *M. oryzae*[34-40]. Alternatively, swapping LRR domains between NLRs or structure-guided engineering of the LRR has proven to be a promising approach to altering effector recognition specificity. In the case of MLA3, transferring the Pwl2-interacting segment of the LRR to the LRR of Sr50 resulted in a dual function Sr50 receptor capable of activation by both AvrSr50 and Pwl2[41]. A more targeted approach was successful in transferring AvrSr50 recognition specificity to Sr33 with the substitution of 12 amino acids from the LRR of Sr50[42]. Notably, some of the tested substitutions in the LRR of Sr50 resulted in receptor autoactivity. Modelling of the inactive receptor suggests that some of these putatively effector-interacting residues in the LRR interact with the NB-ARC 'latch' region to maintain an inactive conformation in the absence of AvrSr50[42]. Although the above-mentioned approaches show promising advances, high resolution structural information of the interface between the LRR and AVRs is lacking, limiting the potential for targeted engineering for broad effector recognition by NLRs.

In the first chapter of this thesis, we co-expressed wheat Sr35 and *Pgt* effector AvrSr35 in insect cell cultures to analyse the resulting conformation Sr35-AvrSr35 heterocomplexes. Cryo-EM and subsequent modelling revealed a pentameric resistosome of ~24 nm at 3.2 Å. We performed cell death assays in wheat protoplasts and *N. benthamiana* with structure-guided substitution mutants of both Sr35 and AvrSr35 to validate the cryo-EM structure and to further verify which residues at the effector-LRR interfaces are indispensable for recognition and receptor activation. We then introduced a minimal number of substitutions into two Sr35 homologues with unknown function to test if these receptors could gain recognition of AvrSr35. These data revealed the first cryo-EM structure of a crop CNL directly interacting with its cognate effector and revealed common principles of calcium channel formation of CNL resistosomes.

In the second chapter, we expressed barley MLA13 and *Bg* AVR_{A13}-1 in leaves of *N. benthamiana* to purify and resolve the resulting heterocomplex *via* cryo-EM. The resulting structure revealed a stable MLA13-AVR_{A13}-1 heterodimer, contrary to the pentameric conformation of the aforementioned Sr35 resistosome. The heterodimer measured ~11 nm in length and was resolved to 3.8 Å. Structure guided mutagenesis and cell death assays validated the interacting residues between AVR_{A13}-1 and the MLA13 LRR that are necessary for triggering a cell death

response. Structural analysis and sequence alignment prompted us to generate a synthetic MLA7 receptor capable of triggering a cell death response in the presence of the non-cognate effectors AVR_{A13}-1 and the virulent variant AVR_{A13}-V2 while retaining recognition of its cognate AVR_{A7} variants.

In the third chapter, we present a robust and versatile protocol for expressing and purifying recombinant proteins from leaves of *N. benthamiana*. Firstly, we tested the expression levels of several diverse proteins that were codon altered for expression in insect cell cultures or *N. benthamiana* leaf expression systems. Additionally, we show that expressing the signal peptide of the effectors AVR_{A22} from *B. graminis* and Pwl2 from *M. oryzae* increases protein yield. We then generated and utilised Gateway compatible vectors with a backbone-encoded Twin-Strep tag for performing single-step affinity chromatography purification of heterocomplexes. The single-step co-expression and purification of Sr35 and AvrSr35 not only resulted in the isolation and resolution of the resistosome but also the AvrSr35 homodimer[43,44]. This shows that different expression and purification systems can lead to the same oligomeric state of some proteins. The protocol exhibits versatility for a diverse range of protein complexes and clarifies time-consuming optimisation parameters when tailoring for a user-specific application.

Chapter 1: A wheat resistosome defines common principles of immune receptor channels

A wheat resistosome defines common principles of immune receptor channels

https://doi.org/10.1038/s41586-022-05231-w

Received: 22 March 2022

Accepted: 11 August 2022

Published online: 26 September 2022

Open access

Check for updates

Alexander Förderer[1,2,7], Ertong Li[1,2,7], Aaron W. Lawson[2,7], Ya-nan Deng[3,4,7], Yue Sun[5], Elke Logemann[2], Xiaoxiao Zhang[5], Jie Wen[5], Zhifu Han[5], Junbiao Chang[6], Yuhang Chen[3,4]✉, Paul Schulze-Lefert[2]✉ & Jijie Chai[1,2,5]✉

Plant intracellular nucleotide-binding leucine-rich repeat receptors (NLRs) detect pathogen effectors to trigger immune responses[1]. Indirect recognition of a pathogen effector by the dicotyledonous *Arabidopsis thaliana* coiled-coil domain containing NLR (CNL) ZAR1 induces the formation of a large hetero-oligomeric protein complex, termed the ZAR1 resistosome, which functions as a calcium channel required for ZAR1-mediated immunity[2–4]. Whether the resistosome and channel activities are conserved among plant CNLs remains unknown. Here we report the cryo-electron microscopy structure of the wheat CNL Sr35[5] in complex with the effector AvrSr35[6] of the wheat stem rust pathogen. Direct effector binding to the leucine-rich repeats of Sr35 results in the formation of a pentameric Sr35–AvrSr35 complex, which we term the Sr35 resistosome. Wheat Sr35 and *Arabidopsis* ZAR1 resistosomes bear striking structural similarities, including an arginine cluster in the leucine-rich repeats domain not previously recognized as conserved, which co-occurs and forms intramolecular interactions with the 'EDVID' motif in the coiled-coil domain. Electrophysiological measurements show that the Sr35 resistosome exhibits non-selective cation channel activity. These structural insights allowed us to generate new variants of closely related wheat and barley orphan NLRs that recognize AvrSr35. Our data support the evolutionary conservation of CNL resistosomes in plants and demonstrate proof of principle for structure-based engineering of NLRs for crop improvement.

Plant nucleotide-binding leucine-rich repeat receptors (NLRs) are intracellular receptors that play a key role in the plant innate immune system by sensing the presence of pathogen effectors delivered inside plant cells during pathogenesis through direct or indirect recognition[1,7]. Activation of plant NLRs generally leads to an array of immune responses, often linked to rapid host cell death at sites of attempted pathogen infection. Structural and functional homologues of plant NLRs evolved from independent events for intracellular non-self-perception in animal innate immunity and are characterized by their conserved central nucleotide-binding and oligomerization domains (NODs)[8]. Plant NLRs can be broadly separated into two classes: CNL with an N-terminal coiled-coil domain and TNL with an N-terminal Toll/interleukin 1 receptor (TIR) domain. Among the flowering plants dicots typically possess both receptor classes, whereas monocots, including cereals, encode only CNL receptors[9].

Wheat stem rust caused by fungal infection with *Puccinia graminis* f. sp. *tritici* (*Pgt*) threatens global wheat production[10], and the emergence of widely virulent *Pgt* strains, including the Ug99 lineage, has motivated the search for stem rust resistance in wheat germplasm and wild relatives over the past two decades. This resulted in the isolation of 11 phylogenetically related stem rust resistance (*Sr*) genes that belong to a clade of grass CNLs, all of which confer strain-specific immunity[5,11–18] ('clade I' CNLs defined in ref. [18]). The mildew resistance locus A (MLA) receptors of the wheat sister species barley also belong to this group of grass CNLs and share strain-specific immunity with *Sr* genes[18]. *Sr35* was first identified in a landrace of the *Triticum urartu* relative *Triticum monococcum* (einkorn) and confers immunity to *Pgt* Ug99 in bread wheat when transferred as a transgene[5]. However, because *Sr35* was absent in the diploid A genome of the wild ancestor of wheat, *T. urartu*, it was initially absent in hexaploid bread wheat (*Triticum aestivum*). *Sr35* resistance has been linked to the recognition of the *Pgt* effector *AvrSr35*[6], but until now, it has remained inconclusive whether Sr35 receptor-mediated host cell death is driven by direct physical interaction with the AvrSr35 effector[6,19].

Cryo-electron microscopy of the Sr35 resistosome

To purify Sr35, we expressed the protein alone or together with AvrSr35 in Sf21 insect cells. Unexpectedly, cell death was observed when the receptor was co-expressed with *AvrSr35* (Extended Data Fig. 1a),

[1]Institute of Biochemistry, University of Cologne, Cologne, Germany. [2]Max Planck Institute for Plant Breeding Research, Cologne, Germany. [3]State Key Laboratory of Molecular Developmental Biology, Institute of Genetics and Developmental Biology, Chinese Academy of Sciences, Beijing, China; Innovative Academy of Seed Design, Chinese Academy of Sciences, Beijing, China. [4]College of Advanced Agricultural Sciences, University of Chinese Academy of Sciences, Beijing, China. [5]Beijing Advanced Innovation Center for Structural Biology, Tsinghua-Peking Joint Center for Life Sciences, Center for Plant Biology, School of Life Sciences, Tsinghua University, Beijing, China. [6]Henan Key Laboratory of Organic Functional Molecules and Drug Innovation, Henan Normal University, School of Pharmaceutical Sciences, Zhengzhou University, Zhengzhou, China. [7]These authors contributed equally: Alexander Förderer, Ertong Li, Aaron W. Lawson, Ya-nan Deng. ✉e-mail: yuhang.chen@genetics.ac.cn; schlef@mpipz.mpg.de; chai@mpipz.mpg.de

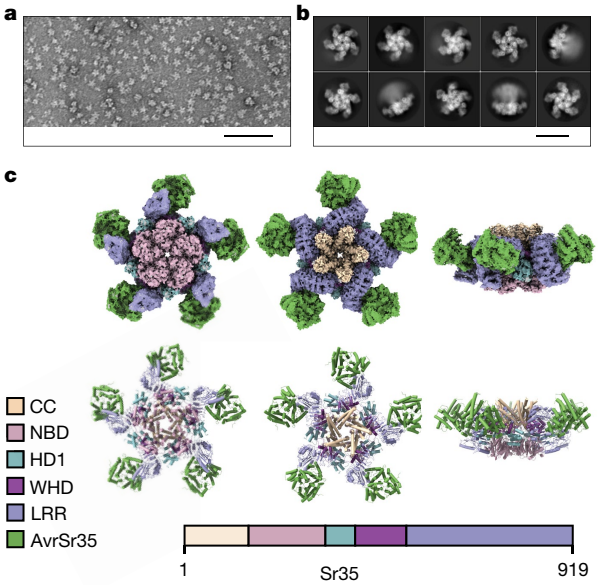

Fig. 1 | 3D reconstruction of the Sr35 resistosome. a, Negative staining of purified Sr35 in complex with AvrSr35 (Sr35 resistosome). Star-shaped particles were enriched by affinity purification and size-exclusion chromatography. Monodisperse Sr35 resistosomes have an average size of approximately 24 nm. Scale bar, 100 nm. **b**, 2D classifications of the Sr35 resistosome particles from the cryo-EM sample. Particles show preferential orientations for bottom and top views. Fewer, but sufficient, particles are in side view. Scale bar, 20 nm. **c**, Cryo-EM density map with 3 Å resolution (top) and the finally refined structure model (bottom) of the Sr35 resistosome shown in three different orientations. AvrSr35 is coloured green and Sr35 domains are shown according to the colour codes in the inset panel.

suggesting that Sr35 and its effector are sufficient to mediate this immunity-associated response in insect cells in the absence of other plant proteins. To circumvent cell death activation for protein purification, we introduced substitutions in the N-terminal residues L15E/L19E ($Sr35^{L15E/L19E}$), which are predicted to be essential for Sr35 membrane association by analogy with the ZAR1 resistosome[3]. Mutational analysis of the corresponding N-terminal residues of the tomato CNL NRC4 has been shown to abrogate cell death activity in *Nicotiana benthamiana*[20]. Indeed, the $Sr35^{L15E/L19E}$ substitutions markedly reduced *Sr35*-induced cell death in insect cells (Extended Data Fig. 1a and Supplementary Table 1). Using affinity-tagged $Sr35^{L15E/L19E}$ co-expressed with affinity-tagged AvrSr35, we were able to enrich the Sr35–AvrSr35 complex for subsequent separation of potential receptor complex isoforms and correctly folded receptor complexes by size-exclusion chromatography (Extended Data Fig. 1b,c). The affinity-purified protein complex was eluted with a broad peak with a maximum UV absorbance at 65 ml elution volume exceeding 669 kDa (66 ml) of our largest protein marker. Individual fractions were analysed via negative staining and a large number of star-shaped particles with fivefold symmetry were identified (fractions at 60–69 ml; Fig. 1a). The most monodisperse fractions were pooled and used for cryo-electron microscopy (cryo-EM) analysis.

We analysed the Sr35–AvrSr35 complex sample by cryo-EM (Extended Data Fig. 1) using a total of 1,608,441 individual particles for reference-free two-dimensional (2D) classification (Fig. 1b). After three-dimensional (3D) classification, a subset of 230,485 particles was used for reconstruction, yielding a density map of 3.0 Å (Fig. 1c, top). Despite the high resolution of up to 2.5 Å in the centre of the complex, the local resolution decreased towards the outer edge to approximately 4 Å (Extended Data Fig. 1f), indicating that the outer region of the complex is more flexible. To compensate for this decreased resolution, a local mask was used for the outer region, yielding a local density map with a resolution of 3.33 Å (Extended Data Fig. 1f). Both density maps were used for model building (Fig. 1c, bottom).

The final 3D reconstruction of the Sr35–AvrSr35 complex contains five receptor protomers, each bound to one effector molecule. The reconstruction revealed a star-shaped structure, similar to the ZAR1 resistosome[3], that we termed the Sr35 resistosome. As in the ZAR1 resistosome, five Sr35 NOD modules define the base of the circular protomer arrangement, and a helical barrel formed by the fivecoiled-coil domains is buried at the centre. Unlike ZAR1, the leucine-rich repeat (LRR) domains at the outer region do not pack against each other in the Sr35 resistosome, which might explain why this region is more flexible. AvrSr35 adopts an exclusively helical fold (Extended Data Fig. 2). A 3D structure homology search using the server DALI[21] showed that there are no other known protein structures sharing the AvrSr35 fold. Five AvrSr35 proteins bind exclusively to the C-terminal part of the LRR domains in the complex.

Oligomerization of the Sr35 resistosome

The central NOD module of plant NLRs is subdivided into a nucleotide-binding domain (NBD), helical domain 1 (HD1) and winged helical domain (WHD). ATP/dATP has been shown to be important for ZAR1 oligomerization as it stabilizes the active conformation of ZAR1 via its interaction with the WHD in the NOD module. There is an unambiguous cryo-EM density at the predicted nucleotide-binding site between the HD1 and NBD domains that is unfilled by Sr35 and AvrSr35. An ATP molecule fits well into this cryo-EM density. The modelled ATP is nested in a groove formed by HD1 and NBD. The short α-helix that mediates interprotomer interaction (Fig. 2a,c) also caps the ATP molecule. In contrast to that of ZAR1, the ATP in Sr35 does not directly contact the WHD. Instead, the γ-phosphate group of the ATP forms a bidentate hydrogen bond with Sr35 NBD^{R157} and NBD^{R311} (Fig. 2c). The latter also forms a hydrogen bond with Sr35 WHD^{S420} (Fig. 2c), showing an indirect coupling of the ATP γ-phosphate group with the WHD of Sr35.

Similar to the ZAR1 resistosome, NBD–NBD contacts contribute to Sr35 protomer packing (Fig. 2a,d). Sr35 NBD^{Y244} from one protomer packs tightly against Sr35 NBD^{R259} and Sr35 NBD^{Y263} from an adjacent protomer (Fig. 2d). Additionally, a hydrogen bond is established between Sr35 NBD^{Y244} and Sr35 NBD^{R259}. Of note, the coiled-coil domain of Sr35 contributes considerably to the interprotomer interactions (Fig. 2a): the C-terminal half of α4-helix from one protomer packs against the C-terminal sides of α2- and α4-helices of the neighbouring coiled-coil protomer. At the centre of this interface in the coiled-coil is Tyr141 (CC^{Y141}), which makes extensive hydrophobic contacts with Sr35 CC^{L42}, CC^{M43}, CC^{L47} and CC^{W65} (Fig. 2e). Moreover, CC^{Y141} participates in a hydrogen bonding triad together with CC^{R140} from the same and CC^{E39} from the neighbouring protomer (Fig. 2e). As previously reported[22], the long linker region between the coiled-coil and NBD domain is also involved in mediating oligomerization of the Sr35 resistosome.

To functionally test the requirements for these interactions in mediating the assembly of the Sr35 hetero-oligomeric complex, we introduced amino acid substitutions into the receptor and assessed their impact on Sr35-mediated cell death using a luciferase (LUC) activity assay in wheat protoplasts[23] prepared from a genotype that does not recognize AvrSr35 (cultivar 'Chinese Spring'). In this protoplast transfection assay, the relative (to empty vector, EV) luminescence of the LUC reporter is an indicator of cell viability. Cotransfection of *Sr35*, *AvrSr35* and the *LUC* reporter resulted in a near complete loss of luminescence signal, indicating massive cell death of the protoplasts and suggesting receptor activation by AvrSr35 (Fig. 2g). Consistent with the insect cell data described above, wheat protoplasts co-expressing $Sr35^{L15E/L19E}$ and *AvrSr35* displayed luminescence levels that were comparable to those co-expressing *EV* and *AvrSr35* constructs, indicating

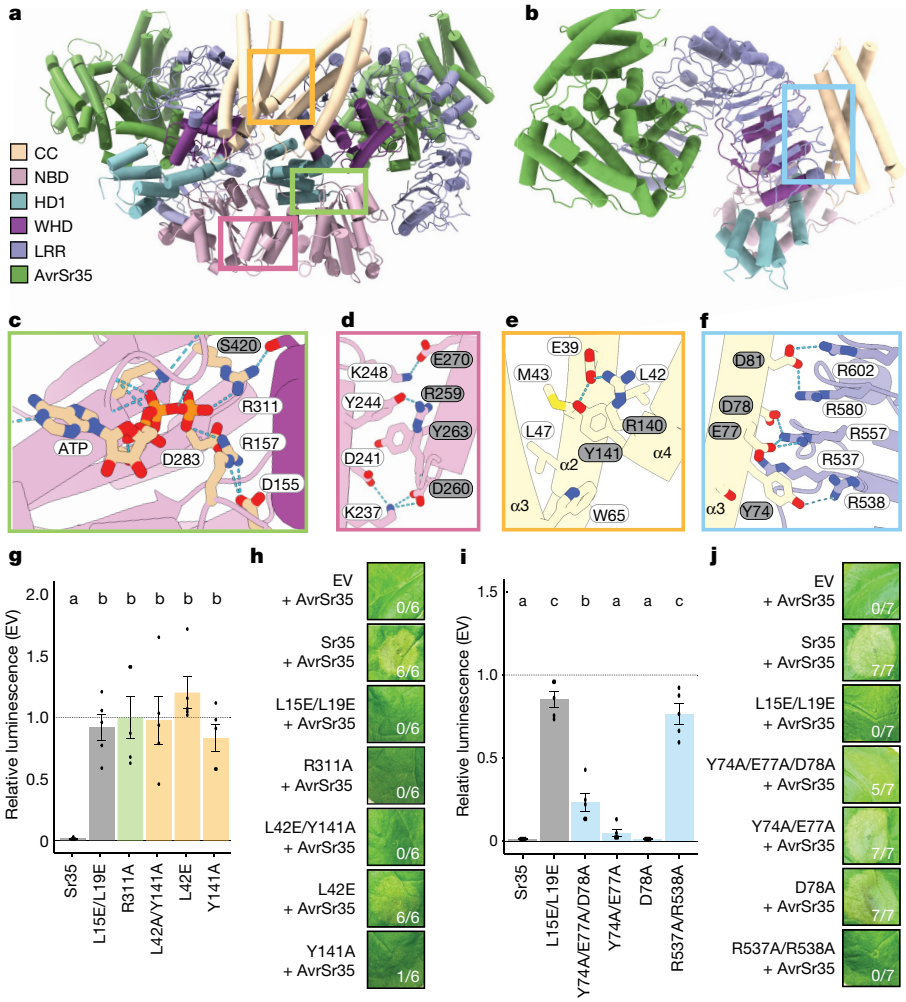

Fig. 2 | Assembly of the Sr35 resistosome. a, Sr35 resistosome showing a lateral dimer. Boxes in green, yellow and pink indicate positions of the zoomed views in **c**–**f**. Sr35 domains and AvrSr35 coloured according to the inset panel. **b**, Structure of one Sr35 protomer in complex with AvrSr35. Colour codes as in **a**. The blue box indicates position of structural detail in **f**. **c**, Structural detail of ATP binding in one protomer. Note the specific hydrogen bond of R311 with the γ-phosphate group of ATP at a 2.8 Å distance. Grey and white residue labels correspond to NBD and WHD residues, respectively. **d**, Structural detail of the interface between NBDs of a lateral dimer. Dashed lines represent polar interactions. Grey and white residue labels correspond to two neighbouring protomers from the pentamer. **e**, Structural detail of interface between two coiled-coil (CC) protomers. **f**, Structural detail of coiled-coil and LRR domain intramolecular packing in one Sr35 protomer. Acidic residues in the CC^{EDIVD} form salt-bridges with basic Arg (R) residues of the $LRR^{R\text{-}cluster}$. **g**, Cotransfection of *Sr35* and *Sr35* mutants with *AvrSr35* in wheat protoplasts. Relative luminescence as readout for cell death. EV treatment defined the relative baseline (mean ± s.e.m.; $n = 5$). Test statistics derived from analysis of variance (ANOVA) and Tukey post hoc tests ($P < 0.05$). Exact P values for all protoplast plots are provided in Supplementary Table 3. Bar colours as box colours in **c** and **d**. **h**, Tobacco cell death data of *Sr35* and *Sr35* mutants with *AvrSr35*. **i**, Wheat protoplast data of EDIVD and R-cluster mutants. Experiment and statistics as in **g**. Bar colours as box colour in **f**. **j**, *Nicotiana benthamiana* cell death data of EDVID and R-cluster mutants. Representative data in **h** and **j** shown from seven replicates and scored for leaf cell death.

that the cell death activity of the $Sr35^{L15E/L19E}$ receptor is substantially impaired (Fig. 2g). A similarly drastic loss of receptor-mediated cell death activity was observed with substitutions predicted to affect coiled-coil interprotomer interactions (Y141A, L42E and L42E/Y141A) or the ATP-binding site (R311A) (Fig. 2g) (raw data of all protoplast measurements are provided in Supplementary Table 2).

To corroborate the data from wheat protoplasts, we used *Agrobacterium tumefaciens*-mediated transient gene expression of *Sr35* and *AvrSr35* in *N. benthamiana* leaves. Co-expression of *Sr35* and *AvrSr35*, but not *AvrSr35* plus EV, resulted in cell death in the *Agrobacterium*-infiltrated area (Fig. 2h). By contrast, cell death was abolished when *AvrSr35* was co-expressed with the *Sr35* mutants predicted to perturb Sr35 oligomerization (Fig. 2h), with the exception of $Sr35^{L42E}$, which showed residual cell death activity only in *N. benthamiana* (full versions of all tobacco agroinfiltrations are provided in Supplementary Figs. 1–8). In planta, protein levels of wild-type Sr35 and all receptor mutants tested were comparable, indicating that these substitutions do not render the receptor unstable (Extended Data Fig. 3a, and full versions of all blots are provided in Supplementary Figs. 9–11). Together, these data strongly suggest that the residues mediating Sr35 oligomerization in the cryo-EM structure are necessary for cell death activity in wheat and heterologous *N. benthamiana*.

A conserved sequence in the coiled-coil domain, long known as the 'EDVID (Glu-Asp-Val-Ile-Asp) motif' that is present in approximately 38% of *Arabidopsis* CNLs[24] and first described in the potato CNL Rx, is used to group CNLs with or without this motif[24,25]. In the cryo-EM structure of the Sr35 resistosome, the EDIVD motif (Glu-Asp-Ile-Val-Asp) and the adjacent Sr35 Y^{74} mediate the packing of the LRR domain against the coiled-coil domain. Acidic residues from the motif form strong contacts with five arginine residues in the LRR domain (LRR^{R537}, LRR^{R538}, LRR^{R557}, LRR^{R580} and LRR^{R602}). These contacts comprise two bidentate salt bonds and a cation–π interaction (Fig. 2b,f). The extensive contacts

in this region are further reinforced by hydrogen bonding and van der Waals contacts. These arginine residues are each separated by one iteration of the LRR motif, resulting in their spatial separation along the Sr35 amino acid sequence (Extended Data Fig. 4a). As previously noted[26], the cryo-EM structure of the ZAR1 resistosome shows that similar intramolecular interactions exist between arginine residues in the ZAR1 LRR and 'EDVID'. In both resistosomes the respective arginine residues cluster together and form a positively charged surface patch (Extended Data Fig. 4b). We therefore term this resistosome region $LRR^{R\text{-}cluster}$. Location of the arginine residues in different repeats of the LRR domain explains why the conservation of the $LRR^{R\text{-}cluster}$ had remained unnoticed. A sequence alignment of CNLs shows that the $LRR^{R\text{-}cluster}$ is conserved and co-occurs with the EDVID motif (Extended Data Fig. 4a).

To test whether the $LRR^{R\text{-}cluster}$ is necessary for *Sr35*-mediated cell death, we substituted residues from the interface between the arginine cluster and the EDIVD motif and assessed the impact of these mutations on cell death activity using the wheat protoplast and *N. benthamiana* leaf assays described above. Simultaneous mutations of $LRR^{R537A/R538A}$ in the $LRR^{R\text{-}cluster}$ essentially abolished cell death activity (Fig. 2i,j). Similarly, a triple substitution in the Sr35 EDIVD motif, including the adjacent Sr35 Y^{74}, (Y74A/E77A/D78A) reduced or abolished Sr35 cell death activity in protoplasts and *N. benthamiana*, without affecting NLR stability (Extended Data Fig. 3b). These observations suggest that the co-occurrence of the EDVID motif and $LRR^{R\text{-}cluster}$ is an evolutionarily conserved stabilization mechanism of CNL resistosomes. As the EDVID–$LRR^{R\text{-}cluster}$ interactions are also present in the inactive ZAR1 and AlphaFold2-modelled Sr35 monomers and an extensive fold switching occurs in the coiled-coil domain during receptor activation (Extended Data Fig. 4c), these intramolecular interactions may be transiently disrupted to allow α1-helix to flip.

Channel activity of the Sr35 resistosome

Albeit having only 28.4% sequence conservation and although the α1-helix region of Sr35, whose equivalent in ZAR1 resistosome forms a funnel-shaped structure, is not well defined, the structures of the wheat Sr35 and *Arabidopsis* ZAR1 resistosomes are highly similar (Extended Data Fig. 5). We thus reasoned that the two complexes might share channel activity. To test this conjecture we used an assay previously established in *Xenopus laevis* (*Xenopus*) oocytes[4] to assess potential channel activity of the Sr35 resistosome. Co-expression of *Sr35* and *AvrSr35*, but not either alone, generated currents as recorded by two-electrode voltage-clamp (Fig. 3a,b), suggesting that assembly of the Sr35 resistosome is required for the currents. In strong support of this conclusion, two *Sr35* mutants that impaired the interaction with AvrSr35 and abolished AvrSr35-dependent cell death activity of the receptor in planta ($Sr35^{R730D/R755Q}$ and $Sr35^{W803L/K754G}$; see below), lost their ability to produce currents in oocytes (Fig. 3c). In agreement with the data on cell death *in planta* and insect cells, co-expression of the α1-helix substitution mutant $Sr35^{L15E/L19E}$ with *AvrSr35* did not mediate currents in oocytes (Fig. 3c). Substitutions affecting the acidic inner lining of the funnel formed by α1-helices in $ZAR1^{E11A}$ have been shown to abolish cell death in planta and channel activities in oocytes[3,4]. Unexpectedly, both Sr35 resistosome channel and cell death activities were tolerant to these analogous acidic residue substitutions ($Sr35^{E17A/E22A}$) (Fig. 3c–e and Extended Data Fig. 3c) (raw data of all oocytes measurements are provided in Supplementary Table 4).

Xenopus oocytes express endogenous calcium-gated chloride channels (CaCC); thus, the currents detected in this assay could be confounded by the activity of these native channels. However, the addition of the CaCC inhibitor A01 only partially blocked the currents in *Xenopus* oocytes (Fig. 3b) and cotreatment with A01 and the calcium channel blocker $LaCl_3$ was required for complete inhibition of the electrical activity (Fig. 3b). Together, these results indicate that the Sr35 resistosome may contribute to mixed currents in *Xenopus* oocytes, possibly via Sr35 resistosome calcium channel activity.

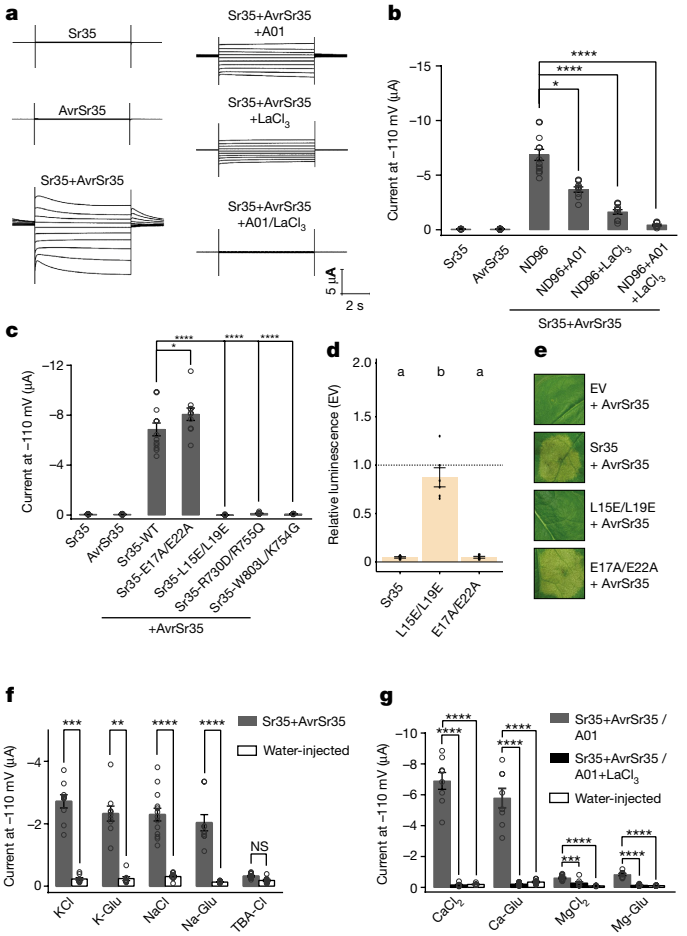

Fig. 3 | The Sr35 resistosome forms a Ca^{2+}-permeable non-selective cation channel. a, Representative measurements from two-electrode (TEVC) recordings from *Xenopus* oocytes expressing *Sr35*, *AvrSr35* and *Sr35/AvrSr35*. Effects of CaCCinh-A01 (Ca^{2+}-activated chloride channel inhibitor) and $LaCl_3$ (Ca^{2+} channel blocker) on the Sr35-mediated currents in ND96 solution (96 mM NaCl, 2.5 mM KCl, 1 mM $MgCl_2$, 1.8 mM $CaCl_2$, 5 mM HEPES, pH 7.6). Current traces shown at different voltages from −110 mV to +70 mV in 20 mV increments and current amplitudes at −110 mV. **b**, Quantitative measurements of data as in **a**. **c**, Structure-based mutagenesis of Sr35 residues at the interface between the LRR domain of Sr35 and AvrSr35, and Sr35 α1-helix. TEVC recordings in ND96 solution, and current amplitudes at −110 mV. **d**, Wheat protoplast data of Sr35 mutations at α1-helix. Relative luminescence as readout for cell death. EV treatment defined the relative baseline (mean ± s.e.m.; $n = 5$). Test statistics derived from ANOVA and Tukey post hoc tests ($P < 0.05$). Exact P values are provided in Supplementary Table 3. **e**, Tobacco cell death data of Sr35 and Sr35 channel mutants. Representative data shown from a minimum of three replicates. **f**, The Sr35 channel is selective for cations. TEVC recordings performed in various solutions, including KCl (96 mM), K-gluconate (96 mM), NaCl (96 mM), Na-gluconate (96 mM) and TBA-Cl (96 mM). **g**, Cationic currents of $CaCl_2$, Ca-Glu, $MgCl_2$ and Mg-Glu in the presence of CaCCinh-A01 and CaCCinh-A01+$LaCl_3$. Data are mean ± s.e.m., $n \geq 8$ (**b**,**c**,**f**,**g**). *$P \leq 0.05$, **$P \leq 0.01$, ***$P \leq 0.001$, ****$P \leq 0.0001$, one-way ANOVA analyses and Tukey post hoc test in **b**, **c** and **g**, and two-sided Student's *t*-tests in **f**.

To test whether the Sr35 resistosome can function as a non-selective cation channel, we tested cation flux in the presence of monovalent solutions of potassium and sodium chloride salts (KCl, NaCl). Similar to the ZAR1 resistosome, co-expression of *Sr35* and *AvrSr35* increased cation flux in oocytes, which was retained for potassium and sodium salts with the immobile gluconate counter-ion (K-Glu, Na-Glu). By contrast,

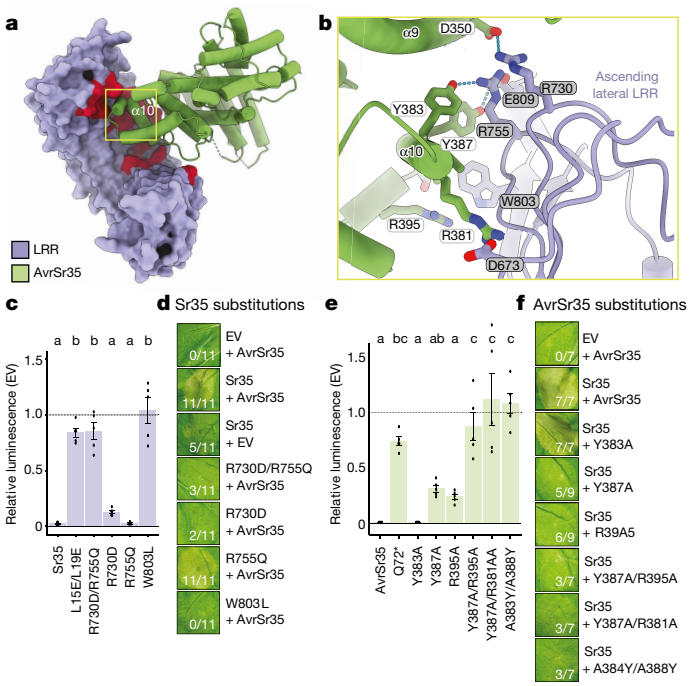

Fig. 4 | Direct AvrSr35 effector recognition is mediated by the Sr35 LRR domain. a, Interface between Sr35 LRR and AvrSr35. Red colour indicates the critical LRR residues within 5 Å from AvrSr35. **b**, Structural detail of Sr35 receptor and AvrSr35 effector interface. Dashed lines represent polar interactions. Grey and white residue label boxes correspond to Sr35 and AvrSr35 sidechains, respectively. **c**, Cotransfection of *Sr35* LRR mutants with *AvrS35* in wheat protoplasts. Relative luminescence as readout for cell death. EV treatment defined the relative baseline (mean ± s.e.m.; $n = 5$). Test statistics derived from ANOVA and Tukey post hoc tests ($P < 0.05$). Exact P values for all protoplast plots are provided in Supplementary Table 3. Bar colours correspond to box colours in **b**. **d**, *Nicotiana benthamiana* cell death data of *Sr35* LRR mutations at the receptor–effector interface. Representative data are shown from 11 replicates and scored for leaf cell death. **e**, Cotransfection of *Sr35* with *AvrS35* mutants in wheat protoplasts. Experimental layout and statistics as in **c** (mean ± s.e.m.; $n = 5$). Bar colours as domain colours in **a**. **f**, *Nicotiana benthamiana* cell death data of *AvrSr35* mutants co-expressed with *Sr35*. Representative data are shown from nine replicates and scored for leaf cell death.

we observed only residual ion flux when a chloride salt of the immobile tetrabutylammonium was used (TBA-Cl) (Fig. 3f). A comparison of the divalent ions Ca^{2+} and Mg^{2+} ($MgCl_2$, $CaCl_2$) combined with the *Sr35* and *AvrSr35* co-expression in oocytes, showed that ion flux was significant for calcium but not magnesium (Fig. 3g). This finding supports the conclusion that the Sr35 resistosome is permeable to calcium. Although our collective data strongly suggest that the Sr35 resistosome functions similarly to the ZAR1 resistosome by forming a non-selective calcium channel, the channel activity of the Sr35 resistosome is tolerant to substitutions of acidic residues predicted to line the inner surface of the channel. Thus, we cannot exclude the possibility that the very N terminus of the Sr35 resistosome (residues 1–21) is structurally and functionally distinct from that of the ZAR1 resistosome.

Direct recognition of AvrSr35 by Sr35

In the cryo-EM structure, AvrSr35 binds to the very C-terminal part of the Sr35 LRR domain, supporting a direct recognition mechanism of AvrSr35 by Sr35 (Fig. 4a). AvrSr35 is much larger than many other pathogen effectors, but only a small portion of the protein is in contact with the Sr35 LRR through charge and shape complementarity (Fig. 4a and Extended Data Fig. 6a,b). Nearly all residues that contribute to recognizing AvrSr35 are from the ascending lateral side of the last eight LRRs, and many of the residues interact with a single helix (α10) of AvrSr35. $AvrSr35^{Y383}$, $AvrSr35^{A384}$, $AvrSr35^{Y387}$ and $AvrSr35^{A388}$ from one α10 side are located at the centre of the Sr35–AvrSr35 interface and make extensive contacts with their respective neighbouring residues in Sr35 (Fig. 4b). Several residues in the loop region located C-terminal to α10 form hydrophobic contacts with $Sr35^{W919}$. Similar interactions are also made between $AvrSr35^{R381}$ in the N-terminal side of α10 and Sr35. In addition to the hydrophobic and van der Waals interactions, a large network of hydrogen bonds also mediates the Sr35–AvrSr35 interface, supporting specific recognition of AvrSr35 by Sr35 (individual contacts provided in Fig. 4b).

To functionally verify the Sr35–AvrSr35 interaction, we first substituted R730, R755 and W803 in Sr35 with their counterparts in the Sr35 homologue of wheat cultivar Chinese Spring[27] (here denoted *TaSh1*), which shares 86.5% sequence identity with Sr35 but is derived from a wheat cultivar susceptible to *Pgt* strains encoding *AvrSr35*[14]. These W803L or R730D substitutions strongly and weakly suppressed *Sr35*-mediated cell death activity, respectively, when co-expressed with *AvrSr35* in wheat protoplasts (Fig. 4c). By contrast, R755Q had no detectable effect on *Sr35*-induced cell death, but its combination with R730D resulted in a complete loss of cell death in wheat protoplasts (Fig. 4c). Similar results were obtained when these *Sr35* mutants were assayed in *N. benthamiana* (Fig. 4d and Extended Data Fig. 3d). These data support the Sr35–AvrSr35 interaction in the cryo-EM structure and explain why *TaSh1* in susceptible cultivar Chinese Spring is unable to recognize AvrSr35. To further verify specific AvrSr35 recognition by Sr35, we made the following substitutions in the fungal effector at their interface: Y383A, Y387A, R395A, Y387A/R395A, Y387A/R381A, A384Y/A388Y, all of which either form hydrogen bonds or salt-bridges with the Sr35 LRR (Fig. 4b). Similar to the Q72* premature stop codon mutant of AvrSr35 (Fig. 4e)[6], the mutations Y387A/R395A, Y387A/R381A and A384Y/A388Y abolished *Sr35*-induced cell death in wheat protoplasts and *N. benthamiana* (Fig. 4e,f and Extended Data Fig. 3e). By contrast, single mutations of Y387A and R395A only partially abolished effector-triggered receptor activation (Fig. 4e,f and Extended Data Fig. 3e), and several other single mutations of AvrSr35 (Extended Data Fig. 6b) had no effect, suggesting that much of the AvrSr35–Sr35 interface is resilient to disruption by single amino acid substitutions.

Sr35 receptor activation by steric clash

We made structural predictions of inactive, monomeric Sr35 using AlphaFold2 (ref. [28]). In these predictions, structures of all individual domains were highly similar to those in the Sr35 resistosome and the LRR domain in particular was accurately predicted (Extended Data Fig. 7a). Although some predictions were a close match with the domain organization of Sr35 in the resistosome, other individual predictions showed striking differences in the domain organization of NOD module (NBD–HD1 relative to WHD) (Extended Data Fig. 7b). These predictions shared the relative domain organization of inactive, monomeric ZAR1 and other inactive NLR structures[29], and most likely represent an inactive Sr35 structure. Modelling of AvrSr35 onto the LRR domain of the predicted structure of inactive Sr35 shows substantial overlap between the effector and Sr35 NBD (Extended Data Fig. 8). This is reminiscent of ZAR1 activation, which occurs through an allosteric mechanism involving a 'steric clash' with the NBD[2,3]. Comparison of Sr35 and ZAR1 resistosomes suggests that this 'steric clash' mechanism is likely to be conserved in CNLs. AvrSr35 binding dislodges the NBD, allowing subsequent nucleotide exchange for further ATP-triggered allosteric changes in the receptor and assembly of the Sr35 resistosome. Together, these results support a conserved allosteric mechanism underlying activation of the Sr35 and ZAR1 resistosomes. Ligand binding to the ascending lateral side of the LRR domain was also seen in the structures of the TNL RPP1 (ref. [30]) and Roq1 (ref. [31]) resistosomes (Extended Data Fig. 9), suggesting that the ligand binding mechanism may be conserved in plant NLRs[29].

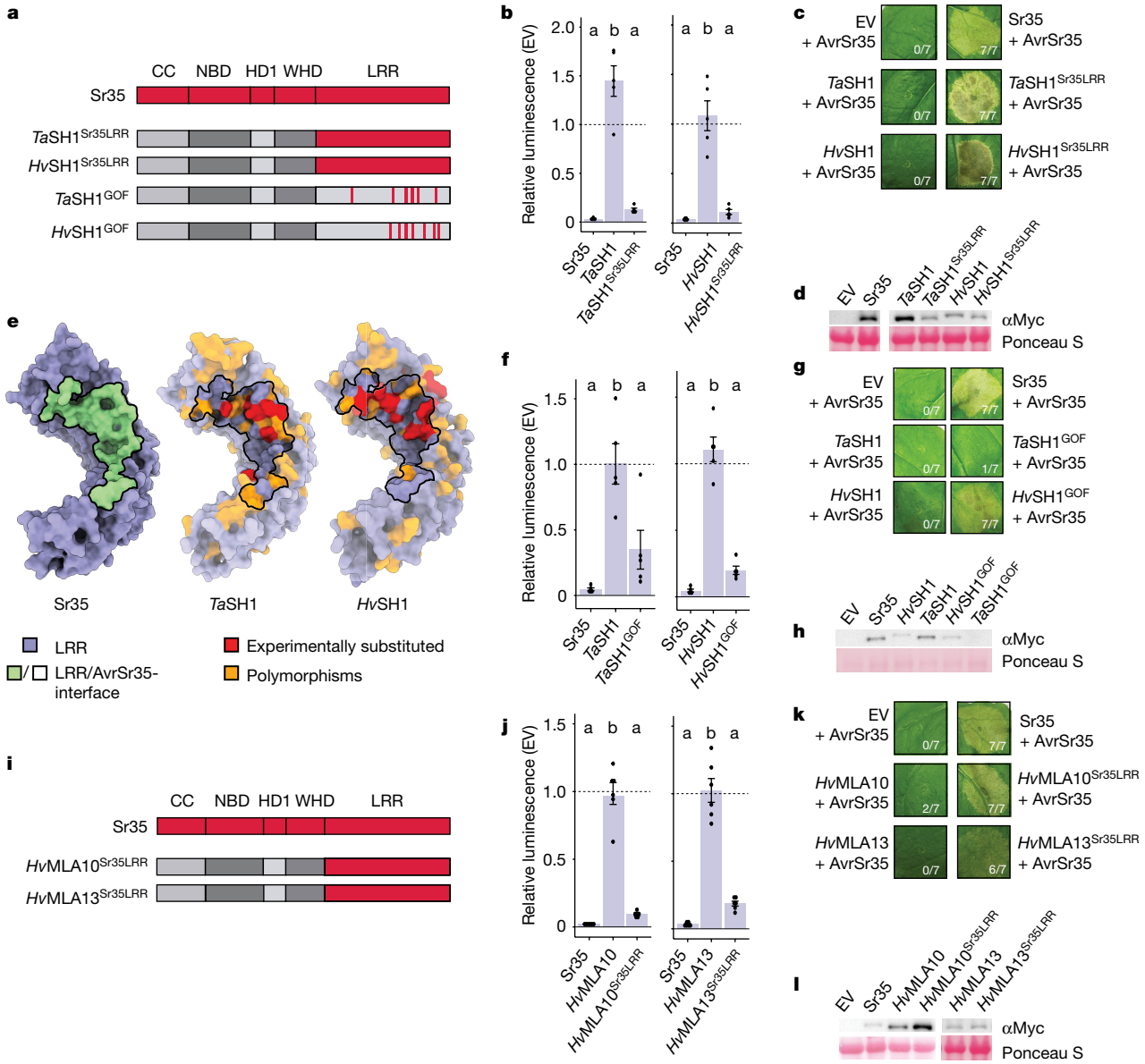

Fig. 5 | Structure-guided neofunctionalization of orphan CNLs and MLA receptor hybrids. a, Illustration of Sr35 domain structure and hybrid receptors made from Sr35 homologues (*Sh*) in bread wheat (*Triticum aestivum*; *TaSh1*) and barley (*Hordeum vulgare*; *HvSh1*). Sr35^{LRR} (red) substitutes *Ta*SH1^{LRR} and *Hv*SH1^{LRR} (*Ta*SH1^{Sr35LRR} and *Hv*SH1^{Sr35LRR}). GOF receptor variants (*TaSh1^{GOF}* and *HvSh1^{GOF}*) were derived from sequence polymorphisms between Sr35, *Ta*SH1 and *Hv*SH1. **b**, Wheat protoplast transfections of *TaSh1^{Sr35LRR}*, *HvSh1^{Sr35LRR}* and controls co-expressed with *AvrSr35*. EV treatment defined the relative baseline (mean ± s.e.m.; $n = 6$). Test statistics derived from ANOVA and Tukey post hoc tests ($P < 0.05$). Exact P values for all protoplast plots are provided in Supplementary Table 3. **c**, Tobacco cell death of *TaSh1^{Sr35LRR}* and *HvSh1^{Sr35LRR}*. Representative data shown from seven replicates and scored for cell death. **d**, Western blot of hybrid receptors tested in tobacco. Pooled three replicates. Ponceau S staining as loading control. Composite image of same blot. **e**, Cryo-EM structure of Sr35 and structural predictions of *Ta*SH1^{LRR} and *Hv*SH1^{LRR} (ref. [28]). Polymorphisms between *Ta*SH1 or *Hv*SH1, and Sr35 are shown (orange). Residues mutated are shown red. **f**, Wheat protoplast transfections of *TaSh1^{GOF}*, *HvSh1^{GOF}* and controls co-expressed with *AvrSr35*. Experiment and statistics as in **b**. **g**, Tobacco cell death of *TaSh1^{GOF}* and *HvSh1^{GOF}*. Replicates and scoring as in **c**. **h**, Western blot of GOF experiment in tobacco. Replicates and loading control as in **d**. **i**, Graphical illustration of MLA hybrid receptors; design as in **a** (*HvMla10^{Sr35LRR}* and *HvMla13^{Sr35LRR}*). **j**, Wheat protoplast transfections of *HvMla10^{Sr35LRR}*, *HvMla13^{Sr35LRR}* and controls co-expressed with *AvrSr35*. Experiment and statistics as in **b**. **k**, Tobacco cell death of *HvMla10^{Sr35LRR}* and *HvMla13^{Sr35LRR}*. Replicates and scoring as in **c**. **l**, Western blot of MLA hybrid receptors in tobacco. Replicates and loading control as in **d**. Composite image of two independent blots.

Engineering of CNLs for effector recognition specificity

To test whether the evolutionary conservation of CNL resistosomes can be harnessed for the design of new receptors with altered function, we first chose two closely related *Sr35* homologues (*Sh*) of unknown resistance function in bread wheat (*Triticumaestivum*; *TaSh1*) and in the sister species barley (*Hordeumvulgare*; *HvSh1*). We generated hybrid receptors of *TaSh1* and *HvSh1* in which the LRR domain, including the highly conserved WHD α4-helix, was substituted by the equivalent fragment of Sr35 (termed *TaSh1^{Sr35LRR}* and *HvSh^{Sr35LRR}*) (Fig. 5a and Extended Data Fig. 10a). Unlike wild-type *TaSh1* or *HvSh1* genes, both hybrid receptors mediated *AvrSr35*-dependent cell death in wheat leaf protoplasts prepared from cultivar Chinese Spring and when expressed in leaves of *N. benthamiana* (Fig. 5b–d), indicating neofunctionalization of the orphan receptors.

Owing to the high sequence similarity of *Ta*SH1 and *Hv*SH1 with *T. monococcum* Sr35 (86.5% and 86.4% amino acid sequence identity to Sr35, respectively), we reasoned that targeted amino acid substitutions in the LRR domains of the homologues might be sufficient to enable detection of AvrSr35. Combined structural model (Extended Data Fig. 10b,c) and protein sequence alignments indicated that the AvrSr35-interacting residues of Sr35 are polymorphic in *Ta*SH1 and *Hv*SH1 (Fig. 5e and Extended Data Fig. 10d). The alignments identified several residues in the LRR domains of *Ta*SH1 and *Hv*SH1 that are likely to hinder effector binding at the modelled interface. Accordingly, we generated *TaSh1* and *HvSh1* variants encoding receptors with eight and ten substitutions in the LRR, respectively (*Ta*SH1$^{D609G/Y728F/D731R/I754K/Q755R/L804W/Q810E/R857W}$ and *Hv*SH1$^{Y727F/Q801E/G754K/Q752P/Q755R/R809E/W835I/R856W/917D/P919W}$; designated for simplicity *Ta*SH1^{GOF} and *Hv*SH1^{GOF}, respectively, in which GOFdenotes gain-of-function) (Fig. 5a). Unlike wild-type *HvSh1*, *HvSh1*^{GOF} mediated a clear cell death response in wheat protoplasts and *N. benthamiana* when co-expressed with the effector *AvrSr35* (Fig. 5f–h). *TaSh1*^{GOF} induced a notable cell death phenotype in wheat protoplasts, but not in *N. benthamiana* (Fig. 5f–h), which is probably due to undetectable *Ta*SH1^{GOF} protein in the heterologous *N. benthamiana* expression system (Fig. 5h). These findings suggest that targeted amino acid substitutions that mimic the effector binding region of Sr35 are sufficient for neofunctionalization of these orphan receptors. The relatively small number of nucleotide changes needed to enable *Ta*SH1 to detect AvrSr35 makes it feasible to introduce such changes in elite bread wheat by gene editing. In this way, generating varieties that are resistant to *Pgt* Ug99[32–36] provides an alternative strategy to transgene-mediated *Sr35* transfer from *T. monococcum* to bread wheat[5,37].

Next, we investigated whether the Sr35 LRR domain, transferred to more distant CNLs (approximately 45% amino acid sequence identity) in the sister species barley, can generate functional hybrid receptors. We chose barley *Hv*MLA10 and *Hv*MLA13, known to confer isolate-specific immunity against the barley powdery mildew fungus[38], *Blumeria graminis* f. sp. *hordei* (*Bgh*), as templates to engineer AvrSr35 recognition (Fig. 5i). The ascomycete *Bgh* effectors recognized by *Hv*MLA10 and *Hv*MLA13 lack sequence similarity to AvrSr35 from the basidiomycete *Pgt*. Using the above reasoning for hybrid receptor generation of *Sr* homologues, the LRR domains of *Hv*MLA10 and *Hv*MLA13 were replaced by the Sr35 LRR. The two resulting hybrid receptors, *HvMla10*^{Sr35LRR} and *HvMla13*^{Sr35LRR}, induced cell death when co-expressed with *Pgt AvrSr35* in wheat protoplasts and *N. benthamiana* (Fig. 5j–l). This finding supports our hypothesis that a combination of effector binding to the LRR and steric clash of the effector with the NBD is needed for CNL activation, as exemplified here for hybrid receptors where the AvrSr35 effector is predicted to clash with the MLA NBD.

Discussion

Our results, together with earlier data, strongly suggest that the activation and signalling mechanisms of CNLs are evolutionarily conserved. Three independent lines of evidence support this idea: (1) our structural elucidation of the wheat Sr35 resistosome and its similarity to the previously reported *Arabidopsis* ZAR1 resistosome structure[3]; (2) the functional interspecies hybrid receptors generated from the non-orthologous CNLs wheat Sr35 and barley MLAs; and (3) the conservation extends to the non-selective cation flux across membranes enabled by pentamerization, although it is possible that ion selectivity and channel dynamics differ between individual CNLs, including the channel activity of so-called helper NLRs acting downstream of canonical plant NLRs[39]. Reconstitution of effector-dependent Sr35-triggered cell death in insect cells indicates that regulated channel activity is sufficient to recapitulate plant CNL-mediated cell death in eukaryotic cells of another kingdom. It is possible that plant CNL pore formation and ion flux trigger and intersect with intrinsic cell death pathways in animals, for example, Apaf-1 apoptosome-mediated developmental and stress-induced cell death[40,41]. Although the components needed for cell death downstream of CNL channel activity in plants remain to be identified, the evolutionary conservation of channel activity rationalizes how highly diverse pathogen signals activate a shared set of downstream responses. This is reminiscent of the highly conserved NADase activity encoded by the TIR domain, which converts the presence or activity of diverse pathogen molecules into TNL-triggered immune signals[30,31].

Our study also uncovers the mechanism by which direct or indirect recognition of pathogen effectors results in the formation of the conserved pentameric scaffold that facilitates channel activity. Indirect recognition of a bacterial pathogen effector by ZAR1 results in a conformational change of the NBD, allosterically promoting exchange of ADP with ATP/dATP for full receptor activation. Our data support a similar mechanism for Sr35 activation by direct recognition of AvrSr35. These results lend further support to the notion that the exchange of ADP with ATP/dATP is widely involved in the activation of NLRs. Although AvrSr35 is essential for the activation of Sr35, the effector makes no contribution to oligomerization of the Sr35 resistosome, which is principally mediated by the conserved NBD. This is also true for the assembly of the ZAR1 resistosome in *Arabidopsis* and the Apaf-1 apoptosome in animals[3,42]. It seems that recognition of diverse pathogen effectors by the polymorphic LRRs release the conserved NBD to mediate NLR oligomerization.

A third plant NLR recognition mechanism involves a combination of direct and indirect recognition through the incorporation of effector target domains (integrated decoys) into the NLR domain architecture, termed NLR-IDs, representing approximately 10% of all NLR-encoding genes of a plant species[43]. Crystal structures of the ID in complex with the bound pathogen effector have been resolved for two NLR-IDs, enabling structure-informed ID engineering to extend pathogen strain-specific NLR recognition[44–46]. How the corresponding full-length NLR-ID receptors are activated, including a potential steric clash with their NBD is unclear owing to a lack of full-length receptor structures. This is further complicated as NLR-IDs, which directly recognize effectors, typically function with canonical NLRs as interacting pairs[43]. Direct recognition of pathogen effectors by plant NLRs can be rapidly circumvented by polymorphisms of effector residues at the effector–NLR interface, particularly as a pathogen and its host plant typically evolve at different time scales. Virulent isolates of *Pgt* within and beyond the Ug99 lineage have escaped the recognition of at least one of the recently cloned *Sr* genes, including single amino acid changes in the effector[47]. For example, a *Pgt* isolate with combined virulence against *Sr35* and *Sr50* caused an epidemic in Sicily in 2017[48]. Our findings allow the prediction not only of AvrSr35 substitutions that might escape Sr35 recognition, but also substitutions in the Sr35 LRR that can physically 're-capture' such effector variants. More generally, the evolutionarily conserved plant CNL resistosome architecture with its conserved function highlights the future potential of structure-guided NLR engineering for crop improvement.

Note added in proof: After completion of this work, the Sr35 resistosome structure was confirmed in an independent study[49].

Online content

Any methods, additional references, Nature Research reporting summaries, source data, extended data, supplementary information, acknowledgements, peer review information; details of author contributions and competing interests; and statements of data and code availability are available at https://doi.org/10.1038/s41586-022-05231-w.

1. Jones, J. D. G. & Dangl, J. L. The plant immune system. *Nature* **444**, 323–329 (2006).
2. Wang, J. Z. et al. Ligand-triggered allosteric ADP release primes a plant NLR complex. *Science* **364**, eaav5868 (2019).
3. Wang, J. Z. et al. Reconstitution and structure of a plant NLR resistosome conferring immunity. *Science* **364**, eaav5870 (2019).

4. Bi, G. Z. et al. The ZAR1 resistosome is a calcium-permeable channel triggering plant immune signaling. *Cell* **184**, 3528–352 (2021).
5. Saintenac, C. et al. Identification of wheat gene *Sr35* that confers resistance to Ug99 stem rust race group. *Science* **341**, 783–786 (2013).
6. Salcedo, A. et al. Variation in the *AvrSr35* gene determines *Sr35* resistance against wheat stem rust race Ug99. *Science* **358**, 1604–1606 (2017).
7. Dodds, P. N. & Rathjen, J. P. Plant immunity: towards an integrated view of plant–pathogen interactions. *Nat. Rev. Genet.* **11**, 539–548 (2010).
8. Urbach, J. M. & Ausubel, F. M. The NBS-LRR architectures of plant R-proteins and metazoan NLRs evolved in independent events. *Proc. Natl Acad. Sci. USA* **114**, 1063–1068 (2017).
9. Johanndrees, O. et al. Differential *EDS1* requirement for cell death activities of plant TIR-domain proteins. Preprint at *bioRxiv* https://doi.org/10.1101/2021.11.29.470438 (2021).
10. Singh, R. P. et al. The emergence of Ug99 races of the stem rust fungus is a threat to world wheat production. *Annu. Rev. Phytopathol.* **49**, 465–481 (2011).
11. Zhang, W. et al. Identification and characterization of *Sr13*, a tetraploid wheat gene that confers resistance to the Ug99 stem rust race group. *Proc. Natl Acad. Sci. USA* **114**, E9483–E9492 (2017).
12. Periyannan, S. et al. The gene *Sr33*, an ortholog of barley *Mla* genes, encodes resistance to wheat stem rust race Ug99. *Science* **341**, 786–788 (2013).
13. Mago, R. et al. The wheat *Sr50* gene reveals rich diversity at a cereal disease resistance locus. *Nat. Plants* **1**, 15186 (2015).
14. Chen, S., Zhang, W., Bolus, S., Rouse, M. N. & Dubcovsky, J. Identification and characterization of wheat stem rust resistance gene *Sr21* effective against the Ug99 race group at high temperature. *PLoS Genet.* **14**, e1007287 (2018).
15. Steuernagel, B. et al. Rapid cloning of disease-resistance genes in plants using mutagenesis and sequence capture. *Nat. Biotechnol.* **34**, 652–655 (2016).
16. Arora, S. et al. Resistance gene cloning from a wild crop relative by sequence capture and association genetics. *Nat. Biotechnol.* **37**, 139–143 (2019).
17. Gaurav, K. et al. Population genomic analysis of Aegilops tauschii identifies targets for bread wheat improvement. *Nat. Biotechnol.* **40**, 422–431 (2022).
18. Zhang, J. et al. A recombined *Sr26* and *Sr61* disease resistance gene stack in wheat encodes unrelated NLR genes. *Nat. Commun.* **12**, 3378 (2021).
19. Bolus, S., Akhunov, E., Coaker, G. & Dubcovsky, J. Dissection of cell death induction by wheat stem rust resistance protein Sr35 and its matching effector AvrSr35. *Mol. Plant Microbe Interact.* **33**, 308–319 (2020).
20. Adachi, H. et al. An N-terminal motif in NLR immune receptors is functionally conserved across distantly related plant species. *eLife* **8**, e49956 (2019).
21. Holm, L. in *Structural Bioinformatics: Methods and Protocols* (ed. Zoltán Gáspári) 29–42 (Springer US, 2020).
22. Xiong, Y., Han, Z. & Chai, J. Resistosome and inflammasome: platforms mediating innate immunity. *Curr. Opin. Plant Biol.* **56**, 47–55 (2020).
23. Saur, I. M. L., Bauer, S., Lu, X. & Schulze-Lefert, P. A cell death assay in barley and wheat protoplasts for identification and validation of matching pathogen AVR effector and plant NLR immune receptors. *Plant Methods* **15**, 118 (2019).
24. Wróblewski, T. et al. Genome-wide functional analyses of plant coiled–coil NLR-type pathogen receptors reveal essential roles of their N-terminal domain in oligomerization, networking, and immunity. *PLoS Biol.* **16**, e2005821 (2018).
25. Rairdan, G. J. et al. The coiled-coil and nucleotide binding domains of the potato Rx disease resistance protein function in pathogen recognition and signaling. *Plant Cell* **20**, 739–751 (2008).
26. Burdett, H. et al. The plant 'resistosome': structural insights into immune signaling. *Cell Host Microbe* **26**, 193–201 (2019).
27. Jia, H. et al. A semi-dominant NLR allele causes whole-seedling necrosis in wheat. *Plant Physiol.* **186**, 483–496 (2021).
28. Jumper, J. et al. Highly accurate protein structure prediction with AlphaFold. *Nature* **596**, 583–589 (2021).
29. Förderer, A., Yu, D., Li, E. & Chai, J. Resistosomes at the interface of pathogens and plants. *Curr. Opin. Plant Biol.* **67**, 102212 (2022).
30. Ma, S. et al. Direct pathogen-induced assembly of an NLR immune receptor complex to form a holoenzyme. *Science* **370**, eabe3069 (2020).
31. Martin, R. et al. Structure of the activated ROQ1 resistosome directly recognizing the pathogen effector XopQ. *Science* **370**, eabd9993 (2020).
32. Ishida, Y., Tsunashima, M., Hiei, Y. & Komari, T. in *Agrobacterium Protocols: Volume 1* (ed. Kan Wang) 189–198 (Springer, 2015).
33. Lowe, K. et al. Morphogenic regulators Baby boom and Wuschel improve monocot transformation. *Plant Cell* **28**, 1998–2015 (2016).
34. Richardson, T., Thistleton, J., Higgins, T. J., Howitt, C. & Ayliffe, M. Efficient Agrobacterium transformation of elite wheat germplasm without selection. *Plant Cell Tiss. Org.* **119**, 647–659 (2014).
35. Sánchez-León, S. et al. Low-gluten, nontransgenic wheat engineered with CRISPR/Cas9. *Plant Biotechnol. J.* **16**, 902–910 (2018).
36. Jouanin, A. et al. CRISPR/Cas9 gene editing of gluten in wheat to reduce gluten content and exposure—reviewing methods to screen for coeliac safety. *Front. Nutr.* https://doi.org/10.3389/fnut.2020.00051 (2020).
37. Luo, M. et al. A five-transgene cassette confers broad-spectrum resistance to a fungal rust pathogen in wheat. *Nat. Biotechnol.* **39**, 561–566 (2021).
38. Lu, X. et al. Allelic barley MLA immune receptors recognize sequence-unrelated avirulence effectors of the powdery mildew pathogen. *Proc. Natl Acad. Sci. USA* **113**, E6486–E6495 (2016).
39. Jacob, P. et al. Plant 'helper' immune receptors are Ca^{2+}-permeable nonselective cation channels. *Science* **373**, 420–425 (2021).
40. Chai, J. & Shi, Y. Apoptosome and inflammasome: conserved machineries for caspase activation. *Natl Sci. Rev.* **1**, 101–118 (2014).
41. Cerella, C., Diederich, M. & Ghibelli, L. The dual role of calcium as messenger and stressor in cell damage, death, and survival. *Int. J. Cell Biol.* **2010**, 546163–546163 (2010).
42. Zhou, M. et al. Atomic structure of the apoptosome: mechanism of cytochrome c-and dATP-mediated activation of Apaf-1. *Genes Dev.* **29**, 2349–2361 (2015).
43. Cesari, S. Multiple strategies for pathogen perception by plant immune receptors. *New Phytol.* **219**, 17–24 (2018).
44. Cesari, S. et al. New recognition specificity in a plant immune receptor by molecular engineering of its integrated domain. *Nat. Commun.* **13**, 1524 (2022).
45. De la Concepcion, J. C. et al. Protein engineering expands the effector recognition profile of a rice NLR immune receptor. *eLife* **8**, e47713 (2019).
46. Liu, Y. et al. A designer rice NLR immune receptor confers resistance to the rice blast fungus carrying noncorresponding avirulence effectors. *Proc. Natl Acad. Sci. USA* **118**, e2110751118 (2021).
47. Ortiz, D. et al. The stem rust effector protein AvrSr50 escapes Sr50 recognition by a substitution in a single surface-exposed residue. *New Phytol.* **234**, 592–606 (2022).
48. Bhattacharya, S. Deadly new wheat disease threatens Europe's crops. *Nature* **542**, 145–146 (2017).
49. Zhao, Y.-B. et al. Pathogen effector AvrSr35 triggers Sr35 resistosome assembly via a direct recognition mechanism. *Sci. Adv.* **8**, eabq5108 (2022).

Methods

Protein expression, purification and negative staining

Codon optimized *Sr35*$^{L15E/L19E}$ and *AvrSr35* genes were cloned into the pFastBac1 vector (Invitrogen) with an N-terminal 6×His-SUMO tag and an N-terminal glutathione *S*-transferase (GST) tag, respectively. The constructs were transformed into EMBacY[50] competent cells for recombinant bacmid DNA generation. Recombinant baculovirus was generated by initial lipofection with Xtreme gene reagent (Roche) of Sf21 insect cells (Invitrogen). Baculovirus was generally amplified to the P_2 generation before protein expression. *Sr35*$^{L15E/L19E}$ and *AvrSr35* were co-expressed in Sf21 insect cells, 50 ml of each virus was used per 1 l of culture. After expression of protein at 28 °C for 48 h, the insect cells were ollected and resuspended with buffer containing 50 mM Tris pH 8.0, 150 mM NaCl, 0.05% Triton X-100 and 5% glycerol. The cell lysates generated by sonication were centrifuged at 13,000 r.p.m. for 1.5 h, and then the supernatant was collected. The protein complex was purified with glutathione Sepharose 4B (GS4B) resin. After binding to the glutathione agarose twice, the agarose was washed with three column volumes of resuspension buffer, and the tagged protein complex was treated with GST-tagged PreScission protease at 4 °C overnight to remove GST and 6xHis-SUMO tags simultaneously. The digested protein complex in the flow-through was concentrated and subjected to HiLoad superpose 6 column (GE) in buffer containing 50 mM Tris pH 8.0, 100 mM NaCl and 0.01% Triton X-100. Pooled peak fractions were used for cryo-EM sample preparation.

Cryo-EM sample preparation and data collection

The Sr35–AvrSr35 complex grids were prepared for cryo-EM analysis. Holy carbon grids (Quantifoil Au 1.2/1.3, 300 mesh) were glow-discharged for 30 s at medium level in HarrickPlasma after 2 min evacuation. The purified Sr35–AvrSr35 protein was concentrated to approximately 0.5 mg ml^{-1} and 3 µl of sample were applied to the grid. The grids were blotted for 2–3 s using a pair of filter papers (55 mm, Ted Pella Inc.) at 8 °C with 100% humidity and flash-frozen in liquid ethane using a FEI Vitrobot Marked IV. Stacks of Sr35–AvrSr35 cryo-EM samples were collected by a Titan Krios microscope operated at 300 kV, equipped with a K3 Summit direct electron detection camera (Gatan) using EPU 2 (Thermo Fisher Scientific, 2.8.1.10REL) at Zhengzhou University. Micrographs were recorded at 81,000× magnification corresponding to 1.1 Å per pixel. The defocus ranged from −1.5 µm to −2.0 µm. Each image stack contains 32 frames recorded every 0.11 s for an accumulated dose of approximately 50 e− per Å^2 and a total exposure time of 3.5 s. A second dataset from an independent protein purification was recorded at EMBL Heidelberg with the following parameters: Titan Krios microscope operated at 300 kV, equipped with a K3 Summit direct electron detection camera (Gatan), 50 e per Å^2, 40 frames per stack.

Image processing and 3D reconstruction

All micrographs of the Sr35–AvrSr35 complex were 2 × 2 binned, generating a pixel size of 1.1 Å. The MotionCor2 program was used to perform Motion correction[51]. Contrast transfer function (CTF) parameters were estimated by CTFFIND4[52]. On the basis of the CTF estimations, 5,292 micrographs were manually picked and were further processed in RELION3.1[53].

1,608,441 particles were picked using Laplacian-of-Gaussian auto picking and then subjected to several rounds of 2D classification[54,55]. Every round of 2D classification performed 25 iterations with regularisation parameter $T = 2$ and number of classes = 100 to remove bad particles. The particles with the best quality were used to generate the initial model using ab initio calculation from RELION3.1. Then 698,386 particles were imported into 3D classification with *C*1 symmetry. There were five Sr35 molecules in the complex, each of which was bound to one AvrSr35 molecule. *C*5 symmetry was used in the following 3D refinement. After CTF refinement and postprocessing, the resolution of the Sr35–AvrSr35 complex reconstruction was 3.0 Å. The resolution was estimated by the gold-standard Fourier shell correlation = 0.143 criterion[56]. Local resolution distribution was evaluated using RELION 3.1 (ref. [57]).

In the reconstruction above, the LRR and AvrSr35 portions were more flexible than the other parts of the Sr35–AvrSr35 complex. To improve the density of the more flexible portions, we used a procedure as previously described[58]. The final refined particles were expanded with *C*5 symmetry. A local mask was generated using USCF Chimera[59]. Expanded particles and local mask were subjected to 3D classification without alignment. Finally, 476,069 particles were used for 3D auto-refinement and CTF refinement. A final resolution of 3.33 Å was achieved after postprocessing. For the second dataset, one third of the micrographs were analysed the same way and resulted in the same overall structure at a resolution of 3.4 Å. The resulting model was not used further for model building.

Model building and refinement

The final density map was obtained by merging the global map and the local map which contained LRR and AvrSr35, using a 'combine_focused_map' in PHENIX 1.18.2 (ref. [60]). The model of the Sr35–AvrSr35 complex was manually built in COOT 0.9 (ref. [61]) based on the global and the local maps. The generated model was refined against the combined Sr35–AvrSr35 EM density using real space refinement in PHENIX with secondary structure and geometry restraints[61]. Model statistics can be found in Extended Data Table 1. USCF Chimera 1.15 and ChimeraX 1.15 were used to visualize models and density maps.

Transient gene expression assays in wheat protoplasts

Seedlings of the wheat cultivar. Chinese Spring were grown at 19 °C, 70% humidity and under a 16 h photoperiod. Protoplasts were isolated from the leaves and transfected as previously described[23]. The coding sequences of *TaSh1* (NCBI XP_044359492.1) and *HvSh1* (NCBI KAE8803279.1) were generated by gene synthesis based on wild-type codons (GeneArt, Invitrogen). The coding sequence of all tested receptor constructs, or an EV as negative control, were expressed from *pIPKb002* vector[62] containing the strong ubiquitin promoter. Receptors were co-expressed with *AvrSr35* in *pIPKb002*. In addition, cotransfection of *pZmUBQ:LUC*[63] facilitated the expression of the *LUC* reporter construct. Each treatment was transfected with 4.5 µg of *pZmUBQ:LUC* and 5 µg of *pIPKb002:AvrSr35*. Quantities of receptor-encoding *pIPKb002* plasmid were varied for each construct in an effort to minimize cell death due to (receptor) toxicity-mediated cell death (*EV* 8 µg; *Sr35* and *Sr35* mutants 2 µg; *AvrSr35* and *AvrSr35* mutants 5 ug; *HvMla10*, *HvMla13*, *HvMla10*^{Sr35LRR}, *HvMla13*^{Sr35LRR}, *TaSh1*, *TaSh1*, *TaSh1*^{GOF}, *TaSh1*^{GOF} 8 µg; *TaSh1*^{Sr35LRR} and *TaSh1*^{Sr35LRR} 2 µg). A maximum of two technical replicates were completed with the same batch of wheat seedlings. Luminescence was measured using a luminometer (Centro, LB960). Relative luminescence was calculated by dividing the absolute luminescence value by that of the corresponding *EV* treatment (EV = 1).

Transient gene expression and western blotting in tobacco

For *N. benthamiana* transient gene expression, *Sr35* and *Sr35* mutants, *AvrSr35* and *AvrSr35* mutants were cloned into the *pDONR* vector (Invitrogen). The obtained plasmids of *Sr35* and *Sr35* mutants were recombined by an LR clonase II (Thermo Fisher Scientific) reaction into *pGWB517-4×Myc* with a C-terminally fused 4×Myc epitope tag[64], while *AvrSr35* and *AvrSr35* mutants were recombined into the *pXCSG-mYFP*[65] vector with a C-terminally fused mYFP epitope tag. After being verified by Sanger sequencing, all the constructs were transformed into *Agrobacterium tumefaciens* GV3101 pMP90RK by electroporation. Transformants were grown on LB media selection plates containing rifampicin (15 mg ml^{-1}), gentamycin (25 mg ml^{-1}), kanamycin (50 mg ml^{-1}), and spectinomycin (50 mg ml^{-1}) for transformants harbouring *pGWB517-4×Myc* or carbenicillin (50 mg ml^{-1}) for *pXCSG-mYFP*.

Individual *Agrobacterium* transformants were picked and cultured in LB medium containing respective antibiotics in the abovementioned concentration. After shaking culture at 28 °C for 16 h, the culture was harvested at 3,800 r.p.m. for 10 min and resuspended with infiltration buffer containing 10 mM MES pH 5.6, 10 mM $MgCl_2$ and 150 μM acetosyringone. The OD_{600} of *AvrSr35* and *AvrSr35* mutant strains was adjusted to 1.0. For *Sr35* and *Sr35* substitution mutants, the OD_{600} was adjusted to 0.15. Hybrid receptor bacterial strains (*HvMla10*^{Sr35LRR}, *HvMla13*^{Sr35LRR}, *TaSh*^{Sr35LRR}, *HvSh*^{Sr35LRR}) were adjusted to an OD_{600} of 0.6. In the hybrid receptor gain-of-function experiment, the OD_{600} of *TaSh1*, *HvSh1*, *TaSh1*^{GOF} and *HvSh1*^{GOF} bacterial strains was adjusted to 1.8 without resulting in cell death in co-expression of *TaSh1* and *HvSh1* when co-expressed with *AvrSr35*. After dilution, all the cell suspensions were incubated at 28 °C for 1 h at 200 rpm. Construct expression was conducted in leaves of four-week-old *N. benthamiana* plants via *Agrobacterium*-mediated transient expression assays. For phenotypic experiments, *Agrobacteria* cultures expressing receptor constructs, or the respective receptor mutants, were co-infiltrated with *AvrSr35*, or its mutants, at 1:1 ratio using a syringe. As a control, either receptor or effector bacterial strains were replaced with *Agrobacteria* transformed with EVs. Phenotypic data were recorded at day 3 after infiltration.

Agrobacterium-mediated transient expression assays for protein detection were conducted as described above. The infiltrated leaves were harvested at 24 h after infiltration, flash-frozen in liquid nitrogen and ground to powder using a Retsch grinder. Plant powder was mixed with 4xLämmli buffer in a 1:2 ratio. Five microlitres was loaded onto 10% SDS–PAGE. After transfer to PVDF membrane, protein was detected using monoclonal mouse anti-MYC (1:3,000; R950-25, Thermofisher), polyclonal rabbit anti-GFP (1:3,000; pabg1, Chromotek), polyclonal goat anti-mouse IgG-HRP (1:7,500; ab6728, Abcam) and polyclonal swine anti-rabbit IgG-HRP (1:5,000; PO399, Agilent DAKO) antibodies. Protein was detected using SuperSignal West Femto:SuperSignal substrates (ThermoFisher Scientific) in a 1:1 ratio.

Electrophysiology

The TEVC recordings were conducted as previously described[4]. The cDNAs of *Sr35*, or *Sr35* mutants, and *AvrSr35* were cloned into the *pGHME2* plasmid for expression in *Xenopus* oocytes. cRNAs for all constructs were transcribed using T7 polymerase. Ovarian lobes were obtained from adult *Xenopus laevis* under anaesthesia. Both the amount of cRNA injected and the oocyte incubation time were optimized to minimize toxicity caused by the assembled Sr35 resistosome. Isolated oocytes were co-injected with 0.5 ng cRNA of *Sr35* (WT and mutants) and *AvrSr35*. Oocytes were then incubated at 18 °C for approximately 4 h in ND96 buffer (96 mM NaCl, 2.5 mM KCl, 1 mM $MgCl_2$, 1.8 mM $CaCl_2$, 5 mM HEPES pH 7.6) supplemented with 10 μg l^{-1} penicillin and 10 μg l^{-1} streptomycin. TEVC measurements were performed between 4–7 h later after injection. Water-injected oocytes served as controls.

Two-electrode voltage-clamp recordings were performed using an OC-725C oocyte clamp amplifier (Warner Instruments) and a Digidata 1550 B low-noise data acquisition system with pClamp 10.6 software (Molecular Devices). Data were analysed using OriginPro, 2022 (OriginLab). The microelectrode solutions contained 3 M KCl (electrical resistance of 0.5–1 MΩ), and the bath electrode was a 3 M KCl agar bridge. To eliminate the chloride currents mediated by endogenous Ca^{2+}-activated chloride channels in Xenopus oocytes, the ND96 recording solution was supplemented with 200 μM CaCC inhibitor (CaCCinh)-A01, and the oocytes were pre-incubated 5–10 min before measurement. To test the channel blocking effect of $LaCl_3$, the oocytes were pre-incubated for 5–10 min in the recording solutions supplemented with 200 μM CaCCinh-A01 and 100 μM $LaCl_3$ before measurement. For the recordings in Fig. 3g, the various recording solutions were as follows: KCl (96 mM), K-gluconate (96 mM), NaCl (96 mM), Na-gluconate (96 mM) and TBA-Cl (96 mM). All solutions contained 5 mM HEPES pH 7.6, and 1 mM $MgCl_2$ or Mg-gluconate. For the recordings in Fig. 3h, the various recording solutions were as follows: $CaCl_2$ (12 mM), Ca-gluconate (12 mM), $MgCl_2$ (12 mM) and Mg-gluconate (12 mM). All solutions contain 5 mM HEPES pH 7.6, and 1 mM $MgCl_2$ or Mg-gluconate. The treatments of CaCCinh-A01 and $LaCl_3$ were conducted as above. Voltage-clamp currents were measured in response to voltage steps lasting 7.5 s and to test potentials ranging from −110 mV to +70 mV, in 20 mV increments. Before each voltage step, the membrane was held at 0 mV for 1.60 s, and following each voltage step, the membrane was returned to 0 mV for 2 s. *I–V* relations for Sr35 resistosome channels were generated from currents that were measured 0.2 s by the end of each test voltage step. Three independent batches of oocytes were investigated and showed consistent findings. Data from one representative oocyte batch are shown.

Statistics and reproducibility

No statistical method was used to predetermine sample size. Sample size was chosen in accordance with the generally accepted standards of the respective scientific field. Data distribution for each protoplast transfection experiment was subjected to the Shapiro-Wilk normality test. All experiments were found to be normally distributed. An ANOVA and subsequent Tukey post hoc test was completed for each experiment. Treatments found to be significantly different were labelled with different letters ($\alpha = 0.05$). All statistical output is listed in Supplementary Information.

Purification of the Sr35 resistosome was performed more than 10 times. Pull-down and SDS analysis were highly reproducible between biological replicates and comparable with Extended Data Fig. 1b,c. Negative staining was performed for each protein preparation and showed some variability compared to Fig. 1a, but generally yielded >20% star-shaped particles. Cryo-EM datasets were recorded twice from independent protein preparations (micrograph of one cryo-EM sample preparation shown in Extended Data Fig. 1d) and yielded highly similar cryo-EM density maps.

Insect cell death data were performed with six biological replicates and yielded comparable results to Extended Data Fig. 1a.

Tobacco agroinfiltration data was performed with at least two biological replicates for each substitution mutant and always simultaneously with western blot analysis. Technical replicates of one dataset are shown as raw image data. Western blot samples were always obtained from the same biological replicate as the phenotypic data. Only phenotypic data for which the western blot gave a clear signal are shown.

Ethics declarations

The animal study (*Xenopus laevis*) was reviewed and approved by the Laboratory Animal Ethics Committee at Institute of Genetics and Developmental Biology, Chinese Academy of Sciences, Beijing, China with the approval ID AP2020029.

Reporting summary

Further information on research design is available in the Nature Research Reporting Summary linked to this article.

Data availability

The atomic coordinates of the Sr35 resistosome have been deposited in the Protein Data Bank (PDB) with the accession code 7XC2. The EM map for the local mask of Sr35 LRR in complex with AvrSr35 has been deposited in the Electron Microscopy Data Bank (EMDB) with the accession code EMD-33111. Sequences of *TaSh1* and *HvSh1* are available at NCBI under accession codes XP_044359492.1 and KAE8803279.1, respectively. Source data of tobacco agroinfiltrations, western blots, insect cell viability and wheat protoplast cell death are provided with this manuscript. All plasmids are available from the authors.

Code availability

No custom codes were generated for this study.

50. Trowitzsch, S., Bieniossek, C., Nie, Y., Garzoni, F. & Berger, I. New baculovirus expression tools for recombinant protein complex production. *J. Struct. Biol.* **172**, 45–54 (2010).
51. Zheng, S. Q. et al. MotionCor2: anisotropic correction of beam-induced motion for improved cryo-electron microscopy. *Nat. Methods* **14**, 331–332 (2017).
52. Mindell, J. A. & Grigorieff, N. Accurate determination of local defocus and specimen tilt in electron microscopy. *J. Struct. Biol.* **142**, 334–347 (2003).
53. Scheres, S. H. W. RELION: implementation of a Bayesian approach to cryo-EM structure determination. *J. Struct. Biol.* **180**, 519–530 (2012).
54. Scheres, S. H. W. A Bayesian view on cryo-EM structure determination. *J. Mol. Biol.* **415**, 406–418 (2012).
55. Scheres, S. H. W. in *Methods in Enzymology* Vol. 579 (ed. R. A. Crowther) 125–157 (Academic Press, 2016).
56. Rosenthal, P. B. & Henderson, R. Optimal determination of particle orientation, absolute hand, and contrast loss in single-particle electron cryomicroscopy. *J. Mol. Biol.* **333**, 721–745 (2003).
57. Kucukelbir, A., Sigworth, F. J. & Tagare, H. D. Quantifying the local resolution of cryo-EM density maps. *Nat. Methods* **11**, 63–65 (2014).
58. Bai, X.-c, Rajendra, E., Yang, G., Shi, Y. & Scheres, S. H. W. Sampling the conformational space of the catalytic subunit of human γ-secretase. *eLife* **4**, e11182 (2015).
59. Pettersen, E. F. et al. UCSF Chimera–a visualization system for exploratory research and analysis. *J. Comput. Chem.* **25**, 1605–1612 (2004).
60. Adams, P. D. et al. PHENIX: a comprehensive Python-based system for macromolecular structure solution. *Acta Crystallogr. D* **66**, 213–221 (2010).
61. Emsley, P., Lohkamp, B., Scott, W. G. & Cowtan, K. Features and development of Coot. *Acta Crystallogr. D* **66**, 486–501 (2010).
62. Himmelbach, A. et al. A set of modular binary vectors for transformation of cereals. *Plant Physiol.* **145**, 1192–1200 (2007).
63. Müller, J. et al. Conserved ERAD-like quality control of a plant polytopic membrane protein. *Plant Cell* **17**, 149–163 (2005).
64. Nakagawa, T. et al. Development of series of gateway binary vectors, pGWBs, for realizing efficient construction of fusion genes for plant transformation. *J. Biosci. Bioeng.* **104**, 34–41 (2007).
65. Wiermer, M. *Molecular and spatial characterisation of Arabidopsis EDS1 defence regulatory complexes.* Inaugural dissertation, Universität zu Köln (2005).

Acknowledgements We acknowledge Zhengzhou University and EMBL Heidelberg for their assistance with cryo-EM data acquisition. We thank U. Neumann (Max Planck Institute for Plant Breeding Research, Cologne, MPIPZ) and F. Babatz (CECAD, Cologne) for TEM support, J. Jirschitzka for technical support (MPIPZ) and N. Donnelly (MPIPZ) for manuscript polishing. We thank our funding bodies: the Alexander von Humboldt Foundation (a Humboldt professorship to J. Chai), the Max-Planck-Gesellschaft (P.S.-L. and a Max Planck fellowship to J. Chai), Deutsche Forschungsgemeinschaft SFB-1403-414786233 (J. Chai and P.S.-L.) and Germany's Excellence Strategy CEPLAS (EXC-2048/1, Project 390686111) (J. Chai and P.S.-L.), iNEXT-Discovery for funding Cryo-EM dataset collection at EMBL Heidelberg (PID 16414 to A.F. and J. Chai), the National Key Research and Development Program of China 2021YFA1300701 (Z.H.), the Strategic Priority Research Program of the Chinese Academy of Sciences (XDA24020305 to Y.C.) and the National Key Research and Development Program of China (2020YFA0509903 to Y.C.).

Author contributions A.F. and J. Chai conceived the study. A.F., Y.C., P.S.-L. and J. Chai conceptualized the study. A.F., Y.C., P.S.-L. and J. Chai acquired funding. A.F., E. Li, A.W.L., Y. D., and J. Chang designed the experiments. A.F. and E. Li performed the biochemistry; and A.F., E.Li and Y.S. acquired the structure. J.W. and X.Z. assisted during structure study. A.F., E. Li, A.W.L. and E. Logemann performed plant functional studies. Y.D. performed electrophysiology study. A.F., E. Li, A.W.L., Y.D., Z.H. and Y.C. analysed the data. A.F., P.S.-L., J. Chai and Y.C. wrote the manuscript with input from all authors.

Funding Open access funding provided by Max Planck Society.

Competing interests The authors declare no competing interests.

Additional information

Supplementary information The online version contains supplementary material available at https://doi.org/10.1038/s41586-022-05231-w.

Correspondence and requests for materials should be addressed to Yuhang Chen, Paul Schulze-Lefert or Jijie Chai.

Peer review information *Nature* thanks Peter Dodds, Bostjan Kobe and the other, anonymous, reviewer(s) for their contribution to the peer review of this work. Peer reviewer reports are available.

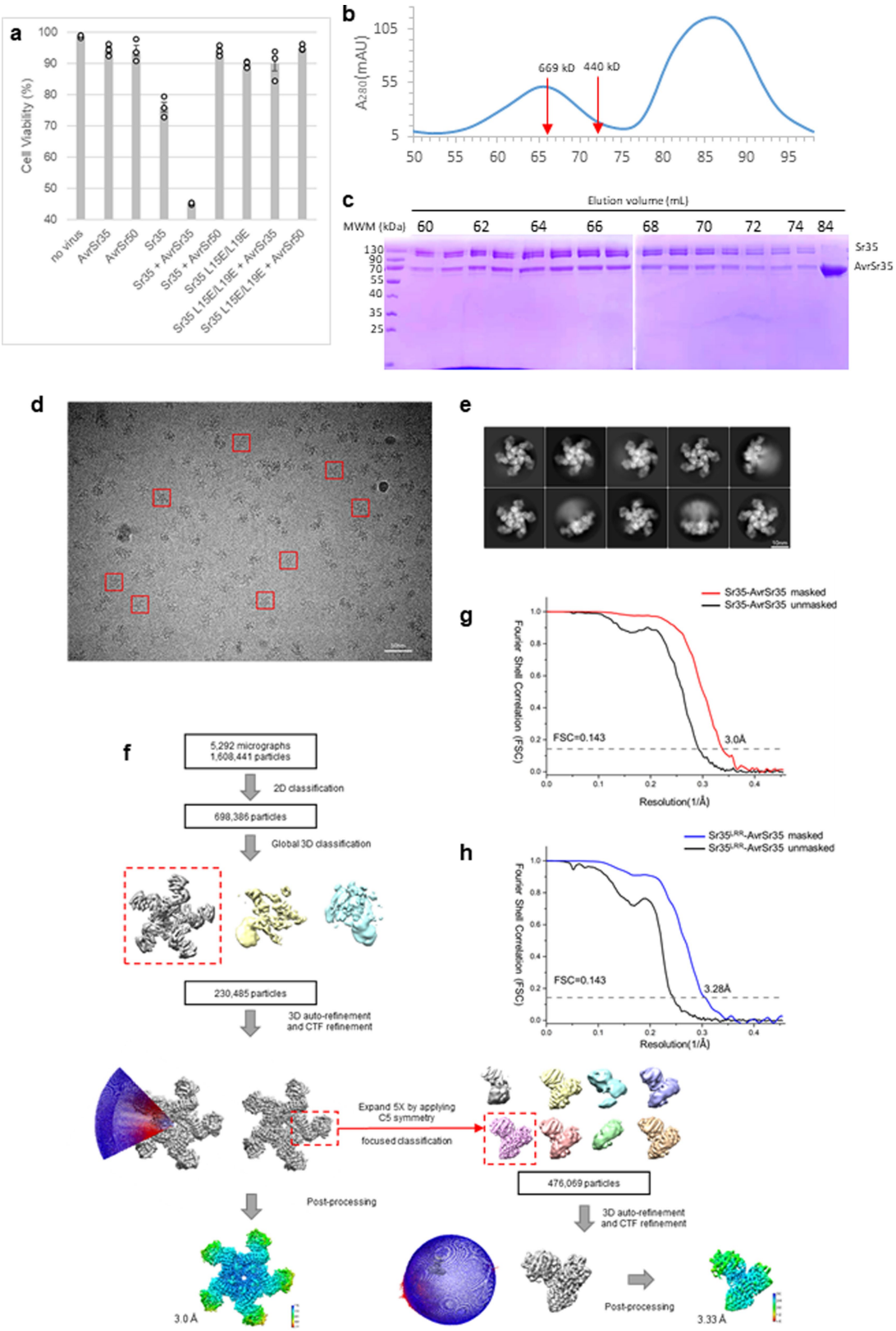

Extended Data Fig. 1 | Sr35-AvrSr35 complex reconstitution in Sf21 insect cells. a, Cell viability data in Sf21 insect cells. Sr35 constructs carrying amino-terminal 6xHis-Sumo-tag and Avr35 constructs carrying N-terminal GST-tag. Cell viability was determined using trypan blue stain (mean ± SEM; n = 3 technical replicates). Six biological replicates were performed with comparable results. **b**, Chromatogram of Sr35-AvrSr35 resistosome purification using HiLoad S6 column. Red arrows corresponding to 669 kDa (66 mL) thyroglobulin molecular weight marker, 440 kDa (72 mL) to ferritin. **c**, SDS–PAGE of individual fractions collected in (b). Numbers represent elution volumes. Molecular weight marker (MWM) on left. **d**, Representative cryo-EM micrograph of Sr35-AvrSr35 complex. **e**, Representative 2D class averages of Sr35-AvrSr35 complex. **f**, Flowchart of cryo-EM data processing and Sr35-AvrSr35 3D reconstruction. **g**, FSC curves at 0.143 of the final model of Sr35-AvrSr35 complex. **h**, FSC curves at 0.143 of the final model of Sr35LRR-AvrSr35.

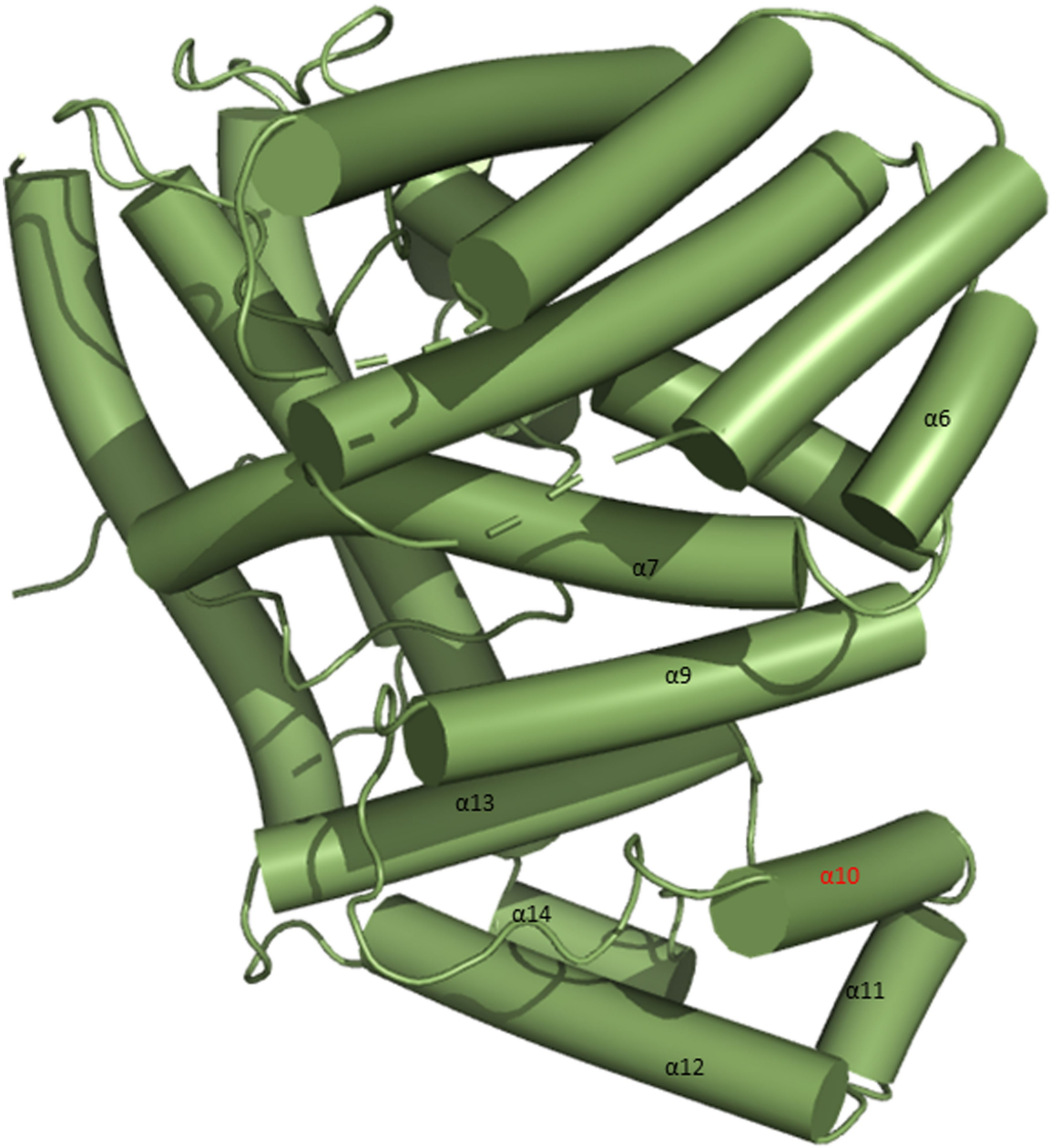

Extended Data Fig. 2 | AvrSr35 structure from the Sr35 resistosome. α10-helix (red) is involved in most extensive contacts with Sr35 LRR.

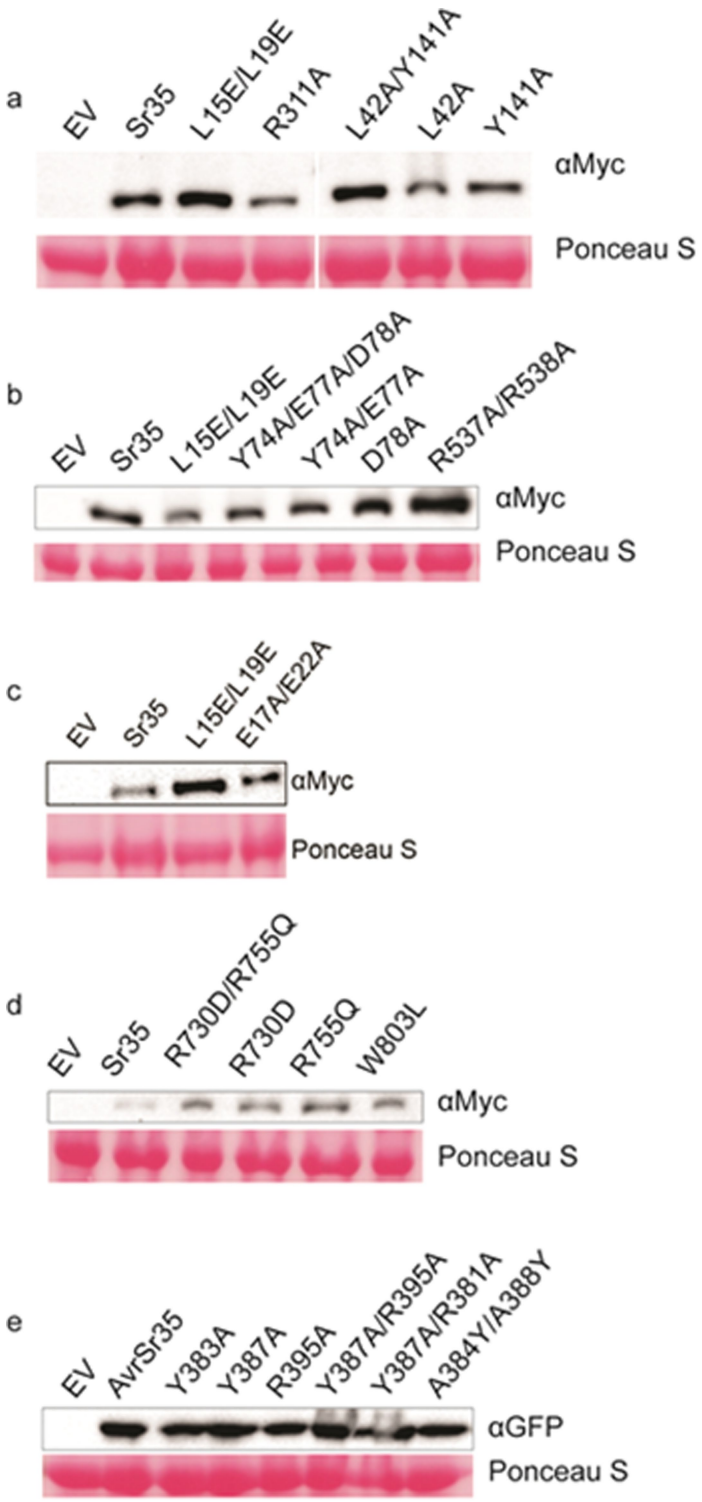

Extended Data Fig. 3 | Western blot of *N. benthamiana* experiments. Pooled samples from 3 technical replicates. Ponceau S staining as a loading control. **a**, Sr35 NBD ATP-binding and coiled-coil protomer interface mutants. Myc-tagged protein. Left and right side merged from the same blot. **b**, Sr35 EDVID and arginine-cluster mutants. Myc-tagged protein. Last lane cropped from the same blot. **c**, Sr35 channel mutants. Myc-tagged protein. **d**, Sr35 LRR mutants. Myc-tagged protein. **e**, AvrSr35 mutants. YFP-tagged protein detected by GFP antibody.

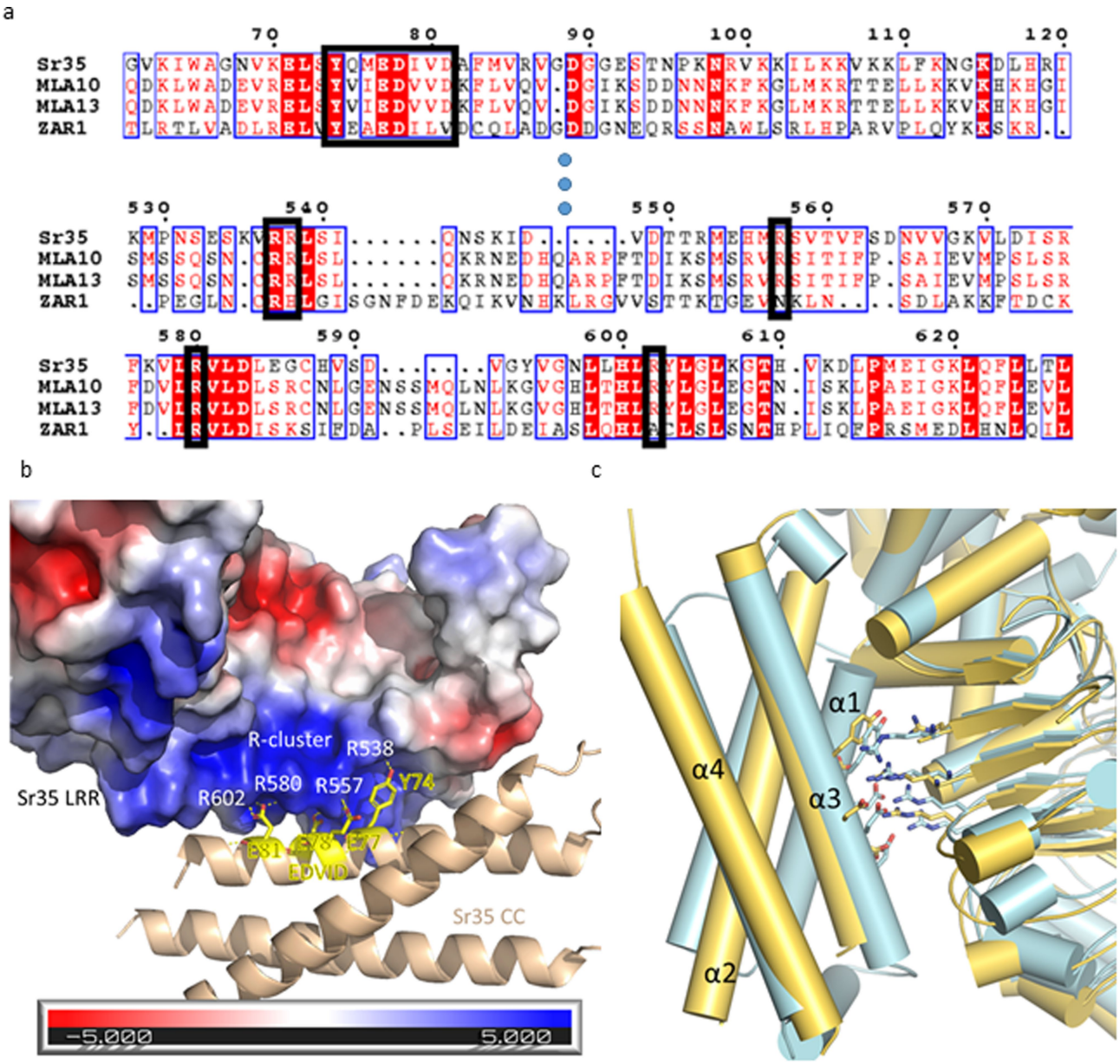

Extended Data Fig. 4 | Details of EDIVD and R-cluster. a, Multiple protein sequence alignment of *Hv*MLA10, *Hv*MLA13, Sr35 and ZAR1. Amino acids highlighted in red and in red text are identical and possess similar properties, respectively. Alignment of the EDIVD motif and arginine cluster are boxed in black (Robert and Gouet 2014). **b**, Electrostatic surface charge of Sr35 LRR around the EDVID motif. **c**, Structural alignment of Sr35 inactive structure prediction (cyan) and one protomer (yellow) from Sr35 resistosome. Detailed view of EDVID and arginine cluster interactions. In analogy to ZAR1, the Sr35 coiled-coil (CC) α1-helix might undergo structural rearrangement, which likely requires EDVID with arginine cluster interactions to transiently resolve.

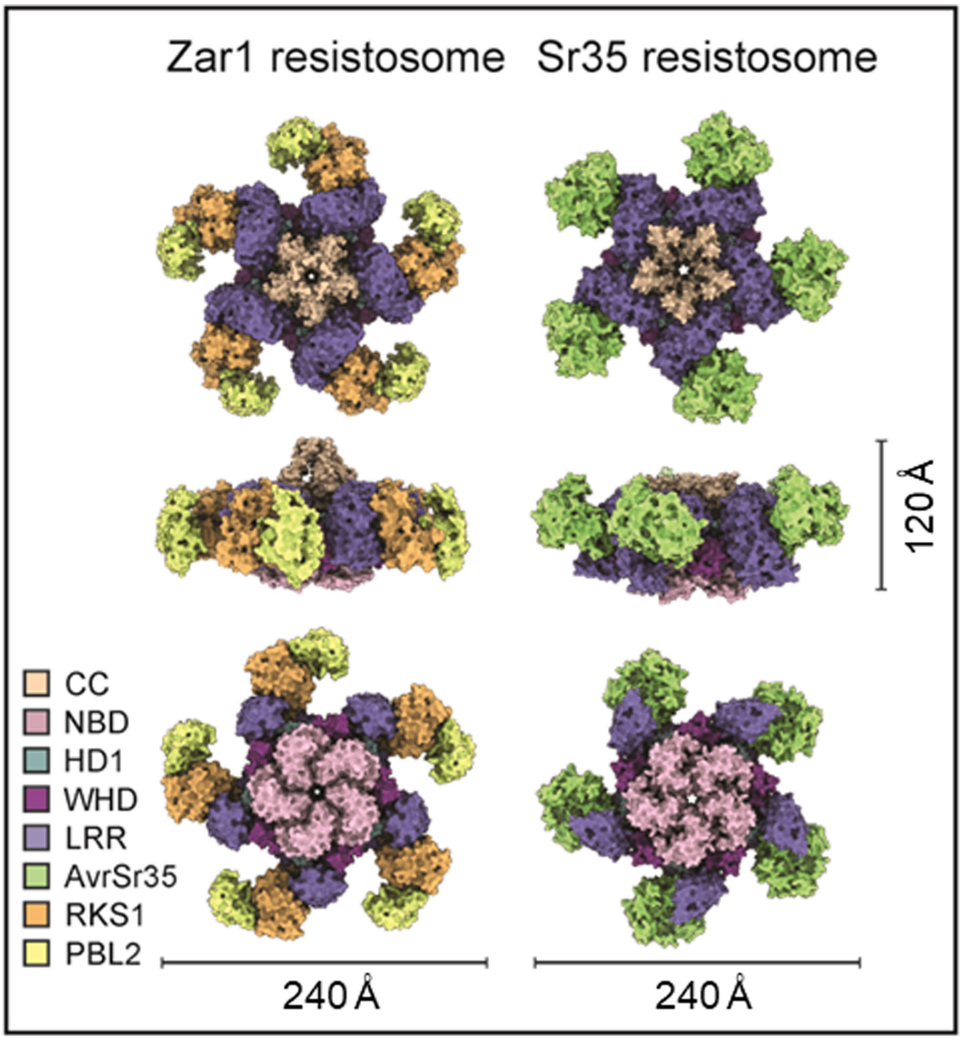

Extended Data Fig. 5 | CNL resistosome structural conservation. The structures (in surface representation) of the ZAR1 resistosome and the Sr35 resistosome are shown. Zar1 is indirectly activated by the host proteins PBL2 and RKS1. Sr35 is directly activated by the fungal effector AvrSr35. The first, second, and third row show the top, side, and bottom views of these structures, respectively. Domains are coloured according to in-figure legend. Sizes are indicated by scale bar.

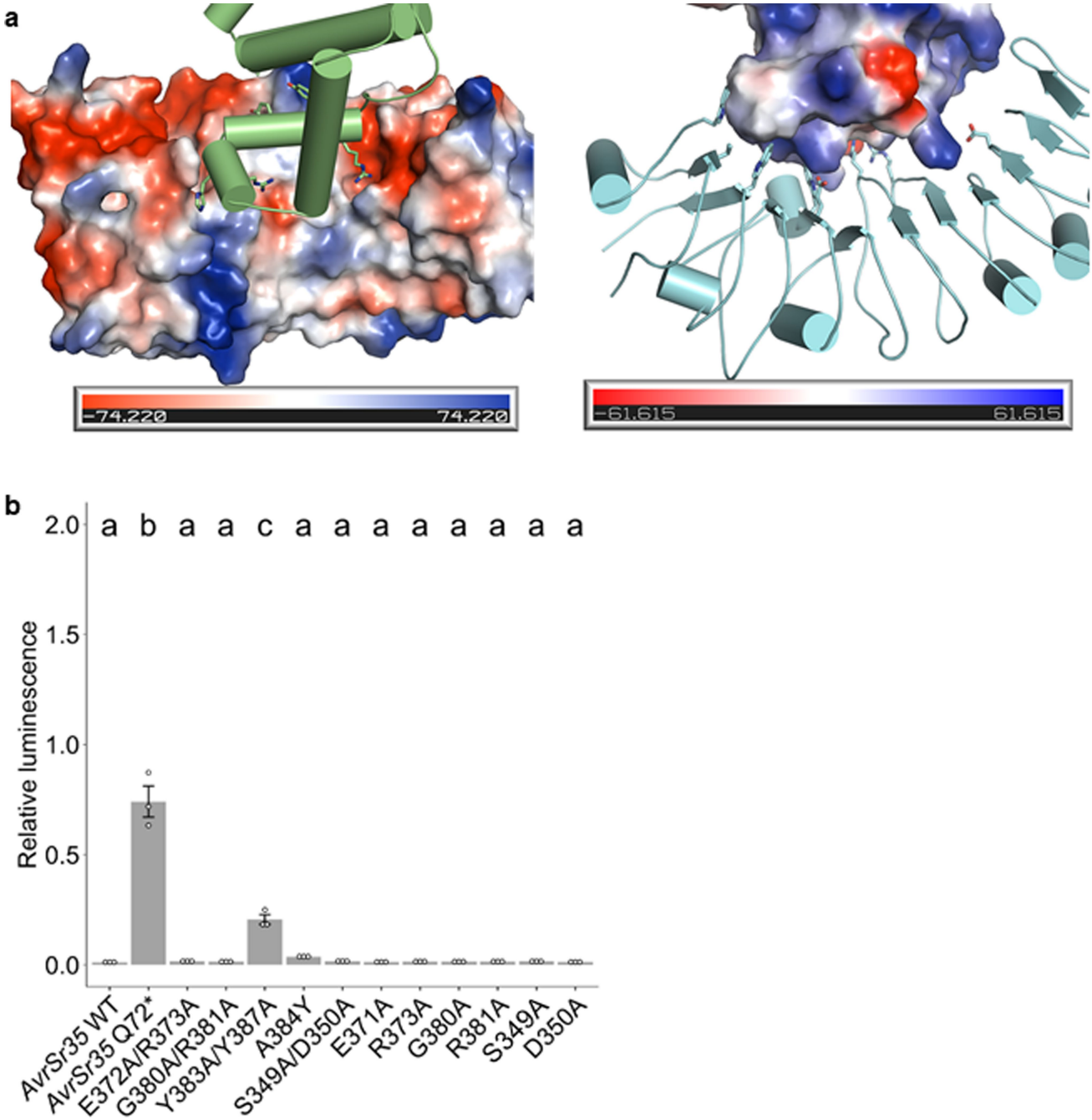

Extended Data Fig 6 | Recognition of AvrSr35 effector by Sr35 LRR domain. **a**, Shape and charge complementarity of Sr35 LRR and AvrSr35 at their interface. (Left) AvrSr35 shown as cartoon (lime) and Sr35 as electrostatics surface model. (Right) Sr35 LRR shown as cartoon (cyan) and AvrSr35 as electrostatics surface model. **b**, Wheat protoplast data of AvrSr35 mutants predicted to impair Sr35 recognition. Relative luminescence as readout for cell death. Empty vector treatment defined the relative baseline (mean ± SEM; $n = 3$). Test statistics derived from ANOVA and Tukey post hoc tests ($P < 0.05$). Exact p values provided in Supplementary Table 3.

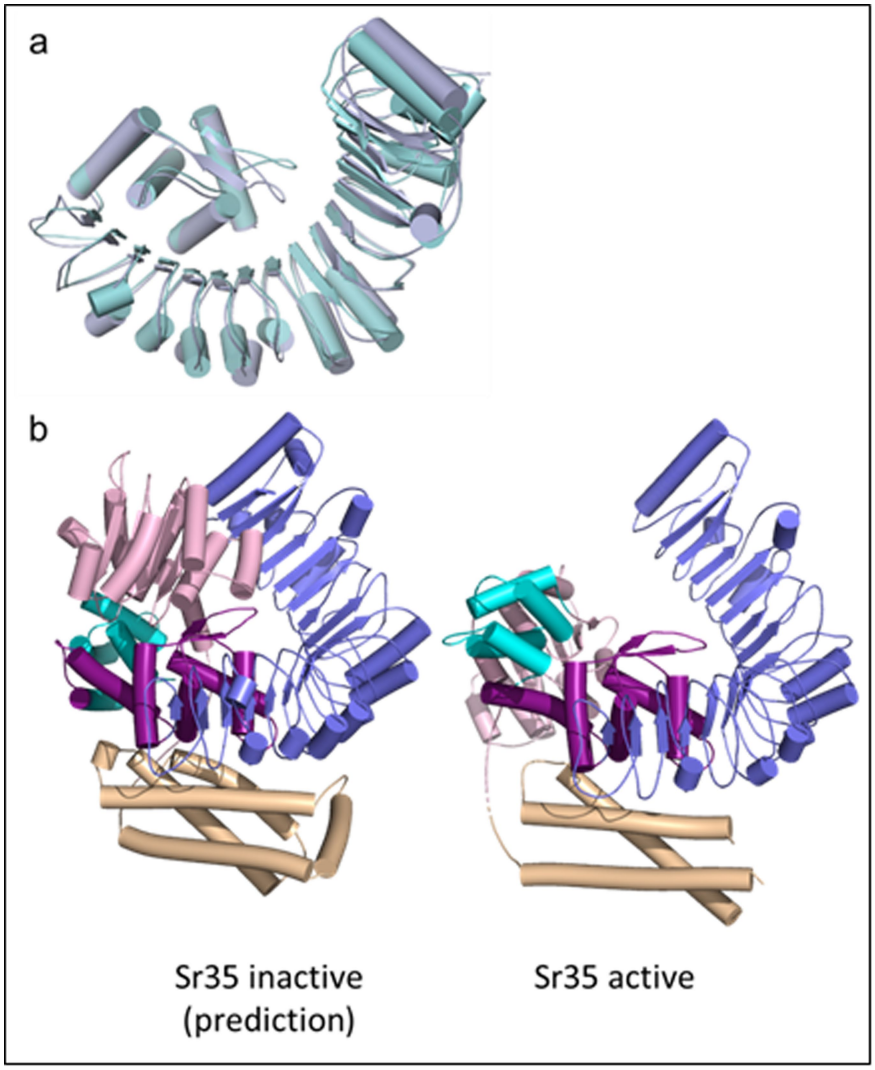

Extended Data Fig. 7 | Comparison of the Sr35 prediction (AlphaFold2) with the Sr35 protomer from the cryo-EM structure. a, Structural alignment of WHD and LRR domains from Sr35 AlphaFold2 prediction (cyan) and from Sr35 resistosome Cryo-EM structure (blue). **b**, Structural comparison of monomeric Sr35 from prediction (left) and from Cryo-EM structure (right). Substantial differences exist highlighting the structural re-organization within the NOD module (NBD-HD1 relative to WHD). Domain color code: coiled-coil (yellow), NBD (light pink), HD1 (cyan), WHD (purple), and LRR (blue).

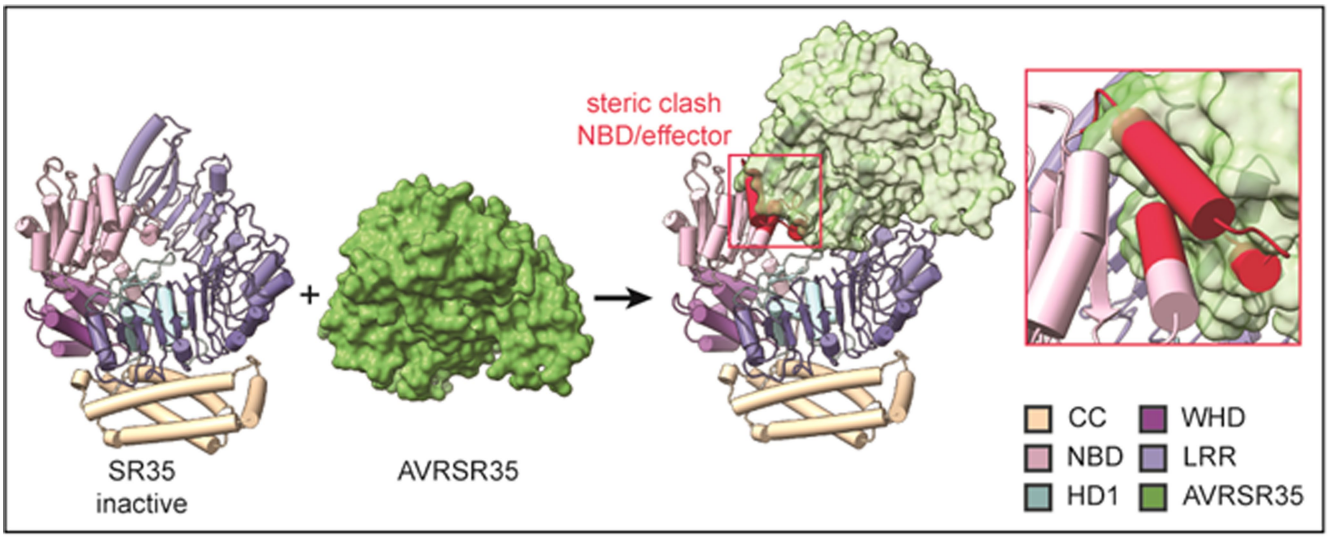

Extended Data Fig. 8 | Steric clash between AvrSr35 and Sr35 NBD mediates Sr35 receptor activation. Inactive Sr35 inside the cell comes in contact with Pgt effector AvrSr35. In avoidance of a steric clash (red) between AvrSr35 and the Sr35 NBD domain, the Sr35 NBD domain is forced to structurally rearrange and a 'primed' receptor-effector complex is formed. Full activation and oligomerization requires subsequent ADP release, ATP binding and, NOD module rearrangement and coiled-coil (CC) domain structural rearrangement. Sr35 domains and AvrSr35 are coloured according to in-figure legend.

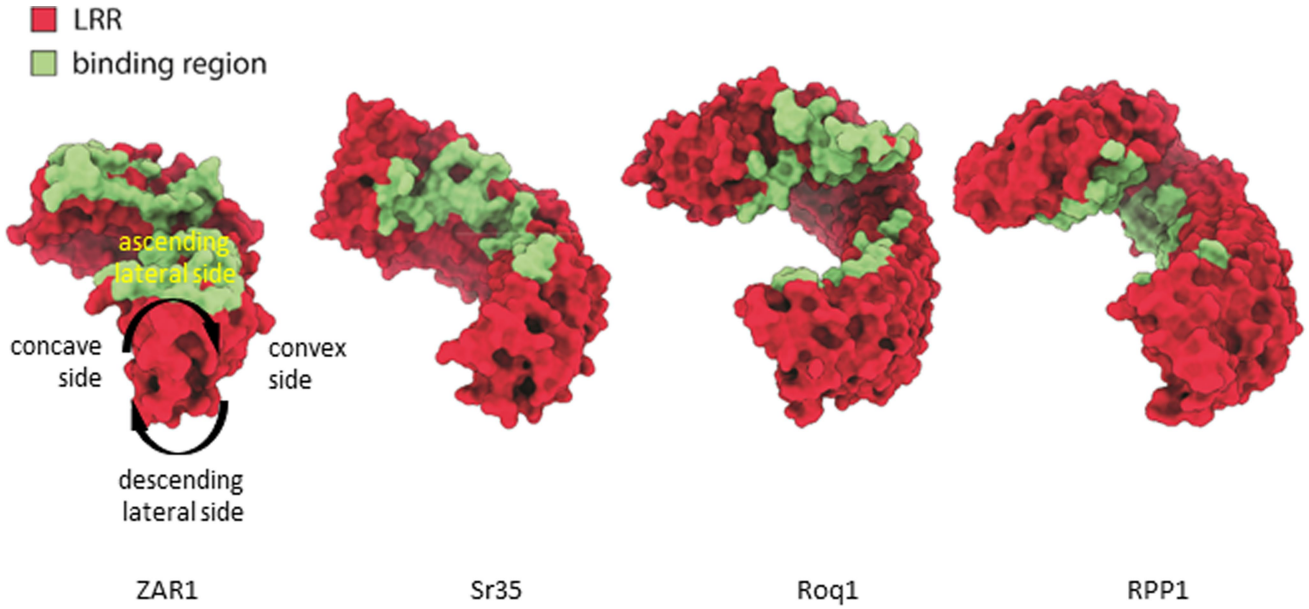

Extended Data Fig. 9 | Comparison of ZAR1, Sr35, ROQ1, RPP1 ligand binding sites. Ligand binding to LRR of CNLs (Zar1, Sr35) and LRR-CJID of TNLs (Roq1, RPP1) occurs in equivalent region in the ascending lateral side of the LRR domain (compare concave, convex, ascending and descending lateral sides defined on Zar1).

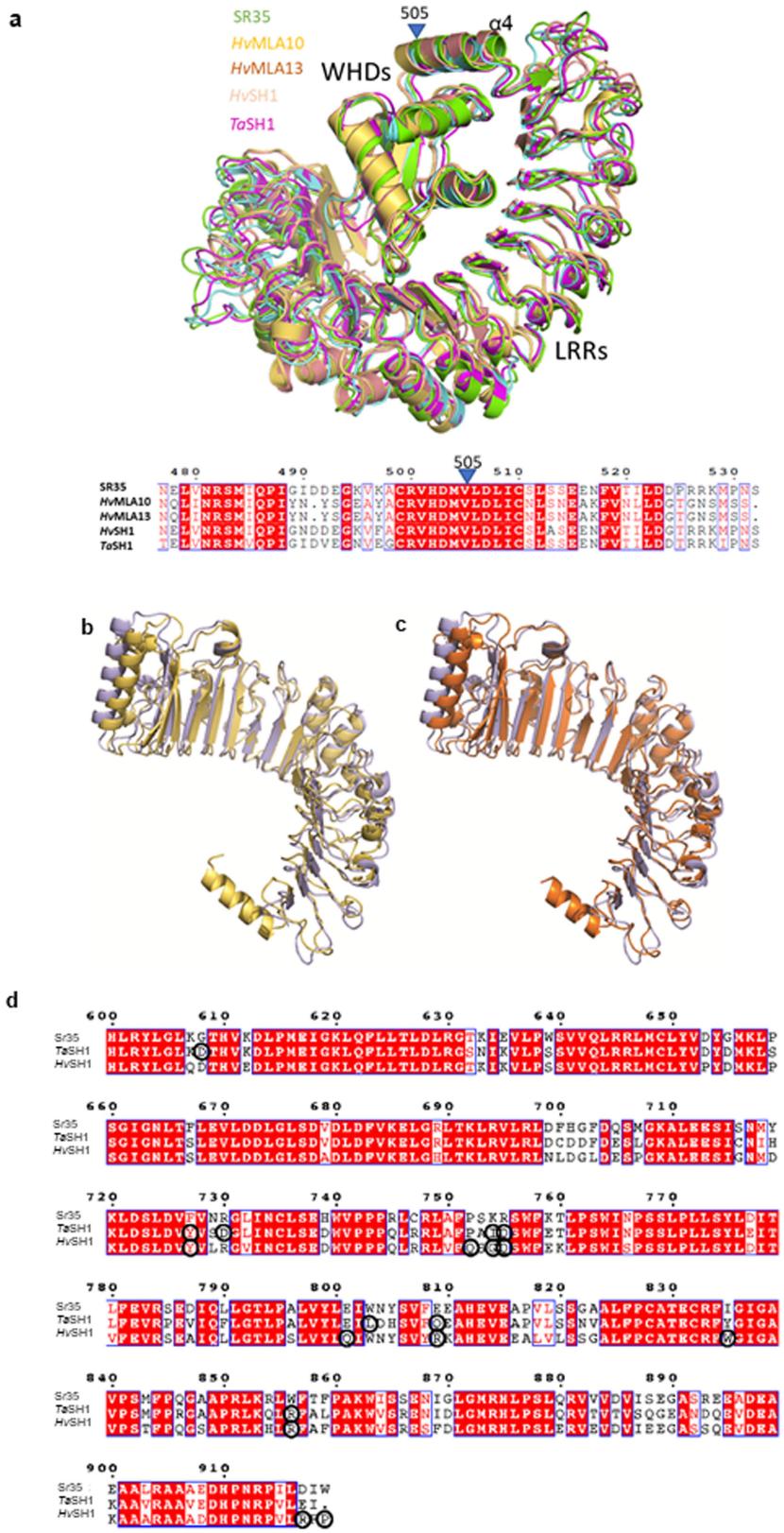

Extended Data Fig. 10 | Rationale for hybrid receptor design. a, Structural (top) and sequence (bottom) alignment of Sr35, HvMLA10, HvMLA13, TaSH1 and HvSH1. Amino acid 505 in the structurally and sequence conserved α4-helix of the WHD of Sr35 was included in hybrid CNL receptors. Structure of Sr35 is isolated from the cryo-EM Sr35 resistosome structure, while *Hv*MLA10, *Hv*MLA13, *Ta*SH1 and *Hv*SH1 were predicted using AlphaFold2. **b**, Structural alignment of Sr35 LRR (light blue) with structural prediction of *Ta*Sh1 (yellow) and **c**, *Hv*Sh1 (orange). **d**, Multiple protein sequence alignment of Sr35, *Ta*SH1 and *Hv*SH1. Circled amino acids were substituted to corresponding amino acids in the Sr35 sequence for the generation of *TaSh1*^{GOF} and *HvSh1*^{GOF} constructs. Amino acids highlighted in red and in red text are identical and possess similar properties, respectively.

Extended Data Table 1 | Cryo-EM data collection, refinement and validation statistics

	Sr35-AvrSr35	Sr35^{LRR}-AvrSr35
PDB and EMDB ID	7XC2 EMD-33112	EMD-33111
Data collection		
Cryo electron microscope	FEI Titan Krios	
Voltage (kV)	300	
Detector	Gatan K3 Summit	
Energy filter slit width (eV)	20	
Magnification	81,000x	
Pixel size (Å)	1.1	
Total electron exposure (e^-/Å^2)	50	
Number of frames collected	32	
Defocus range (mm)	-1.5 ~ -2.0	
Automation software	EPU2	
Micrographs collected	5,292	
Micrographs used	5,292	
3D reconstruction		
Software	RELION 3.1	RELION 3.1
Total extraced particles	1,608,441	1,152,425
Total number particles for final refinement	230,485	476,069
Symmetry imposed	C5	C1
Resolution range (Å)	2.8~5.7	3.25~4.66
Resolution (Å) after refinement (FSC=0.143)	3.41	4.00
Resolution (Å) after post-processing (FSC=0.143)	3.00	3.33
Map sharpening B-factor (Å^2)	-60	-60
Refinement and validation		
Software	Phenix.real_space_refine	None
Model resolution (Å)	3.0 (FSC=0.5)	
Model composition		
Non-hydrogen atoms	52070	
Protein residues	6445	
Map-model CC (overall/local)	0.89/0.88	
B factors (Å^2)	134	
R.M.S deviations		
Bonds lengths (Å)	0.003	
Bonds angles (°)	0.580	
MolProbity score	1.76	
Clash score	6.54	
Rotamer outliers (%)	1.1	
Cb outliers (%)	0.00	
CaBLAM outliers (%)	2.47	
EMRinger score	2.27	
Ramachandran plot statistics		
Preferred (%)	94.65	
Allowed (%)	5.35	
Outlier (%)	0.00	

nature portfolio

Corresponding author(s): Jijie Chai, Alexander Förderer, Yuhang Chen

Last updated by author(s): Jun 25, 2022

Reporting Summary

Nature Portfolio wishes to improve the reproducibility of the work that we publish. This form provides structure for consistency and transparency in reporting. For further information on Nature Portfolio policies, see our Editorial Policies and the Editorial Policy Checklist.

Statistics

For all statistical analyses, confirm that the following items are present in the figure legend, table legend, main text, or Methods section.

n/a	Confirmed	
☐	☒	The exact sample size (*n*) for each experimental group/condition, given as a discrete number and unit of measurement
☐	☒	A statement on whether measurements were taken from distinct samples or whether the same sample was measured repeatedly
☐	☒	The statistical test(s) used AND whether they are one- or two-sided *Only common tests should be described solely by name; describe more complex techniques in the Methods section.*
☐	☒	A description of all covariates tested
☐	☒	A description of any assumptions or corrections, such as tests of normality and adjustment for multiple comparisons
☐	☒	A full description of the statistical parameters including central tendency (e.g. means) or other basic estimates (e.g. regression coefficient) AND variation (e.g. standard deviation) or associated estimates of uncertainty (e.g. confidence intervals)
☐	☒	For null hypothesis testing, the test statistic (e.g. *F*, *t*, *r*) with confidence intervals, effect sizes, degrees of freedom and *P* value noted *Give P values as exact values whenever suitable.*
☒	☐	For Bayesian analysis, information on the choice of priors and Markov chain Monte Carlo settings
☒	☐	For hierarchical and complex designs, identification of the appropriate level for tests and full reporting of outcomes
☒	☐	Estimates of effect sizes (e.g. Cohen's *d*, Pearson's *r*), indicating how they were calculated

Our web collection on statistics for biologists contains articles on many of the points above.

Software and code

Policy information about availability of computer code

Data collection	OC-725C oocyte clamp amplifier (Warner Instruments) Titan Krios (Thermo Fisher Scientific), K3 Summit camera (Gatan) luminometer (Centro, LB960)
Data analysis	EPU 2 (Thermo Fisher Scientific) 2.8.1.10REL Relion 3.1 Coot 0.9 PHENIX 1.18.2 USCF Chimera 1.15 ChimeraX 1.15 OriginPro 2022 pClamp 10.6 Pymol Molecular Graphics System 1.7.2.1. GraphPad Prism 8 Microsoft Office Software package (Excel) 2016 RStudio 2021.09.0 Build 351

For manuscripts utilizing custom algorithms or software that are central to the research but not yet described in published literature, software must be made available to editors and reviewers. We strongly encourage code deposition in a community repository (e.g. GitHub). See the Nature Portfolio guidelines for submitting code & software for further information.

Data

Policy information about availability of data

All manuscripts must include a data availability statement. This statement should provide the following information, where applicable:

- Accession codes, unique identifiers, or web links for publicly available datasets
- A description of any restrictions on data availability
- For clinical datasets or third party data, please ensure that the statement adheres to our policy

The atomic coordinates of the Sr35 resistosome have been deposited in the Protein Data Bank with the accession code 7XC2. The EM map for the local mask of Sr35 LRR in complex with AvrSr35 has been deposited in the EMDB with the accession code EMD-33111.
Sequences of TaSh1 and HvSh1 are available at NCBI under accession codes XP_044359492.1 (https://www.ncbi.nlm.nih.gov/protein/XP_044359492.1/) and KAE8803279.1 (https://www.ncbi.nlm.nih.gov/protein/KAE8803279.1), respectively.
Source data of tobacco infiltrations, western blots, insect cell viability and wheat protoplast cell death are provided with this manuscript.

Field-specific reporting

Please select the one below that is the best fit for your research. If you are not sure, read the appropriate sections before making your selection.

☒ Life sciences ☐ Behavioural & social sciences ☐ Ecological, evolutionary & environmental sciences

For a reference copy of the document with all sections, see nature.com/documents/nr-reporting-summary-flat.pdf

Life sciences study design

All studies must disclose on these points even when the disclosure is negative.

Sample size

No statistical methods were used to determine sample size. Sample size was chosen in accordance with the generally accepted standard of the respective scientific field.
The wheat protoplast experiments consisted of a total of five to six replicates. A maximum of two replicates were conducted per batch of wheat seedlings to encompass any variation due to the plant material. Five to six replicates of the wheat protoplast experiments were deemed sufficient due to the consistency of the results. The N. benthamiana infiltration experiments consisted of a minimum of seven biological replicates. Seven replicates are deemed sufficient due to any variation of protein expression in the leaves.
Sample size of Xenopus experiments was chosen based on previous literature (Bi et al. 2021) and deemed sufficient due to the low variation between technical and biological replicates.
More information is given in Statistics and reproducibility.

Data exclusions

No data were excluded from the analyses.

Replication

Generally, repetition was a measure taken to combat experimental variation. The plant data is deemed reproducible due to the use of different batches of plant material in both the wheat protoplast experiments and the N. benthamiana experiments. In addition, different Agrobacterium cultures were used to verify reproducibility of the N. benthamiana experiments.
The Xenopus data is deemed reproducible due to the use of different oocyte batches.
Expression from Sf21 insect cells was generally reproducible whenever the cell culture was in good health. Recovery of star-shaped particles varied according to culture health, baculovirus quality and experimenter performance in protein purification. Generally >20% star-shaped particles were recovered from Sr35 L15E/L19E and AvrSr35 co-expression.
Negative staining and cryo grid preparation are tricky procedures. Variablity of cryo grid preparation was reduced by using Vitrobot automation. Nevertheless, recovery of high quality electron microscopy samples varied significantly.

Randomization

Plant material was selected randomly from a given batch and analyzed equally. Randomization was deemed unnecessary as no sub-sampling was done.

Blinding

Blinding was not deemed relevant for our experiments given the nature of the reagents (plasmids, cRNA) or due to the protein purification work-flow (generally one large-scale purification at a time).

Reporting for specific materials, systems and methods

We require information from authors about some types of materials, experimental systems and methods used in many studies. Here, indicate whether each material, system or method listed is relevant to your study. If you are not sure if a list item applies to your research, read the appropriate section before selecting a response.

Materials & experimental systems

n/a	Involved in the study
☐	☒ Antibodies
☐	☒ Eukaryotic cell lines
☒	☐ Palaeontology and archaeology
☐	☒ Animals and other organisms
☒	☐ Human research participants
☒	☐ Clinical data
☒	☐ Dual use research of concern

Methods

n/a	Involved in the study
☒	☐ ChIP-seq
☒	☐ Flow cytometry
☒	☐ MRI-based neuroimaging

Antibodies

Antibodies used	monoclonal mouse Anti-myc (R950-25, Invitrogen/Thermofisher) c-Myc synthetic peptide: Glu-Gln-Lys-Leu-Ile-Ser-Glu-Glu-Asp-Leu- Species reactivity: Tag. no further validation data available from manufacturer polyclonal goat anti-mouse IgG-HRP (ab6728, Abcam), no further validation data available from manufacturer polyclonal rabbit Anti-GFP; (pabg1, Chromtek), no further validation data available from manufacturer polyclonal swine anti-rabbit IgG-HRP (PO399, Agilent DAKO)
Validation	Antibodies were not validated in-house and not validated by the manufacturer (see above). However, antibodies were deemed reliable due to entries in 'antibodyregistry' under entries: monoclonal mouse Anti-myc (RRID = AB_2556560), polyclonal goat anti-mouse IgG-HRP (RRID = AB_955440) and polyclonal rabbit Anti-GFP (RRID = AB_2749857). In addition, antibodies were validated by the use of an empty vector negative control (to control unspecific binding of antibodies to tobacco/agrobacterium proteins) and wild-type Sr35 (myc-tagged) or wild-type AvrSr35 (YFP-tagged) as positive controls on each western blot.

Eukaryotic cell lines

Policy information about cell lines

Cell line source(s)	Sf21 insect cell line (Invitrogen)
Authentication	none of the cell lines were authenticated
Mycoplasma contamination	cell line was not tested for mycoplasma contamination
Commonly misidentified lines (See ICLAC register)	no commonly misidentified cell lines were used in this study

Animals and other organisms

Policy information about studies involving animals; ARRIVE guidelines recommended for reporting animal research

Laboratory animals	Xenopus laevis, female, age 2-2.5 years
Wild animals	no wild animals were used in this study
Field-collected samples	no field collected samples were used in this study
Ethics oversight	The animal study (Xenopus laevis) was reviewed and approved by Laboratory Animal Ethics Committee at Institute of Genetics and Developmental Biology, Chinese Academy of Sciences, Beijing, China with the approval ID AP2020029.

Note that full information on the approval of the study protocol must also be provided in the manuscript.

Chapter 2: The barley MLA13-AVR$_{A13}$ heterodimer reveals principles for immunoreceptor recognition of RNase-like powdery mildew effectors

The barley MLA13-AVR$_{A13}$ heterodimer reveals principles for immunoreceptor recognition of RNase-like powdery mildew effectors

Aaron W. Lawson[1], Andrea Flores-Ibarra[2], Yu Cao[1,2,3], Chunpeng An[1], Ulla Neumann[4], Monika Gunkel[2], Isabel M. L. Saur[5,6], Jijie Chai[1,2,3], Elmar Behrmann[2], Paul Schulze-Lefert[1,6]

Corresponding authors: Jijie Chai, Elmar Behrmann, Paul Schulze-Lefert

Affiliations

[1]Department of Plant Microbe Interactions, Max Planck Institute for Plant Breeding Research, Cologne 50829, Germany
[2]Institute of Biochemistry, University of Cologne, Cologne 50674, Germany
[3]School of Life Sciences, Westlake University, Hangzhou 310031, China
[4]Central Microscopy, Max Planck Institute for Plant Breeding Research, Cologne 50829, Germany
[5]Institute for Plant Sciences, University of Cologne, Cologne 50674, Germany
[6]Cluster of Excellence on Plant Sciences (CEPLAS), Max Planck Institute for Plant Breeding Research and University of Cologne, Germany

Abstract

Co-evolution between cereals and pathogenic grass powdery mildew fungi is exemplified by sequence diversification of an allelic series of barley resistance genes encoding Mildew Locus A (MLA) nucleotide-binding leucine-rich repeat (NLR) immunoreceptors with a N-terminal coiled-coil domain (CNLs). Each immunoreceptor recognises a matching, strain-specific powdery mildew effector encoded by an avirulence gene (*AVR$_a$*). We present here the cryo-EM structure of barley MLA13 in complex with its cognate effector AVR$_{A13}$-1. The effector adopts an RNase-like fold when bound to MLA13 *in planta*, similar to crystal structures of other RNase-like AVR$_A$ effectors purified from *E. coli*. AVR$_{A13}$-1 interacts *via* its basal loops with MLA13 C-terminal leucine rich repeats (LRRs) and the central winged helix domain (WHD). Co-expression of structure-guided MLA13 and AVR$_{A13}$-1 substitution variants show that the receptor–effector interface plays an essential role in mediating immunity-associated plant cell death. Furthermore, by combining structural information from the MLA13–AVR$_{A13}$-1 heterocomplex with sequence alignments of other MLA receptors, we designed a single amino acid substitution in MLA7 that enables expanded effector detection of AVR$_{A13}$-1 and the virulent variant AVR$_{A13}$-V2. In contrast to the pentameric conformation of previously reported effector-activated CNL resistosomes, MLA13 was purified and resolved as a stable heterodimer from an *in planta* expression system. Our study suggests that the MLA13–AVR$_{A13}$-1 heterodimer might represent a CNL output distinct from CNL resistosomes and highlights opportunities for the development of designer gain-of-function NLRs.

Keywords: NLR receptors, pathogen effectors, co-evolution, plant immunity, powdery mildew, cell death

Introduction

Plant–pathogen co-evolution involves reciprocal, adaptive genetic changes in both organisms, often resulting in population-level variations in nucleotide-binding leucine-rich repeat (NLR) immune receptors of the host and virulence-promoting effectors of the pathogen[1]. NLRs often detect strain-specific pathogen effectors, so-called avirulence effectors (AVRs), inside plant cells, either by direct binding or indirectly by monitoring an effector-mediated modification of virulence targets[2]. There are two main classes of modular sensor NLRs in plants, defined by a distinct N-terminal coiled-coil domain (CC; CNLs) or a Toll-Interleukin-1 Receptor (TIR) domain, each of which plays a critical role in immune signalling after receptor activation[3, 4]. A subset of effector-activated sensor CNLs and TNLs engage additional 'helper NLRs' for immune signalling, some of which contain a HeLo-/RPW8-like domain or a CC at the N-terminus[5, 6]. Immune signals initiated by activated sensor CNLs, sensor TNLs and helper NLRs converge on a rapid increase in Ca^{2+} levels inside plant cells, often followed by host cell death, which is referred to as a hypersensitive response (HR)[3, 7]. In the two sensor CNLs *Arabidopsis thaliana* ZAR1 and wheat Sr35, effector-induced activation results in pentamerisation of heteromeric receptor complexes, called resistosomes, which is mainly mediated by oligomerisation of their central nucleotide-binding domains (NBDs)[8-10]. Recombinant ZAR1 and Sr35 resistosomes expressed in *Xenopus* oocytes exhibit non-selective cation channel activity, and the ZAR1 resistosome has additionally been shown to insert into planar lipid layers and display calcium-permeable cation-selective channel activity[9, 11]. Thus, currently known structures of effector-activated sensor CNLs indicate the assembly of multimeric CNL resistosomes that mediate Ca^{2+} influx in plant cells, ultimately leading to HR[3].

In the sister cereal species barley and wheat, numerous disease resistance genes have been identified that encode CNLs conferring strain-specific immunity against the pathogenic grass powdery mildew fungi *Blumeria hordei* (*Bh*) or *Blumeria tritici* (*Bt*). Co-evolution with these Ascomycete pathogens has resulted in allelic resistance specificities at some of these loci in host populations, with each resistance allele conferring immunity only to powdery mildew isolates expressing a cognate isolate-specific AVR effector[12-16]. The *Bh* avirulence effectors AVR_{A1}, AVR_{A6}, AVR_{A7}, AVR_{A9}, AVR_{A10}, AVR_{A13}, and AVR_{A22} have been characterised and are recognized by the matching MLA receptors, MLA1, MLA6, MLA7, MLA9, MLA10, MLA13 and MLA22, respectively[17-19]. Although these AVR_As are unrelated at the sequence level, with the exception of allelic AVR_{A10} and AVR_{A22}, structural predictions and the crystal structure of a *Bh* effector with unknown avirulence activity (CSEP0064) suggested that they share a common RNase-like scaffold with a greatly expanded and sequence-diversified effector family in the genomes of grass powdery mildew fungi, termed RNase-like associated with haustoria (RALPH) effectors[19-22]. The crystal structures of *Bh* AVR_{A6}, AVR_{A7}-1, AVR_{A10} and AVR_{A22} validated this hypothesis and revealed unexpected structural polymorphisms between them that are linked to a differentiation of RALPH effector subfamilies in powdery mildew genomes[23]. The crystal structure of the RALPH effector AvrPm2a from *Bt*, detected by wheat CNL Pm2a, was also determined and belongs to a RALPH subfamily with 34 members, which includes *Bh* AVR_{A13}, *Bh* CSEP0064 and *Bt* E-5843[16, 23]. For both barley MLA and wheat Pm2a, co-expression of matching receptor–avirulence pairs is necessary and sufficient to induce cell death in heterologous *Nicotiana benthamiana*[16-19]. Similar to several other sensor CNLs, including ZAR1 and Sr35, mutations in MLA's MHD motif of the central NBD result in constitutive receptor

signalling and effector-independent cell death (e.g., autoactive MLA10^{D502V} and MLA13^{D502V})[24-26]. While yeast two-hybrid experiments and split-luciferase complementation assays indicate direct receptor–effector interactions for several matching MLA–AVR$_A$ pairs, similar assays suggest that wheat Pm2a indirectly detects AvrPm2 through interaction with the wheat zinc finger protein *Ta*ZF[18, 19, 27]. The LRR of Pm2a mediates association with *Ta*ZF and recruits the receptor and AvrPm2a from the cytosol to the nucleus. However, the structural basis for how the MLA and Pm2 CNLs either directly or indirectly recognize RALPH effectors is lacking.

In this study, we used transient heterologous co-expression of barley MLA13 with its matching effector AVR$_{A13}$-1 in *N. benthamiana* leaves and affinity purification of heteromeric receptor complexes to confirm that the effector binds directly to the receptor. In contrast to the pentameric wheat Sr35 resistosome bound to AvrSr35 of *Puccinia graminis* f sp *tritici* (*Pgt*), we find that the MLA13–AVR$_{A13}$-1 heterocomplex is purified as a stable heterodimer and resolved using cryo-EM at a global resolution of 3.8 Å. Structural insights into the receptor–effector interface then served as a basis for structure-guided mutagenesis experiments. We co-expressed wild-type or mutant MLA13 and AVR$_{A13}$-1 in barley leaf protoplasts and heterologous *N. benthamiana* leaves to test the relevance of effector–receptor interactions revealed by the cryo-EM structure and their roles in immunity-associated cell death *in planta*. Combining structural data with an in-depth sequence alignment between MLA receptors led to identification of a single amino acid substitution in the MLA7 LRR that allows expanded RALPH effector detection. We suggest that the stable heterodimeric MLA13–AVR$_{A13}$-1 complex may represent an intermediate receptor–effector complex, and the equilibrium between this complex and pentameric CNL resistosomes might be differentially regulated among different sensor CNLs.

Results

The *in planta*-expressed MLA13-AVR$_{A13}$-1 heterocomplex is resolved as a heterodimer

We co-expressed N-terminal GST-tagged MLA13 with C-terminal twin-Strep-tagged AVR$_{A13}$-1 in leaves of *N. benthamiana via Agrobacterium*-mediated transformation to facilitate the formation of potential receptor–effector heterocomplexes *in planta*, followed by affinity purification for structural studies. We observed that the substitutions MLA13$^{K98E/K100E}$, located in the CC domain, abrogate effector-triggered receptor-mediated cell death but not when MLA13$^{K98E/K100E}$ was combined with the autoactive substitution D502V (MLA13$^{K98E/K100E/D502V}$); Extended Data Fig. 3). Autoactivity of MLA13$^{K98E/K100E/D502V}$ indicates that the MLA13$^{K98E/K100E}$ substitutions do not generally disrupt receptor-mediated signalling. The MLA13$^{K98E/K100E}$ variant allowed us to express and purify these proteins while avoiding any effect of *in planta* cell death on receptor accumulation. Analogous substitutions were introduced in the helper CNL *At*NRG1.1 which impair its cell death activity and reduces association with the plasma membrane whilst retaining oligomerisation capability[28].

Affinity purification *via* the twin-Strep-tag on AVR$_{A13}$-1 resulted in the enrichment of both AVR$_{A13}$-1 and MLA13 as demonstrated by SDS-PAGE analysis (Extended Data Fig. 1). A subsequent affinity purification *via* the GST tag on MLA13 resulted in the enrichment of MLA13 with concurrent co-purification of AVR$_{A13}$-1 (Extended Data Fig. 1), indicating that MLA13 and AVR$_{A13}$-1 formed a

heterocomplex. Further analysis of the sample by size exclusion chromatography (SEC) revealed that the heterocomplex elutes at a volume implying a molecule significantly smaller than a hypothetical multimeric MLA13 resistosome (Fig. 1a). In line with the SEC results, negative stain transmission electron microscopy (TEM) analysis revealed homogeneous particles with a diameter of approximately 10 nm, suggesting a 1:1 heterodimer of MLA13–AVR$_{A13}$-1 rather than multimeric resistosome assemblies (Fig. 1b). Notably, star-shaped particles characteristic of pentameric resistosome assemblies such as Sr35 were completely absent (Fig. 1b).

Previously, structures of the pentameric Sr35 resistosome were determined after co-expression of wheat Sr35 with the avirulence effector AvrSr35 of the rust fungus *Pgt* in insect cell cultures and purification of a ~875 kDa complex by SEC[9, 10]. Stable heterodimeric MLA13–AVR$_{A13}$-1 complex formation without detectable high-order receptor–effector complexes in *N. benthamiana* prompted us to test whether co-expression of Sr35$^{L11E/L15E}$ with AvrSr35 in *N. benthamiana*, followed by the same purification method used for the purification of the MLA13–AVR$_{A13}$-1 heterocomplex, leads to the formation of the Sr35 resistosome *in planta*. SEC analysis of the affinity-purified Sr35$^{L11E/L15E}$–AvrSr35 heterocomplex revealed an abundant high-order complex eluting with an estimated molecular weight of 875 kDa (Extended Data Fig. 4b). Further TEM characterisation of the corresponding SEC fraction confirmed a star-shaped complex that resembles the reported insect cell-derived pentameric Sr35 resistosome[9, 10] (Extended Data Fig. 4c). This demonstrates that the formation of the Sr35 resistosome is intrinsic to the co-expression of the two proteins, despite highly divergent expression systems in insect and plant cells. Similar results were obtained when Sr50$^{L11E/L15E}$, an *Mla* ortholog in wheat, was co-expressed with *Pgt* AvrSr50 in *N. benthamiana*, resulting in pentameric Sr50 resistosomes upon TEM analysis (Extended Data Fig. 5)[29]. The pentameric Sr50 resistosomes purified from *N. benthamiana* are similarly star-shaped to wheat Sr35 resistosomes (Extended Data Fig.5c). In further support of these findings, blue native polyacrylamide gel electrophoresis (BN-PAGE) analysis of *N. benthamiana* leaf protein extracts provided evidence for abundant Sr35$^{L11E/L15E}$ oligomerization when co-expressed with AvrSr35, whereas MLA13$^{L11E/L15E}$ receptor oligomerization was undetectable in the presence of AVR$_{A13}$-1 (Extended Data Fig. 6). However, oligomerization was detected when autoactive MLA13$^{L11E/L15E/D502V}$ was expressed in *N. benthamiana* (Extended Data Fig.6). Collectively, this suggests that the heterodimeric MLA13-AVR$_{A13}$-1 complex might represent an intermediate effector-activated CNL complex and that the equilibrium between heterodimeric and pentameric resistosomes may be differentially regulated among sensor CNLs. Finally, we conducted additional purification experiments to avoid potential non-native conformations, for example expression of MLA13 without an N-terminal GST tag, without substitutions in the CC domain, or equivalent mutations in the CC domains used for expressing and resolving the Sr35 and Sr50 resistosomes (Extended Data Fig.7). These experiments consistently resulted in the purification of low-order MLA13 complexes that elute from SEC at a molecular weight resembling that of the MLA13-AVR$_{A13}$-1 heterodimer (Extended Data Fig.7).

Cryo-EM reveals the architecture of the MLA13–AVR$_{A13}$-1 heterodimer

Three independent MLA13–AVR$_{A13}$-1 heterocomplex samples were prepared for cryo-EM analysis. During unsupervised 2D classification only a subset of identified particles yielded classes with features reminiscent of secondary structure elements.

These had structures agreeing best with a heterodimeric but not with a pentameric assembly. Further classifying this subset of particles in 3D revealed heterodimeric complexes comprising one MLA13 and one AVR_{A13}-1. Reconstruction of these particles yielded a final cryo-EM density map at a global resolution of 3.8 Å. Local resolution analysis revealed that the core region of the complex, and importantly the interface between the receptor and AVR_{A13}-1, is defined up to 3.0 Å resolution. More peripheral regions such as the CC, the NBD and the first and last blades of the LRR show resolutions above 5.5 Å, implying their flexibility in the purified state of the heterodimer (Extended Data Fig. 2). Apart from these three regions, the quality of our map after machine learning-assisted sharpening was of sufficient quality to build an almost complete atomic model of the MLA13–AVR_{A13}-1 heterocomplex.

The overall architecture of the MLA13–AVR_{A13}-1 heterodimer resembles a single effector-bound protomer of the pentameric Sr35 resistosome[9, 10]. While the resolution of the CC domain ($MLA13^{1-172}$) does not allow for fitting individual side-chains, it clearly shows that the four amino terminal alpha helices (α1 to α4A) form a bundle reminiscent of the ligand-bound, monomeric Arabidopsis ZAR1–RKS1–$PBL2^{UMP}$ complex (Fig. 2a)[30]. Helix α3 is in close contact with a section of the MLA13 LRR ($MLA1^{518-956}$) that comprises a cluster of arginine residues ($MLA13^{R935/R936/R559/R561/R583/R612/R657/R703}$). This interdomain interaction is believed to be a precursor to formation of the 'EDVID' motif-arginine cluster observed in the ZAR1 and Sr35 resistosomes following activation and CC rearrangement[9, 10]. The linker ($MLA13^{131-143}$) between helix α4A and the NBD ($MLA13^{173-328}$) lacks observable density, suggesting significant flexibility.

Similar to the CC domain, the quality of cryo-EM density for the majority of the NBD does not allow for fitting individual side-chains. In addition, the canonical nucleotide binding site that is sequence-conserved with ZAR1 and Sr35 clearly lacks density for an ATP or ADP, similar to the ZAR1–RKS1–$PBL2^{UMP}$ complex (PDB: 6J5V)[30]. This suggests that the complex might be in an intermediate state after effector binding-induced release of ADP but before ATP binding-induced oligomerisation. Overlay of the MLA13 NBD after AVR_{A13}-1 binding to the receptor with the NBD of an Alpha-fold3 model of the AVR_{A13}-1-bound MLA13 receptor shows conformational differences in NBD conformations between the prediction and experimental model (Fig. 2c). In addition, a motion-based deep generative model to investigate the flexibility remaining in the subpopulation of particles used for the 3D refinement implies that the NBD can sample a conformational space by rotating relative to the WHD ($MLA13^{410-517}$) (Fig. 2b). Interestingly, a similar hinge situated between the NBD and the WHD domain is observed when comparing the MLA13 NBD position to the NBD position in ZAR1 bound or unbound to the effector[30]. Despite its flexibility, the MLA13 NBD does not, however, sample positions overlapping with the ZAR1 NBD, and the consensus position is about 75 degrees rotated compared to the ZAR1 resistosome (Fig.2b). Despite the differences observed for the NBD, the remaining domains of MLA13, namely HD1 ($MLA13^{329-409}$), WHD, and LRR, adopt positions similar to those observed in the non-resistosome ZAR1 structures (PDBs: 6J5W and 6J5V)[30].

AVR_{A13}-1 adopts an RNase-like fold *in planta* and interacts both with the LRR and the WHD domain of MLA13

AVR_{A13}-1 adopts an RNase-like fold reminiscent of the crystal structures reported for *E. coli*-expressed AVR_{A6}, AVR_{A7}-1, AVR_{A10} and AVR_{A22} of *Bh*, all of which share a structural core of two β-sheets and a central α-helix (Fig. 3a)[23]. The N-terminal β-

sheet consists of two antiparallel strands (β1 and β2), whilst the second β-sheet consists of four antiparallel β-strands (β3 to β6). Based on structural polymorphisms between *Bh* AVR_{A6}, AVR_{A7}-1, AVR_{A10}, AVR_{A22} and *Bt* AvrPm2, AVR_{A13}-1 is most similar to *Bt* AVR_{Pm2} and the structure of a *Bh* effector with unknown avirulence activity, CSEP0064[21, 23]. Each of the four crystallised AVR_A effectors and *Bt* AvrPm2 share two conserved cysteine residues at the N and C termini, respectively, that form an intramolecular disulphide bridge connecting the N- and C-terminals. In AVR_{A13}-1, however, the position of the N-terminal cysteine is occupied by a leucine, preventing intramolecular disulphide formation with the C terminal residue AVR_{A13}-1^{C116} (Fig. 3a). The conserved structural core of AVR_{A13}-1 and proximity of AVR_{A13}-1 N- and C-terminal ends show that intramolecular disulphide bridge formation is likely dispensable for adoption of an RNase-like fold when bound to its receptor inside plant cells (Fig. 3a). This also indicates that binding to the receptor does not lead to extensive rearrangements of the RNase-like fold compared to AVR_A crystal structures of proteins purified from *E. coli* and unbound to their matching receptor[22].

The cryo-EM density with higher local resolution of the interface between the MLA13 LRR and AVR_{A13}-1 reveals interactions of the effector with multiple receptor residues, specifically from the concave side of the LRR and the WHD (Fig. 4a). To investigate the physiological relevance of the interactions between MLA13 and AVR_{A13}-1, we generated substitution variants of putative interacting residues in both the receptor and effector; we then transiently expressed these in barley protoplasts and leaves of *N. benthamiana* and tested for loss of AVR_{A13}-1-triggered and MLA13-mediated cell death.

Visualisation of the MLA13–AVR_{A13}-1 interface clarifies that the two basal loops of AVR_{A13}-1 (AVR_{A13}-$1^{W47\text{-}T74}$) play an essential role in the interaction with MLA13 and receptor-mediated cell death. Notably, the aromatic ring from AVR_{A13}-1^{Y52} presents strong π-π stacking with $MLA13^{F900}$ and interacts with $MLA13^{F934}$, an observation supported by a loss in cell death activity due to the single AVR_{A13}-1^{Y52A} and $MLA13^{F900A}$ substitutions (Figs. 3b,c and 4b,c). Contributing to stabilisation of the AVR_{A13}-1 basal loops and their interaction with the receptor, AVR_{A13}-1^{F65} seemingly engages in a T-shaped interaction with the aromatic ring of $MLA13^{Y934}$. Furthermore, a notable reduction of cell death was observed when stacking the two substitutions AVR_{A13}-$1^{Y52A/G60A}$, presumably generating a steric clash between the backbone of AVR_{A13}-1^{G60} and $MLA13^{Y491}$ (Fig. 3b,c and Fig. 4b,c). Reciprocally, the substitutions $MLA13^{Y491A}$ and $MLA13^{Y496A}$ in the WHD resulted in a reduced cell death, suggesting that the WHD plays a critical role in triggering conformational changes in MLA13 that are necessary for cell death activity (Fig. 4b,c). Additional charged π interactions between $MLA13^{H643}$ and AVR_{A13}-1^{N82} are also thought to be an important component of the receptor–effector interface. This is supported by the near-complete loss of cell death activity of the double substitution mutant $MLA13^{H643A/E936A}$ (Fig. 4b,c). We then tested the cell death activity of individual $MLA13^{E936A}$ and $MLA13^{S902A}$ variants (Fig. 4b,c). While $MLA13^{S902A}$ retained wild-type-like activity, the single receptor substitutions $MLA13^{F900A}$ and $MLA13^{E936A}$ resulted in a complete loss of cell death (Fig. 4b,c). Finally, we inferred that $MLA13^{S902}$ acts to stabilise $MLA13^{R938}$, an essential interactor of AVR_{A13}-1^{D50} and AVR_{A13}-1^{A51} that leads to a complete loss of cell death when introducing the single substitution $MLA13^{R938A}$ (Fig. 4b,c).

Expansion of MLA7 effector recognition specificity

Understanding the roles of receptor residues in the MLA13–AVR_{A13}-1 interface allowed us to generate a gain-of-function (GoF) MLA receptor based on amino acid sequence alignment with known MLA resistance specificities to *Bh* (Extended Data Fig. 8)[12]. In this alignment, we observed that MLA7 is most similar to MLA13 with over 93% sequence conservation among the two LRR domains (Extended Data Fig. 8)[23]. Closer inspection of the MLA7 and MLA13 sequence alignment revealed that only one of the LRR residues contributing to the MLA13–AVR_{A13}-1 interface was polymorphic between the two receptors at positions $MLA7^{L902}$ and the corresponding $MLA13^{S902}$ (Extended Data Fig.8). We then introduced the substitution $MLA7^{L902S}$ to test if this MLA13-mimicking receptor could gain detection of AVR_{A13}-1 while retaining the ability to detect its previously described cognate AVR_{A7} effectors[18]. The co-expression of MLA7 WT with AVR_{A7}-2 in barley protoplasts results in a cell death response, whilst only weakly recognising AVR_{A7}-1, AVR_{A13}-1 and AVR_{A13}-V2, a virulent variant of AVR_{A13}-1 (Fig. 5a)[17, 26]. We then performed the same experiment with the $MLA7^{L902S}$ variant: not only was cell death activity retained upon co-expression with AVR_{A7}-2, but a gain of cell death activity was detected upon co-expression with AVR_{A7}-1, AVR_{A13}-1 and AVR_{A13}-V2, a virulent variant of AVR_{A13}-1 (Fig. 5a). Notably, $MLA7^{L902S}$ does not detect AVR_{A22}, indicating that the detection GoF receptor could be limited to a subset of RALPH effectors (Fig. 5a). The same co-expression experiments were performed in leaves of *N. benthamiana* with qualitatively similar results (Fig. 5b,c,d).

Discussion

Resolving the structure of the MLA13–AVR_{A13}-1 heterodimer revealed a 'noncanonical' conformation compared to two known pentameric plant CNL resistosomes, *A. thaliana* ZAR1 and wheat Sr35[8-10]. Similar structures of monomeric ZAR1 are available (PDBs: 6J5W and 6J5V) and represent intermediate forms of the effector-activated pentameric ZAR1 resistosome[8, 30]. The ZAR1–RKS1 complex binds ADP, and subsequent $PBL2^{UMP}$ binding in the presence of ATP results in allosteric changes, allowing the exchange of ADP to ATP in the NBD and the formation of a fully activated ZAR1 resistosome[8, 30]. ZAR1–RKS1 binding of $PBL2^{UMP}$ in the absence of ATP results in a nucleotide-free, ligand-bound intermediate complex (PDB: 6J5V), a conformation reminiscent of the MLA13–AVR_{A13}-1 heterodimer.

In contrast to the Sr35 and Sr50 resistosomes, MLA13 oligomerisation *in planta* was only detectable when introducing an autoactive-inducing substitution ($MLA13^{D502V}$), which is thought to mimic ATP binding, resulting in effector-independent cell death (Extended Data Fig. 6). We expressed and purified a stable MLA13–AVR_{A13}-1 heterodimer using the same protocol successfully used to purify pentameric Sr35 and Sr50 resistosomes. This prompts the question: why does the co-expression of MLA13 and AVR_{A13}-1 not result in the purification of a higher-order complex (i.e., an MLA13 resistosome) from an *in planta* expression system (Extended Data Figs, 4,5,7)? We consider four possible explanations for this result. First, a high-order MLA13–AVR_{A13}-1 heterocomplex might be prone to disassociation and thus requires yet unknown extraction conditions to maintain resistosome conformation when isolated. Second, the conformational transition between effector-dependent, intermediate and oligomeric receptor states might be differentially regulated in MLA13, Sr35, Sr50 and ZAR1. Third, in heterologous *N. benthamiana*,

additional components for abundant MLA13 high-order complex formation might be present in insufficient concentrations for detectable resistosome formation. For instance, a number of MLA resistance specificities, including MLA13, require the barley co-chaperones RAR1 and SGT1 for full immunity to *Bh*[31-34] . These two proteins form a ternary HSP90–RAR1–SGT1 chaperone complex, which elevates pre-activation MLA steady-state levels in barley and might facilitate the formation of MLA13 resistosomes from the MLA13–AVR_{A13}-1 heterodimer. Finally, it is also possible that the stable MLA13–AVR_{A13}-1 heterodimer generates a CNL output that is distinct from CNL resistosomes. For example, it remains to be tested whether the heterodimeric complex described here contributes to nucleo-cytoplasmic partitioning of MLA receptors and their interference with the transcription machinery *via* associations with barley transcription factors[27, 35, 36].

Structure-guided amino acid substitutions of the receptor–effector interface demonstrate the importance of MLA13–AVR_{A13}-1 interactions for triggering effector-dependent and receptor-mediated plant cell death. This interface is primarily mediated by interactions supported by residues in the MLA13 WHD, LRR and two basal loops in AVR_{A13}-1. Similarly, earlier structure–function analyses of AVR_{A10}, AVR_{A22} and AVR_{A6} hybrid effectors suggested that multiple highly polymorphic effector surface residues in the basal loops of each of these *Bh* RALPH effectors are indispensable for recognition by their matching MLA receptors[19, 23]. This suggests the existence of a common structural principle by which functionally diversified MLA receptors recognise sequence-unrelated RALPH effectors *via* their polymorphic basal loops. This is consistent with the observation that the structural core of RALPH effectors with two β-sheets and a central α-helix of AVR_{A13}-1 does not directly contribute to binding MLA13. Interestingly, Alphafold3 generated several models in which AVR_{A13}-1 binds to the LRR domain of MLA13, but neither the binding site to the LRR nor the orientation of the effector relative to the LRR corresponds to the experimentally determined receptor–effector interface (Fig. 2d). Why would MLA receptors preferentially recognise AVR_A effectors at the basal loops and not at other distant surface regions of the RNase-like scaffold? We hypothesise that the polymorphic sequences in the basal loops are important for the virulence activity of these *Bh* RALPH effectors, perhaps allowing them to interact with different virulence targets. However, wheat CNL Pm2a is believed to detect the *Bt* RALPH effector AvrPm2 on the opposite effector side, termed the 'head epitope' which comprises the juxtaposed N- and C-termini[16]. This could be explained by the finding that Pm2a recognises AvrPm2 indirectly through interaction with the wheat zinc finger protein TaZF[23]. An alternative hypothesis is that MLAs avoid recognising conserved structural elements, such as those of RNase-like scaffolds, to prevent interacting with RNase-like host proteins that may trigger a non-pathogen-induced cell death.

Here we provide evidence that residues in the C-terminal region of the MLA13 LRR are essential for receptor-mediated cell death activation upon detection of its cognate effector AVR_{A13}-1. The broader relevance of the C-terminal LRR region among MLA receptors for the detection of different AVR_A effectors is supported by domain swap experiments between LRR regions of MLA1 and MLA6 and MLA10 and MLA22, respectively[19, 32]. Our results show that although the LRR region is the most polymorphic among characterized MLA receptors, there are relatively few polymorphic residues in the MLA13 LRR that are critical for recognition of AVR_{A13}-1[12]. This information, combined with knowledge of natural LRR sequence polymorphisms among MLA receptors with distinct AVR_A effector recognition specificities, has informed the design of a GoF MLA receptor with only a single-base

edit (MLA7^{L902S}). Importantly, in the context of MLA13, substitution of MLA13^{S902A} resulted in a retention of AVR$_{A13}$-1-triggered cell death activity, suggesting that MLA13^{S902} may not play a critical role in supporting the interface with AVR$_{a13}$-1. In the context of MLA7, the MLA7^{L902S} substitution is crucial for a gain of AVR$_{a13}$-1 detection, suggesting that the bulky MLA7^{L902} disrupts the stability of MLA7^{R938} and its essential role in effector interaction. Nevertheless, without experimental MLA7^{L902S} structures bound to AVR$_{A13}$-1 and AVR$_{A7}$-2, we cannot rule out the possibility that variation in the basal loop lengths of these two AVR$_{A}$ effectors might lead to conformationally different receptor–effector interfaces (Extended Data Figs. 9,10). In fact, the structural polymorphisms between the two RALPH subfamilies, which include AVR$_{A7}$-2 and AVR$_{A13}$-1, differ primarily in the lengths of the four antiparallel β-strands (β3 to β6) of the second β-sheet and not the number of structural elements, thereby resulting in different lengths of the basal loops[23]. Since the crystal structures of AVR$_{A6}$, AVR$_{A7}$-2, AVR$_{A10}$, and AVR$_{A22}$ represent unbound effector folds and a structure for unbound AVR$_{A13}$-1 is not available, it remains to be clarified whether the basal loops of AVR$_{A}$ effectors undergo conformational changes upon receptor binding and, if so, whether these are similar or vary among AVR$_{A}$ effectors (Extended Data Figs. 9,10).

Expanding effector detection specificity by minimal perturbations such as single-base gene editing is an attractive approach for accomplishing more durable disease resistance in crops. Characterized *Mla* resistance specificities to *Bh* are alleles of one of three highly sequence-diverged CNL homologs at the complex *Mla* locus[33, 37, 38]. This precludes the generation of lines expressing two or more homozygous *Mla* resistance specificities by crossings between accessions encoding naturally polymorphic *Mla*s. The expanded detection capability of MLA7^{L902S} is a promising and notable proof-of-principle, as the receptor is able to recognise multiple RALPH effectors belonging to two phylogenetic subfamilies. The new repertoire of matching effectors detected by MLA7^{L902S} is simultaneously expressed in several globally distributed *Bgh* strains and includes the virulent effector, AVR$_{A13}$-V2, which is presumed to be the result of resistance escape of MLA13 due to selection pressures[17, 18, 26]. Furthermore, certain allelic *Pm3* resistance specificities in wheat confer both strain-specific immunity to *Bt* and non-host resistance to other cereal mildews[14]. These wheat Pm3 CNL receptors recognise strain-specific matching *Bt* RALPH effectors and conserved RALPH effector homologues in rye mildew (*B. graminis* f sp *secale*), thereby restricting growth of rye mildew on wheat[14]. Given that barley MLA7^{L902S} also confers enhanced cell death activity to the naturally occurring virulent variant of AVR$_{A13}$-1, AVR$_{A13}$-V2, and that the 34 members of this RALPH subfamily include several *Bt* effectors, including AvrPm2 and *Bt* E-5843, it seems possible that this or other engineered MLA receptors could enhance barley non-host resistance to other cereal mildews[16, 17, 23]. Future work will complement our findings by generating gene edited barley lines expressing synthetic MLAs for resistance testing.

Methods

Plant growth

Seeds of wild-type *N. benthamiana* were sown in peat-based potting soil with granulated cork on the surface to prevent pest infestation. Daily irrigation solution contained an electrical conductivity of 2.2 and a mixture of macro and micro

nutrients. A photoperiod of 16 hours was used with broad-spectrum LED lights emitting 220 μmol/m^2/s supplemented by ambient sunlight.

Barley protoplasts isolated from Golden Promise seedlings that were grown on peat-based potting soil at 19 °C and 70% humidity for 7–9 days.

Transient transformation of *N. benthamiana* for recombinant protein expression and purification

The coding sequences of *Mla13* containing a stop codon was transferred from pDONR221 using Gateway LR clonase into pGWB424 containing an N-terminal fusion GST tag in the vector backbone. *AVR$_{a13}$-1* without a stop codon was transferred from pDONR221 using Gateway LR clonase into pGWB402SC containing a C-terminal Twin-Strep-tag® followed by a single HA tag in the vector backbone. Both constructs were individually electroporated into *Agrobacterium tumefaciens* strain GV3101::pMP90RK and selected on plates of Luria/Miller (LB) broth with agar containing spectinomycin (100 μg/mL), gentamycin (25 μg/mL), rifampicin (50 μg/mL) and kanamycin (25 μg/mL) and grown for two days at 28 °C. Three colonies were picked and cultured overnight in a 10-mL liquid LB starter culture with the above antibiotics at 28 °C. Two millilitres of the starter culture were added to and cultured in 350 mL of liquid LB broth containing the above antibiotics for 14 hours at 28 °C. The cultures were pelleted at 4,000 RCF for 15 minutes and resuspended in infiltration buffer (10 mM MES (pH 5.6), 10 mM $MgCl_2$, 500 μM acetosyringone) to an OD_{600} of 2 for each construct. The bacterial suspensions were combined at a 1:1 ratio and infiltrated into leaves of four-week-old *N. benthamiana* plants. The infiltrated plants were stored in the dark for 24 hours before they were returned to normal growth conditions where they grew for an additional 24 hours. The leaves were frozen in liquid nitrogen and stored at -80 °C until they were processed.

Protein purification for cryo-EM

One hundred grams of transiently transformed *N. benthamiana* leaf tissue were ground in a prefrozen mortar and pestle and gradually added to 200 mL of lysis buffer (buffer A; 50 mM Tris-HCl (pH 7.4), 150 mM NaCl, 5% glycerol, 10 mM DTT, 0.5% polysorbate 20, two vials of protease inhibitor cocktail (SERVA Electrophoresis GmbH catalogue # 39103.03), 5% BioLock (IBA Lifesciences GmbH catalogue # 2-02-5-250); pH adjusted to 7.4) until the lysate was defrosted and at 4 °C. The lysate was split into two 250 mL centrifuge bottles, centrifuged twice at 30,000 RCF for 15 minutes and filtered through double-layered miracloth after each centrifuge run.

Five hundred microlitres of Strep-Tactin XT Sepharose resin (Cytiva catalogue # 29401324) were equilibrated in wash buffer (buffer B; 50 mM Tris-HCl (pH 7.4), 150 mM NaCl, 2 mM DTT, 0.1% polysorbate 20; pH adjusted to 7.4). The resin was added to the lysate and incubated by end-over-end rotation at 4 °C for 30 minutes. The resin was washed three times with buffer B and finally isolated in a 1.5-mL tube. Five hundred microlitres of Strep-Tactin XT Sepharose resin elution buffer (buffer C; buffer B supplemented with 50 mM biotin; pH adjusted to 7.4) was added to the resin and rotated end-over-end for 30 minutes. The above elution step was repeated five times.

The five eluates were centrifuged at 16,000 RCF for one minute and 450 μL of supernatant were removed from each eluate and pooled. Two hundred microlitres of Glutathione Sepharose 4B resin (Cytiva catalogue # 17075601) was equilibrated in

buffer B and added to the Strep-Tactin XT eluate was combined with the Glutathione Sepharose 4B resin and incubated by mixing end-over-end for two hours at 4 °C. The Glutathione Sepharose 4B resin was washed twice before with buffer B. Elution from the Glutathione Sepharose 4B resin was performed by adding 200 μL of buffer D (buffer B supplemented with 50 mM reduced glutathione; pH adjusted to 7.4) and rotated end-over-end for 30 minutes. Elution was repeated for a total of four times. The four eluates were centrifuged at 16,000 RCF for one minute and 150 μL of supernatant were removed from each eluate. Twenty microlitres from the first eluate were used for cryo-EM grid preparation and the remaining eluate(s) were pooled and analysed by SEC.

For SEC, a Superose 6 increase 10/300 GL column (Cytiva catalogue #) was equilibrated with buffer B. Five hundred microlitres of the pooled GST eluate were loaded into the column and run at 0.3 mL/minute. Forty-five microlitres of the 500 μL fractions were loaded on SDS PAGE gels.

The Sr35 and Sr50 resistosomes were purified with the above method. The *in planta* cell death activity was abrogated for purification purposes through introduction of the L11E/L15E substitutions in the receptors. A single-step purification was performed by coimmunoprecipitating the effectors *via* the C-terminal and N-terminal twin-Strep epitope tags on AvrSr35 and AvrSr50, respectively. Sr35 and Sr50 were expressed without an epitope tag. The 5 mL of twin-Strep eluate was concentrated and analysed by SEC as described above.

Negative staining and TEM

Carbon film grids (Electron Microscopy Sciences catalogue # CF400-CU-50) were glow discharged for negative staining of protein samples. The MLA13-AVR$_{A13}$-1 heterodimer, Sr35 resistosome and Sr50 resistosome samples were series-diluted in buffer B. Six microlitres of sample were applied to the grid and incubated for one minute before blotting off excess sample with filter paper. Six microlitres of one percent uranyl acetate were then applied to the grids and incubated for one minute before blotting off with filter paper.

Grids were analysed using a Hitachi HT7800 TEM operating at 100 kV and fitted with an EMSIS XAROSA camera.

Cryo-EM sample preparation and data collection

Three microlitres of the purified MLA13–AVR$_{A13}$-1 sample were applied to an untreated graphene oxide-coated TEM grid (Science Services catalogue # ERGOQ200R24Cu50), incubated on the grid for 10 seconds, blotted for 5 seconds and flash-frozen in liquid ethane using a Vitrobot Mark IV device (Thermo Fisher Scientific) set to 90% humidity at 4 °C. Grids were stored under liquid nitrogen conditions until usage.

Cryo-EM data was acquired using a Titan Krios G3i (Thermo Fisher Scientific) electron microscope operated at 300 kV. Images were collected automatically using EPU (version 2.12) (Thermo Fisher Scientific) on a Falcon III direct electron detector with a calibrated pixel size of 0.862 Å*px^{-1}. Target defocus values were set to −2.0 to −0.3 μm. Data was acquired using a total dose of 42 e^{-}*Å^{-2} distributed among 42 frames, although the last three frames were excluded during data analysis.

Image processing and model building

Image processing was performed using CryoSPARC (version 4.1.1+patch 240110). Movie stacks were first corrected for drift and beam-induction motion, and then used

to determine defocus and other CTF-related values. Only high-quality micrographs with low drift metrics, low astigmatism, and good agreement between experimental and calculated CTFs were further processed. Putative particles were automatically picked based on an expected protein diameter between 8 and 12 nm, then extracted and subjected to reference-free 2D classification. 2D classes showing protein-like shapes were used for a template-based picking approach. Candidate particles were extracted again, subjected to reference-free 2D classification to exclude artefacts, and subsequent 3D classification to identify high-quality particles showing defined density for the effector, NBD, and LRR. This subset of particles was further refined using the non-uniform refinement strategy, yielding a map at a global resolution of 3.8 Å. DeepEMhancer was used to optimize the map for subsequent structure building. For further details see Extended Data Fig.2.

AlphaFold was used to predict a model for the CC-NBD-LRR domains of MLA13 from *H. vulgare* using the sequence Q8GSK4 from UniProt and two previously deposited structures in the PDBe, 5T1Y and 3QFL. The AlphaFold-predicted model was fitted into the map; however, the fold of the CC-domain did not match the observed density adjacent to the LRR. Afterward, Robetta was used to predict only this region, which gave outputs that more closely resembled the activated form of ZAR1 resistosome's CC-domain. Robetta uses deep learning-based methods, RoseTTAFold and TrRosetta algorithms, and thus it may be influenced by existing models of the sequence to be predicted. For this reason, the *ab initio* option was chosen when running a second round of predictions in Robetta, and a template of the inactive ZAR1 CC-domain from *A. thaliana* (6J5W, Wang et al 2019) was included in the subsequent prediction run. The new model of the CC-domain fitted the EM map significantly better than the previous predicted models; thus, it was merged with the rest of the MLA13 model for refinement. Finally, the model containing AVR_{A13}-1-bound MLA13 was refined against the EM map in iterations of *phenix.real_space_refine* and manual building in Coot. For further details and statistics see Supplementary Table 1. Molecular visualization and analysis were done using UCSF ChimeraX (version 1.7).

Cell death assays in barley protoplasts

Experiments were performed according to Saur *et al.* 2019 with the exception that plasmid DNA of all constructs was diluted to 500 ng/μL and transfection volumes were 15 μL, 10 μL, and 10 μL for *pUBQ:luciferase*, *Mla*, and AVR_a, respectively[39].

Cell death assays in leaves of *N. benthamiana*

DNA of effector and receptor sequences were cloned as mentioned above into pGWB402SC and pGWB517, respectively. Transformation and preparation of *A. tumefaciens* suspensions was performed as mentioned above. Phenotype images were taken 72 hours post infiltration while samples for western blot analysis were harvested 24 hours post infiltration.

Western blotting of samples consisted of flash-freezing 100 mg of each sample and pulverising the tissue using a bead beater. The frozen leaf powder was resuspended in the aforementioned buffer A. The samples were centrifuged twice at 16,000 RCF before adding 4× Lämmli buffer (Bio-Rad catalogue # 161-0737) supplemented with 5% mM β-mercaptoethanol and heating the sample to 95 °C for five minutes before cooling on ice. Ten microlitres of each sample were run on 12% SDS PAGE gels before transferring to a PVDF membrane. The membranes were then blocked in TBS-T containing 5% milk for one hour at room temperature (RT). Membranes were washed three times for five minutes in TBS-T then incubated with

anti-HA (Cell Signalling Technology catalogue # 3724; 1:1,000) and anti-MYC (Thermo Fisher Scientific Inc. catalogue # R950-25; 1:5,000) in TBS-T with 5% BSA for one hour at RT. Membranes were washed in TBS-T for 3 × 10 minutes incubating with secondary anti-rabbit (Cell Signalling Technology catalogue # 7074S; 1:2,000) and anti-mouse (Abcam Ltd. Catalogue # ab6728; 1:5,000) in TBS-T with 5% milk for one hour at RT. Membranes were washed in TBS-T for 3 × 15 minutes before developing using SuperSignal West Femto substrate (Thermo Fisher Scientific Inc. catalogue # 34096).

BN-PAGE assays

BN-PAGE assays were performed as described in Ma *et al.* (2024) with modifications[40]. Briefly, *N. benthamiana* leaf tissues expressing the indicated constructs were harvested at 48 h after infiltration. Two grams of each sample were ground into powder using liquid nitrogen and homogenized in 4-mL protein extraction buffer (10% glycerol, 50 mM Tris-HCl (pH 7.5), 150 mM NaCl, 5 mM DTT, 0.2% NP-40, 5 mM $MgCl_2$, 20 μM MG132, 1×Roche protease inhibitor cocktail). The extract was centrifuged twice at 4 °C, 12,000 RCF for 15 min. Then, 40 μL of extraction buffer-washed Strep-Tactin® Sepharose chromatography resin (Cytiva) were added to the extract and incubated with end-over-end rotation for one hour. The resins were collected by centrifugation at 1,000 RCF for 3 min and washed three times with wash buffer (10% glycerol, 50 mM Tris-HCl (pH 7.5), 50 mM NaCl, 2 mM DTT, 0.2% NP-40, 1×Roche protease inhibitor cocktail). Subsequently, 100 μL of elution buffer (wash buffer + 50 mM biotin) were added to the resin and followed by end-over-end rotation for 30 min. The purified protein samples were collected by centrifugation. Five microlitres of each sample (25 μL for MLA13 auto-active mutants) were mixed with Native PAGE G-250 additive to a final concentration of 0.1%, and placed on ice for 30 min. Protein samples and unstained Native Mark (Invitrogen catalogue #LC0725) were loaded and run on a Native PAGE 3%-12% Bis-Tris gel (Invitrogen catalogue #BN1001BOX) according to the manufacturer's instructions. The proteins were then immunoblotted as described above.

Data availability

The EM map has been deposited in the EMDB under the accession code EMD-50863. Atomic coordinates have been deposited in the Protein Data Bank under the accession code 9FYC. Other data used to generate tables and figures has been provided as source data with this publication.

Acknowledgements

We thank the greenhouse team at MPIPZ for their expertise in providing high-quality *N. benthamiana* plants. We thank Neysan Donnelly and Jane Parker for critical comments on an early version of this manuscript. We thank Arthur Macha, Petra Koechner, Sabine Haigis, Elke Logemann, Milena Malisic, Florian Kuemmel, Li Liu, Wen Song and Nitika Mukhi for their intellectual and experimental contributions. This work was funded by the Max-Planck-Gesellschaft (P.S.-L.), the Deutsche Forschungsgemeinschaft (DFG, German Research Foundation) in the Collaborative Research Centre Grant (SFB-1403 – 414786233 B08 to P.S.-L., I.M.L.S. and J.C.), Germany's Excellence Strategy CEPLAS (EXC-2048/1, project 390686111 to P.S.-L. and I.M.L.S.), the Ministry of Culture and Science of the State of North Rhine-

Westphalia (iHEAD to P.S.-L. and E.B.) and DFG Emmy Noether Programme (SA 4093/1-1 to I.M.L.S.). We acknowledge access to the cryo-EM infrastructure of StruBiTEM (Cologne, funded by DFG Grant INST 216/949-1 FUGG), and to the computing infrastructure of CHEOPS (Cologne, funded by DFG Grant INST 216/512/1 FUGG).

Author contributions

P.S.-L., J.C., E.B. and A.W.L. conceived the study; A.W.L., Y.C., C.A., M.G. and I.M.L.S. performed experiments; U.N. and M.G. performed electron microscopy screening; A.W.L., E.B., J.C. and P.S.-L. analysed data; A.F.-I. and E.B. performed structural model building; P.S.-L., E.B. and A.W.L. wrote the manuscript.

Competing interests

The authors declare no competing interests.

References

1. S. T. Chisholm, G. Coaker, B. Day and B. J. Staskawicz, Cell **124** (4), 803-814 (2006).
2. T. Maekawa, B. Kracher, S. Vernaldi, E. Ver Loren van Themaat and P. Schulze-Lefert, Proceedings of the National Academy of Sciences **109** (49), 20119-20123 (2012).
3. J. Chai, W. Song and J. E. Parker, Molecular Plant-Microbe Interactions® **36** (8), 468-475 (2023).
4. I. M. L. Saur, R. Panstruga and P. Schulze-Lefert, Nature Reviews Immunology **21** (5), 305-318 (2020).
5. S. M. Collier, L.-P. Hamel and P. Moffett, MPMI **24** (8), 918-931 (2011).
6. A. Bentham, H. Burdett, P. A. Anderson, S. J. Williams and B. Kobe, Annals of Botany (2016).
7. J. D. G. Jones, B. J. Staskawicz and J. L. Dangl, Cell **187** (9), 2095-2116 (2024).
8. J. Wang, M. Hu, J. Wang, J. Qi, Z. Han, G. Wang, Y. Qi, H.-W. Wang, J.-M. Zhou and J. Chai, Science **364** (6435) (2019).
9. A. Förderer, E. Li, A. W. Lawson, Y. N. Deng, Y. Sun, E. Logemann, X. Zhang, J. Wen, Z. Han, J. Chang, Y. Chen, P. Schulze-Lefert and J. Chai, Nature **610** (7932), 532-539 (2022).
10. Y. B. Zhao, M. X. Liu, T. T. Chen, X. Ma, Z. K. Li, Z. Zheng, S. R. Zheng, L. Chen, Y. Z. Li, L. R. Tang, Q. Chen, P. Wang and S. Ouyang, Sci Adv **8** (36), eabq5108 (2022).
11. G. Bi, M. Su, N. Li, Y. Liang, S. Dang, J. Xu, M. Hu, J. Wang, M. Zou, Y. Deng, Q. Li, S. Huang, J. Li, J. Chai, K. He, Y.-h. Chen and J.-M. Zhou, Cell **184** (13), 3528-3541.e3512 (2021).
12. S. Seeholzer, T. Tsuchimatsu, T. Jordan, S. Bieri, S. Pajonk, W. Yang, A. Jahoor, K. K. Shimizu, B. Keller and P. Schulze-Lefert, Mol Plant Microbe Interact **23** (4), 497-509 (2010).
13. S. Bourras, K. E. McNally, R. Ben-David, F. Parlange, S. Roffler, C. R. Praz, S. Oberhaensli, F. Menardo, D. Stirnweis, Z. Frenkel, L. K. Schaefer, S. Flückiger, G. Treier, G. Herren, A. B. Korol, T. Wicker and B. Keller, Plant Cell **27** (10), 2991-3012 (2015).
14. S. Bourras, L. Kunz, M. Xue, C. R. Praz, M. C. Müller, C. Kälin, M. Schläfli, P. Ackermann, S. Flückiger, F. Parlange, F. Menardo, L. K. Schaefer, R. Ben-David, S. Roffler, S. Oberhaensli, V. Widrig, S. Lindner, J. Isaksson, T. Wicker, D. Yu and B. Keller, Nature Communications **10** (1), 2292 (2019).

15. C. R. Praz, S. Bourras, F. Zeng, J. Sánchez-Martín, F. Menardo, M. Xue, L. Yang, S. Roffler, R. Böni, G. Herren, K. E. McNally, R. Ben-David, F. Parlange, S. Oberhaensli, S. Flückiger, L. K. Schäfer, T. Wicker, D. Yu and B. Keller, New Phytol **213** (3), 1301-1314 (2017).
16. B. Manser, T. Koller, C. R. Praz, A. C. Roulin, H. Zbinden, S. Arora, B. Steuernagel, B. B. H. Wulff, B. Keller and J. Sánchez-Martín, Plant J **106** (4), 993-1007 (2021).
17. X. Lu, B. Kracher, I. M. L. Saur, S. Bauer, S. R. Ellwood, R. Wise, T. Yaeno, T. Maekawa and P. Schulze-Lefert, Proceedings of the National Academy of Sciences **113** (42) (2016).
18. I. M. L. Saur, S. Bauer, B. Kracher, X. Lu, L. Franzeskakis, M. C. Müller, B. Sabelleck, F. Kümmel, R. Panstruga, T. Maekawa and P. Schulze-Lefert, eLife **8** (2019).
19. S. Bauer, D. Yu, A. W. Lawson, I. M. L. Saur, L. Frantzeskakis, B. Kracher, E. Logemann, J. Chai, T. Maekawa and P. Schulze-Lefert, PLOS Pathogens **17** (2) (2021).
20. C. Pedersen, E. Ver Loren van Themaat, L. J. McGuffin, J. C. Abbott, T. A. Burgis, G. Barton, L. V. Bindschedler, X. Lu, T. Maekawa, R. Wessling, R. Cramer, H. Thordal-Christensen, R. Panstruga and P. D. Spanu, BMC Genomics **13**, 694 (2012).
21. H. G. Pennington, R. Jones, S. Kwon, G. Bonciani, H. Thieron, T. Chandler, P. Luong, S. N. Morgan, M. Przydacz, T. Bozkurt, S. Bowden, M. Craze, E. J. Wallington, J. Garnett, M. Kwaaitaal, R. Panstruga, E. Cota and P. D. Spanu, PLOS Pathogens **15** (3), e1007620 (2019).
22. K. Seong and K. V. Krasileva, Nat Microbiol **8** (1), 174-187 (2023).
23. Y. Cao, F. Kümmel, E. Logemann, J. M. Gebauer, A. W. Lawson, D. Yu, M. Uthoff, B. Keller, J. Jirschitzka, U. Baumann, K. Tsuda, J. Chai and P. Schulze-Lefert, Proceedings of the National Academy of Sciences **120** (2023).
24. S. Bai, J. Liu, C. Chang, L. Zhang, T. Maekawa, Q. Wang, W. Xiao, Y. Liu, J. Chai, F. L. Takken, P. Schulze-Lefert and Q. H. Shen, PLoS Pathog **8** (6), e1002752 (2012).
25. T. Maekawa, W. Cheng, L. N. Spiridon, A. Töller, E. Lukasik, Y. Saijo, P. Liu, Q. H. Shen, M. A. Micluta, I. E. Somssich, F. L. W. Takken, A. J. Petrescu, J. Chai and P. Schulze-Lefert, Cell Host Microbe **9** (3), 187-199 (2011).
26. E. E. Crean, M. Bilstein-Schloemer, T. Maekawa, P. Schulze-Lefert, I. M. L. Saur and W.-M. Wang, Journal of Experimental Botany **74** (18), 5854-5869 (2023).
27. B. Manser, H. Zbinden, G. Herren, J. Steger, J. Isaksson, S. Bräunlich, T. Wicker and B. Keller, Plant Commun **5** (5), 100769 (2024).
28. Z. Wang, X. Liu, J. Yu, S. Yin, W. Cai, N. H. Kim, F. El Kasmi, J. L. Dangl and L. Wan, Proceedings of the National Academy of Sciences **120** (32) (2023).
29. J. Chen, N. M. Upadhyaya, D. Ortiz, J. Sperschneider, F. Li, C. Bouton, S. Breen, C. Dong, B. Xu, X. Zhang, R. Mago, K. Newell, X. Xia, M. Bernoux, J. M. Taylor, B. Steffenson, Y. Jin, P. Zhang, K. Kanyuka, M. Figueroa, J. G. Ellis, R. F. Park and P. N. Dodds, Science **358** (6370), 1607-1610 (2017).
30. J. Wang, J. Wang, M. Hu, S. Wu, J. Qi, G. Wang, Z. Han, Y. Qi, N. Gao, H.-W. Wang, J.-M. Zhou and J. Chai, Science **364** (6435) (2019).
31. S. Bieri, S. Mauch, Q.-H. Shen, J. Peart, A. Devoto, C. Casais, F. Ceron, S. Schulze, H.-H. Steinbiß, K. Shirasu and P. Schulze-Lefert, The Plant Cell **16** (12), 3480-3495 (2004).
32. Q.-H. Shen, F. Zhou, S. Bieri, T. Haizel, K. Shirasu and P. Schulze-Lefert, The Plant Cell **15** (3), 732-744 (2003).
33. D. A. Halterman and R. P. Wise, The Plant Journal **38** (2), 215-226 (2004).
34. A. V. E. Chapman, M. Hunt, P. Surana, V. Velásquez-Zapata, W. Xu, G. Fuerst and R. P. Wise, Genetics **217** (2) (2020).
35. Q. H. Shen, Y. Saijo, S. Mauch, C. Biskup, S. Bieri, B. Keller, H. Seki, B. Ulker, I. E. Somssich and P. Schulze-Lefert, Science **315** (5815), 1098-1103 (2007).

36. C. Chang, D. Yu, J. Jiao, S. Jing, P. Schulze-Lefert and Q. H. Shen, Plant Cell **25** (3), 1158-1173 (2013).
37. F. Wei, R. A. Wing and R. P. Wise, Plant Cell **14** (8), 1903-1917 (2002).
38. T. Maekawa, B. Kracher, I. M. L. Saur, M. Yoshikawa-Maekawa, R. Kellner, A. Pankin, M. von Korff and P. Schulze-Lefert, Mol Plant Microbe Interact **32** (1), 107-119 (2019).
39. I. M. L. Saur, S. Bauer, X. Lu and P. Schulze-Lefert, Plant Methods **15** (1) (2019).
40. S. Ma, C. An, A. W. Lawson, Y. Cao, Y. Sun, E. Y. J. Tan, J. Pan, J. Jirschitzka, F. Kümmel, N. Mukhi, Z. Han, S. Feng, B. Wu, P. Schulze-Lefert and J. Chai, Nature (2024).

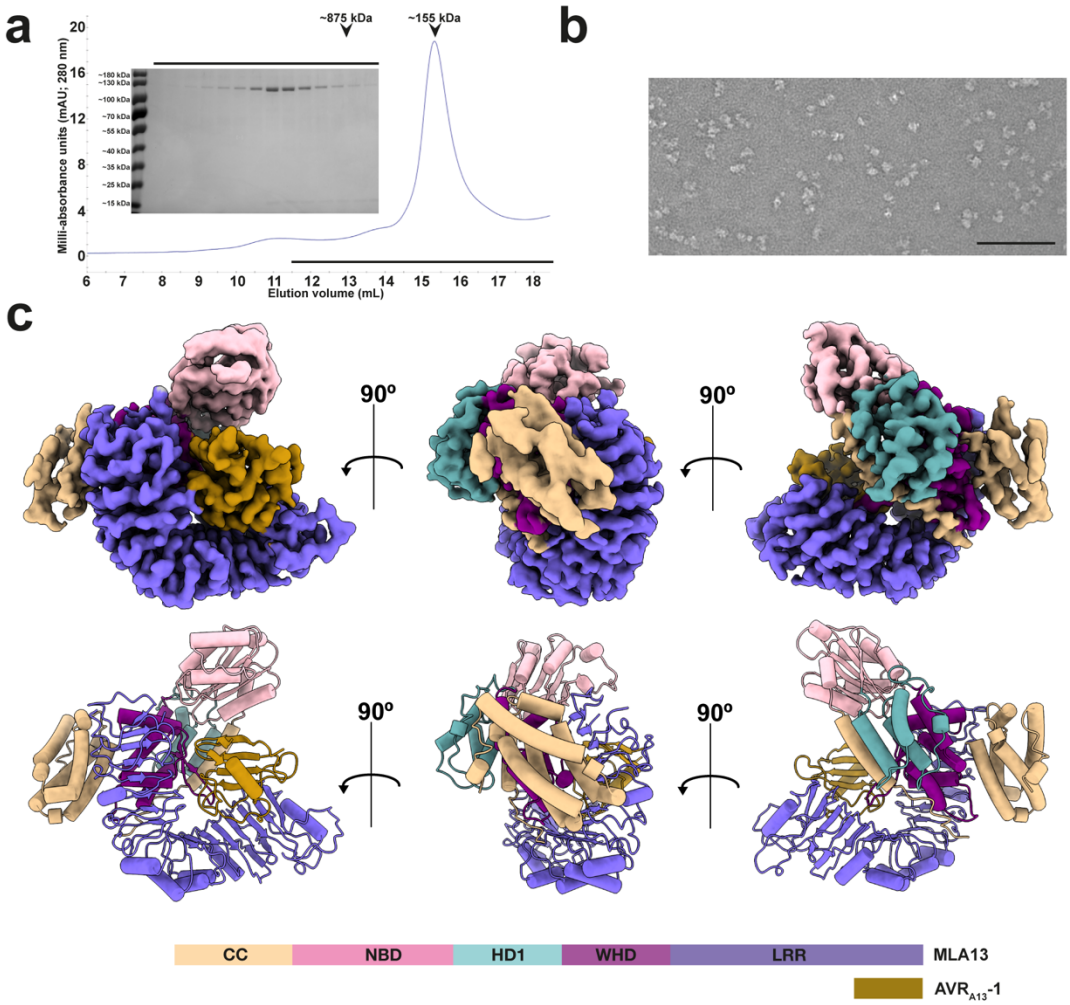

Fig. 1 | The MLA13-AVR$_{A13}$-1 complex is purified and resolved as a heterodimer. a, SEC profile of the N-terminally, GST-tagged MLA13 in complex with C-terminally, twin Strep-HA-tagged AVR$_{A13}$-1 sample purified by a two-step affinity purification as described in the Methods (Extended Data Fig.1). Inset SDS PAGE gel represents fractions eluted along the black line. The high-molecular weight marker (~875 kDa) was determined by running the Sr35 resistosome under the same conditions. **b,** Representative negative staining image of the peak elution volume diluted five-fold. Scale bar represents 100 nm **c,** Three orientations of the MLA13-AVR$_{A13}$-1 density map (above), atomic model (middle) and domain architecture (below). Workflow of cryo-EM data processing is presented as Extended Data Fig.2.

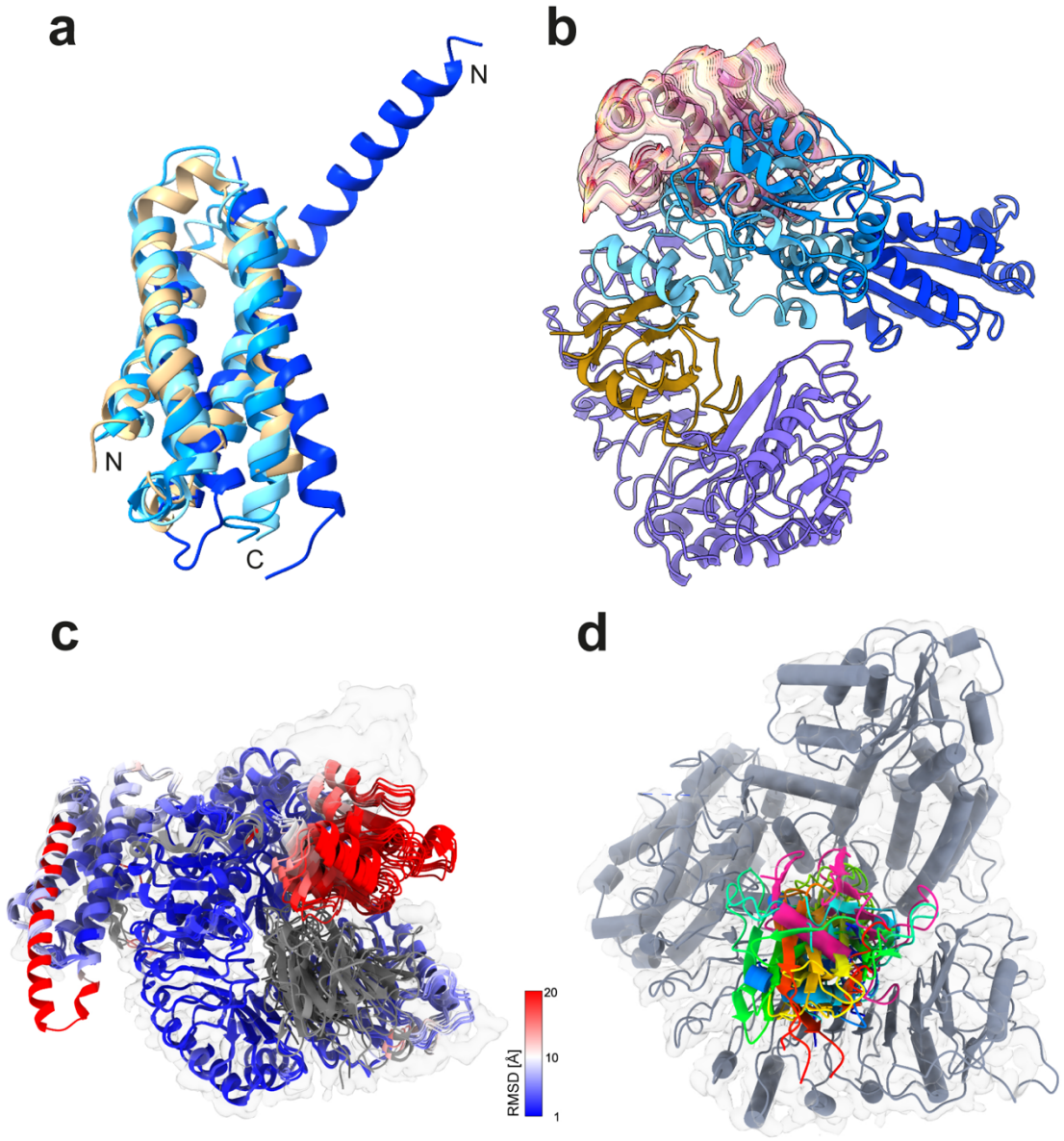

Fig. 2 | Conformational comparisons of the MLA13-AVR$_{A13}$-1 heterodimer with ZAR1 and Alphafold predictions. a, Structural alignment of the CC domains of ZAR1-RKS1 (light blue; PDB: 6J5W), ZAR1-RKS1-PBL2^{UMP} (blue; PDB: 6J5V) and ZAR1 resistosome (dark blue; PDB: 6J5T) to the CC domain of the MLA13-AVR$_{A13}$-1 heterodimer (beige). **b,** Structural alignment of ZAR1-RKS1 (light blue; PDB: 6J5W), ZAR1-RKS1-PBL2^{UMP} (blue; PDB: 6J5V) and ZAR1 resistosome (dark blue; PDB: 6J5T) to the MLA13-AVR$_{A13}$-1 heterodimer. Only the MLA13 NBD and LRR, AVR$_{A13}$-1 and NBDs of ZAR1 are shown. The red-yellow-red traces illustrate the major mode of conformational heterogeneity observed for the MLA13 NBD (average position shown in pink). **c,** Top five models for the MLA13-AVR$_{A13}$-1 complex as predicted by AlphaFold 3. All five models were aligned to the MLA13-AVR$_{A13}$-1 experimental atomic model (grey) and predicted models are coloured by their RMSD deviation to the experimental model. For all models, the position of the NBD does not align with the experimental model. The fourth helix of the CC bundle of one predictive model is too far elongated compared to the experimental model. The experimentally observed electron density map is shown in transparent grey. **d,** AlphaFold 3 predicts five different orientations of AVR$_{A13}$-1 (coloured rainbow) that are all incorrectly rotated compared to the experimentally observed position (pink). The MLA13-AVR$_{A13}$-1 experimental electron density map and model are shown in transparent grey and grey, respectively.

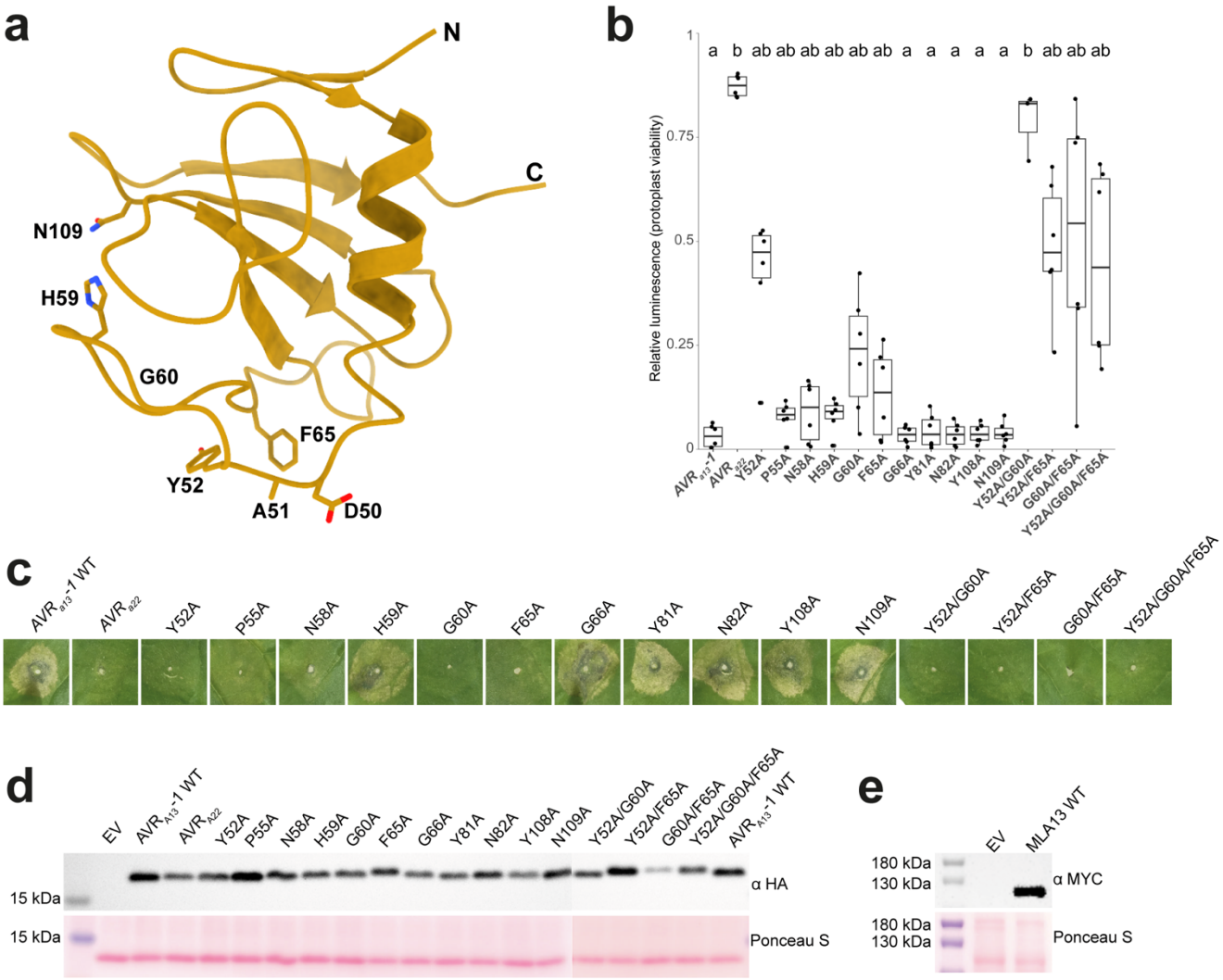

Fig. 3 | The AVR$_{A13}$-1 basal loops are primarily responsible for interacting with the MLA13 LRR. a, The cryo-EM structure of AVR$_{A13}$-1 residues (atom display) that were experimentally shown to be responsible for triggering MLA13-mediated cell death. **b,** Co-expression of MLA13 with AVR$_{A13}$-1 substitution mutants in barley protoplasts. Luminescence is normalised to EV + MLA13 (= 1). High relative luminescence suggests low cell death response and therefore suggesting loss of AVR$_{A13}$-1 interaction with MLA13. The six data points represent two technical replicates performed with three independently prepared protoplast samples. Treatments labelled with different letters differ significantly ($p < 0.05$) according to the Dunn's test. **c,** *Agrobacterium*-mediated co-expression of MLA13 with AVR$_{A13}$-1 interface substitution mutants in leaves of *N. benthamiana*. Three independent replicates were performed with two *Agrobacterium* transformations and plant batches (Supplementary Fig. 2). **d,** Western blot analysis of AVR$_{A13}$-1 substitution mutants. **e,** Western blot analysis of MLA13.

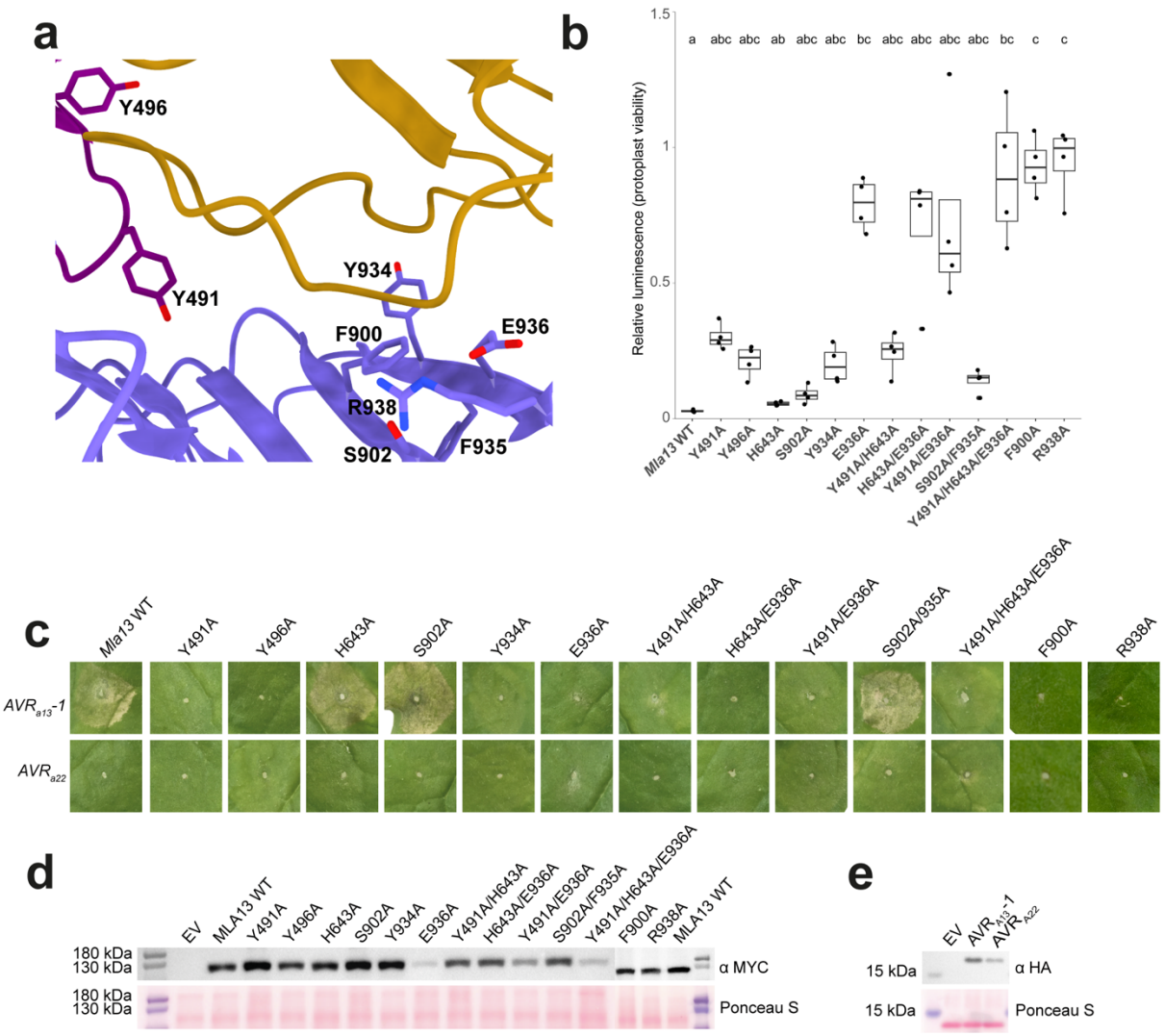

Fig. 4 | Minimal but spatially distributed recognition of AVR_{A13}-1 by the MLA13 LRR and WHD. a, The MLA13-AVR_{A13}-1 interface exhibiting MLA13 residues that were experimentally shown to contribute to AVR_{A13}-1-mediated cell death. **b,** Co-expression of AVR_{A13}-1 with MLA13 substitution mutants in barley protoplasts. Each MLA13 variant was normalised to its own autoactivity; luminescence is normalised to EV + MLA13 variant (= 1). High relative luminescence suggests low cell death response and therefore loss of AVR_{A13}-1 interaction with MLA13. The four data points represent two technical replicates performed with two independently prepared protoplast samples. Treatments labelled with different letters differ significantly ($p < 0.05$) according to the Dunn's test. **c,** *Agrobacterium*-mediated co-expression of AVR_{A13}-1 with MLA13 substitution mutants believed to contribute to MLA13 interface and cell death response in leaves of *N. benthamiana*. Three independent replicates were performed with two *Agrobacterium* transformations and plant batches (Supplementary Fig. 3). **d,** Western blot analysis of MLA13 substitution mutants. **e,** Western blot analysis of AVR_{A13}-1 and AVR_{A22}.

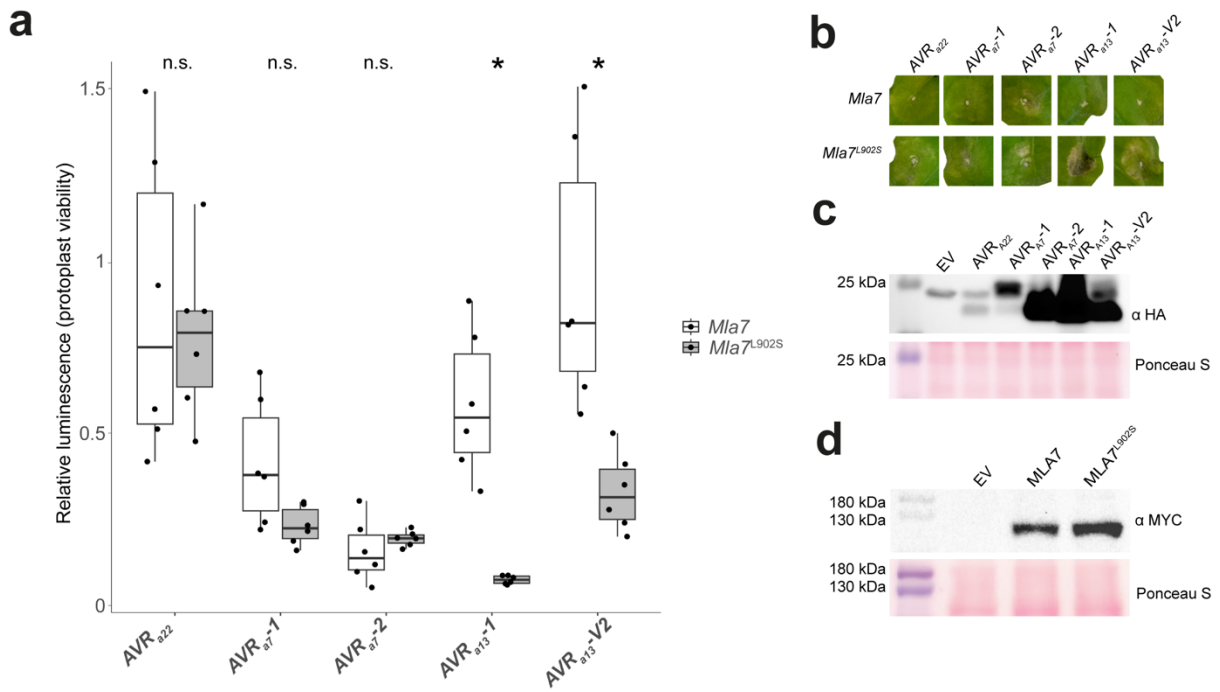

Fig. 5 | The MLA7^{L902S} substitution mutant results in expanded effector recognition. a, Co-expression of MLA7 and MLA7^{L902S} with AVR$_{A7}$ and AVR$_{A13}$ variants in barley protoplasts. Luminescence is normalised to EV + MLA7 (= 1) or EV + MLA7^{L902S} (= 1). High relative luminescence suggests low cell death response and therefore suggests low effector interaction with the receptor. The six data points represent two technical replicates performed with three independently prepared protoplast samples. Treatments labelled with an asterisk differ significantly (p <0.05) according to the Welch two-sample t-test. **b,** *Agrobacterium*-mediated co-expression of MLA7 and MLA7^{L902S} with AVR$_{A7}$ and AVR$_{A13}$ variants in *N. benthamiana* leaves. Three independent replicates were performed (Supplementary Fig. 4). **c,** Western blot analysis of the effector variants tested in (**b**). **d,** Western blot analysis of MLA7 and MLA7^{L902S}.

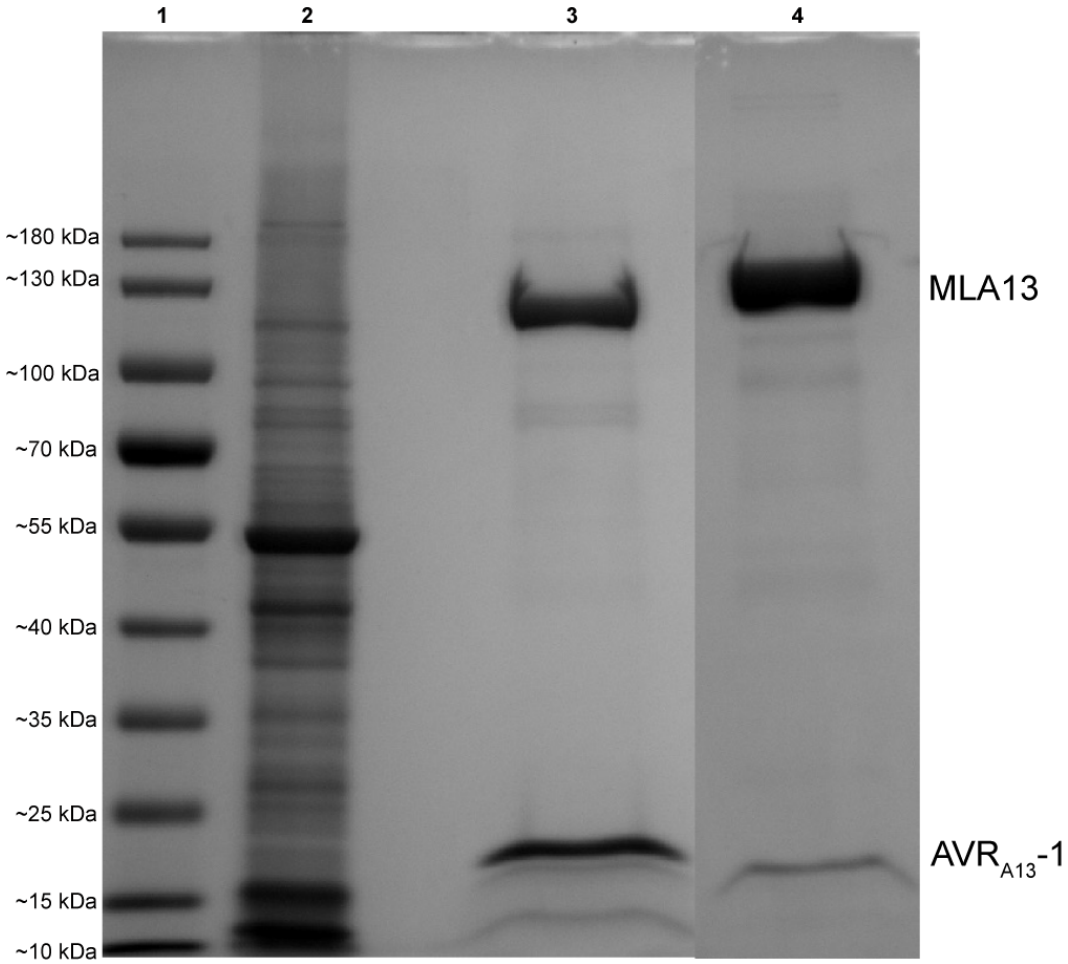

Extended Data Fig. 1 | CBB-stained SDS PAGE gel containing the samples from a two-step affinity purification of the MLA13-AVR$_{A13}$-1 heterodimer. Lane #1: ladder; lane #2: lysate (5 μL loaded); lane #3: first-step Twin-Strep elution (45 μL/1 mL loaded); lane #4: second-step GST elution (45 μL/750 μL loaded).

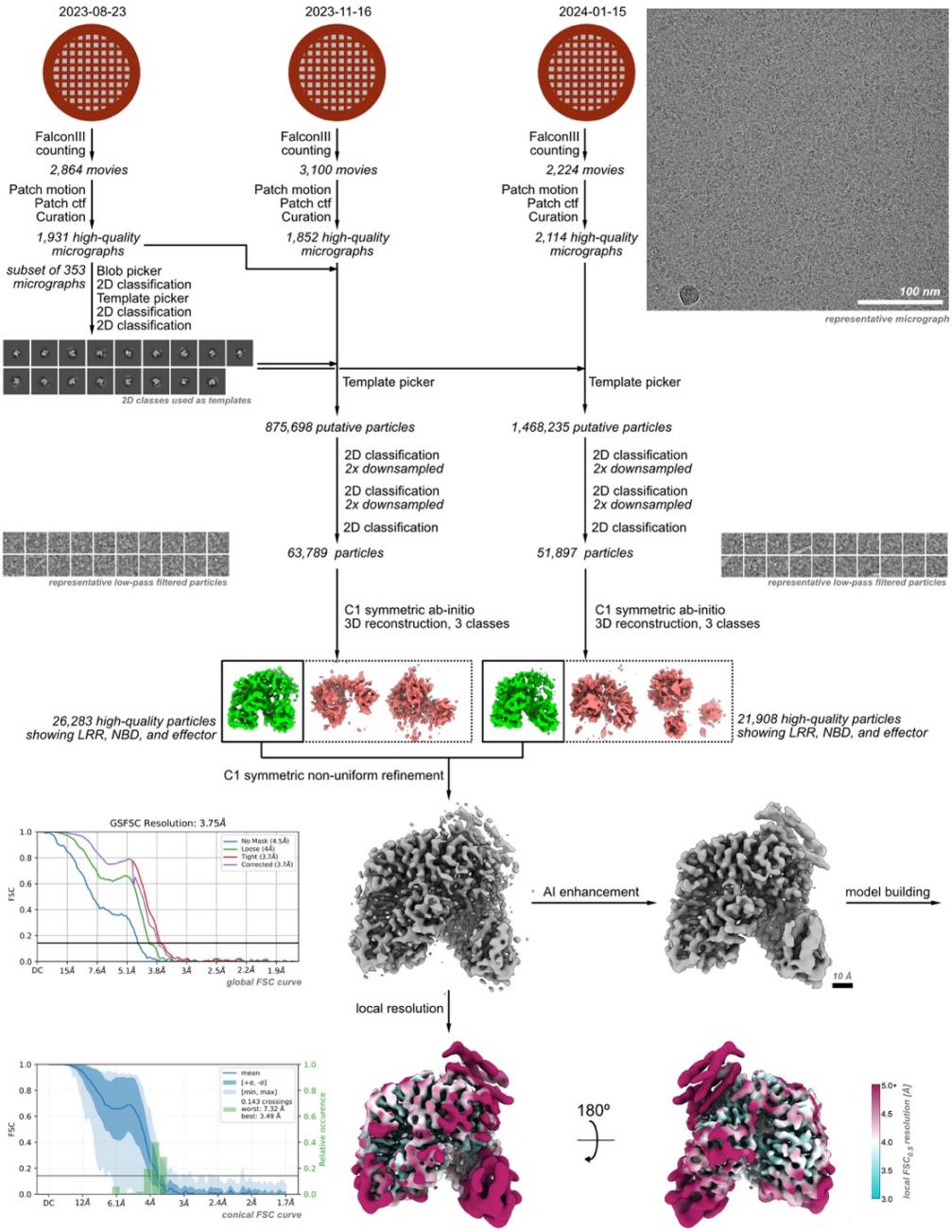

Extended Data Fig. 2 | Workflow of cryo-EM data acquisition and analysis of the MLA13-AVR$_{A13}$-1 heterodimer. A total of three datasets were collected on a 300 kV cryo-electron microscope. For each dataset, movies were selected for low per-frame drift rates, good CTF scores, and low astigmatism. Particles were first picked using a blob picker, and then subjected to unsupervised 2D classification. Representative classes showing protein-like structures were used for a template picker. Putative detected particles were curated using unsupervised 2D classification, selecting for particles with protein-like density and resolutions better than 10 Å. The selected particles were further curated using *ab initio* reconstruction, sorting them into three distinct populations. From these, all particles contributing to a structure showing clear density for the LRR, NBD and effector (shown in green and highlighted by a thicker box outline) were combined and refined in 3D using a non-uniform refinement algorithm, resulting in a map with a uniform resolution of 2.8 Å. Before model building, the map was further sharpened using DeepEMhancer. For further details, see the Materials and Methods and Supplementary Table 1.

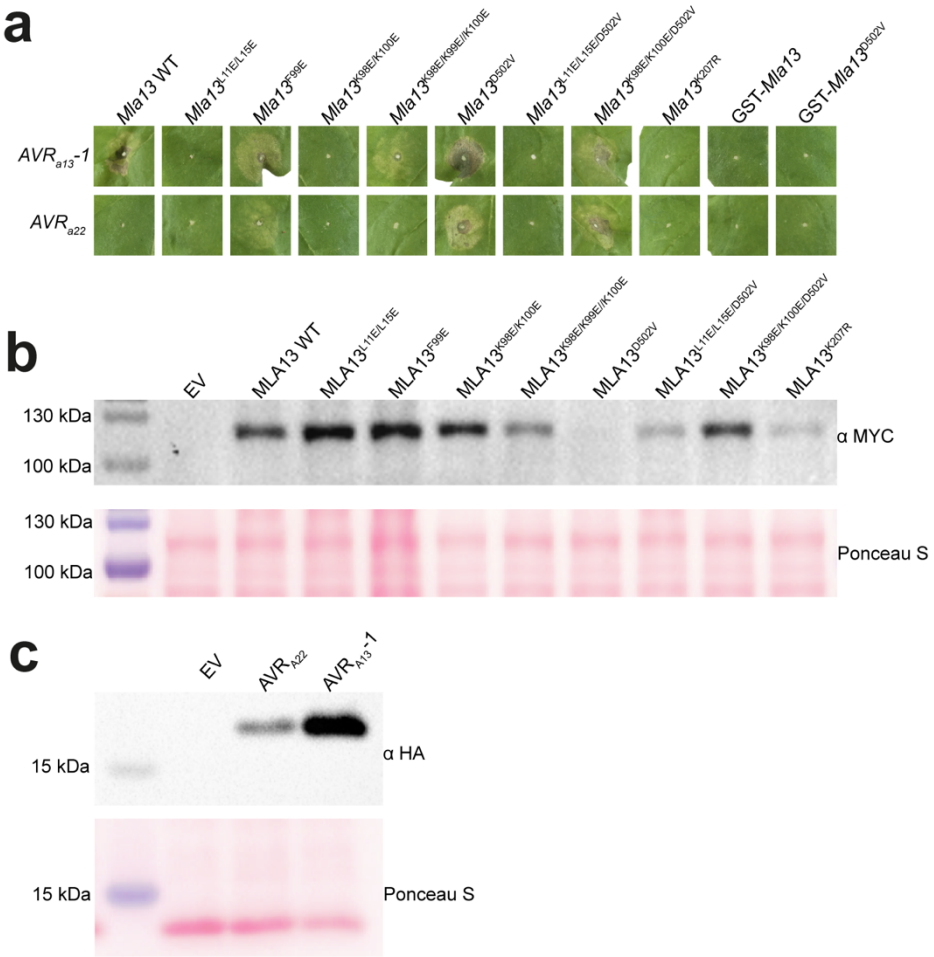

Extended Data Fig. 3 | *Agrobacterium*-mediated co-expression of MLA13 variants with AVR_{A13}-1 and AVR_{A22} in leaves of *N. benthamiana*. a, Cell death phenotypes of MLA13 phenotypes of variants that result in effector-triggered HR, autoactive HR or loss of HR. Six independent replicates were performed (Supplementary Fig.1). **b,** Western blot analysis of the above MLA13 variants. **c,** Western blot analysis of AVR_{A13}-1 and AVR_{A22}.

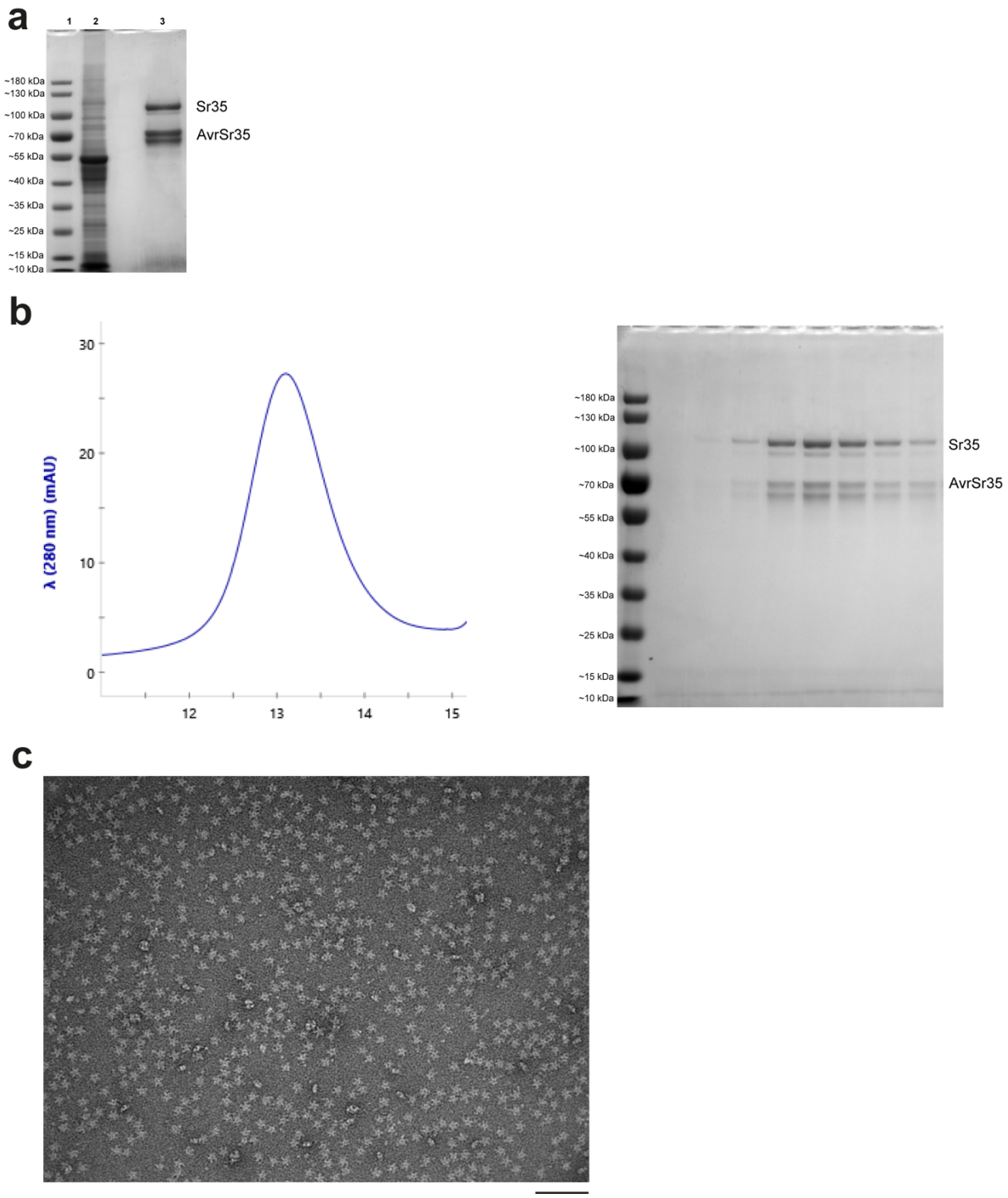

Extended Data Fig. 4 | Transient expression and purification of the Sr35 resistosome from leaves of *N. benthamiana*. a, CBB-stained SDS PAGE gel of a single step affinity purification of the Sr35 resistosome *via* the Twin-Strep tag at the C-terminal of AvrSr35 (Lane #1: ladder; lane #2: lysate (5 μL loaded); lane #3: first-step elution (45 μL/1 mL loaded). **b,** SEC profile (left) and SDS PAGE of resulting elution fractions. **c,** Negative staining of a five-fold dilution from the fraction corresponding to the 13 mL elution volume in (**b**). Black scale bar at the bottom right represents 100 nm.

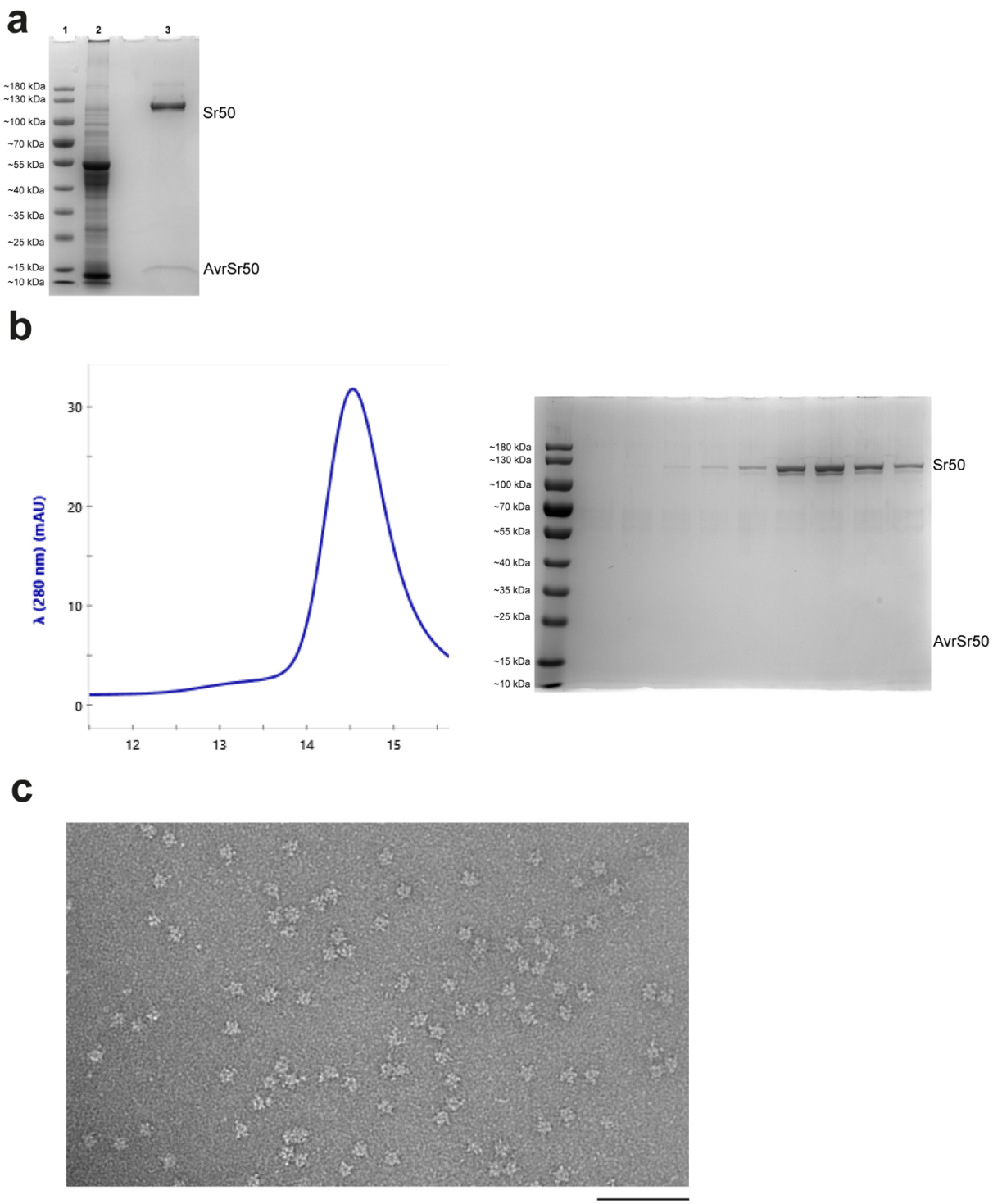

Extended Data Fig. 5 | Transient expression and purification of the Sr50 resistosome from leaves of *N. benthamiana*. a, CBB-stained SDS PAGE gel of a single step affinity purification of the Sr50 resistosome *via* the Twin-Strep tag at the N-terminal of AvrSr50 (Lane #1: ladder; lane #2: lysate (5 μL loaded); lane #3: first-step elution (45 μL/1 mL loaded). **b,** SEC profile (left) and SDS PAGE of resulting elution fractions. **c,** Negative staining of a 5× dilution from the fraction corresponding to the 14.5 mL elution volume in (**b**). Black scale bar at the bottom right represents 100 nm.

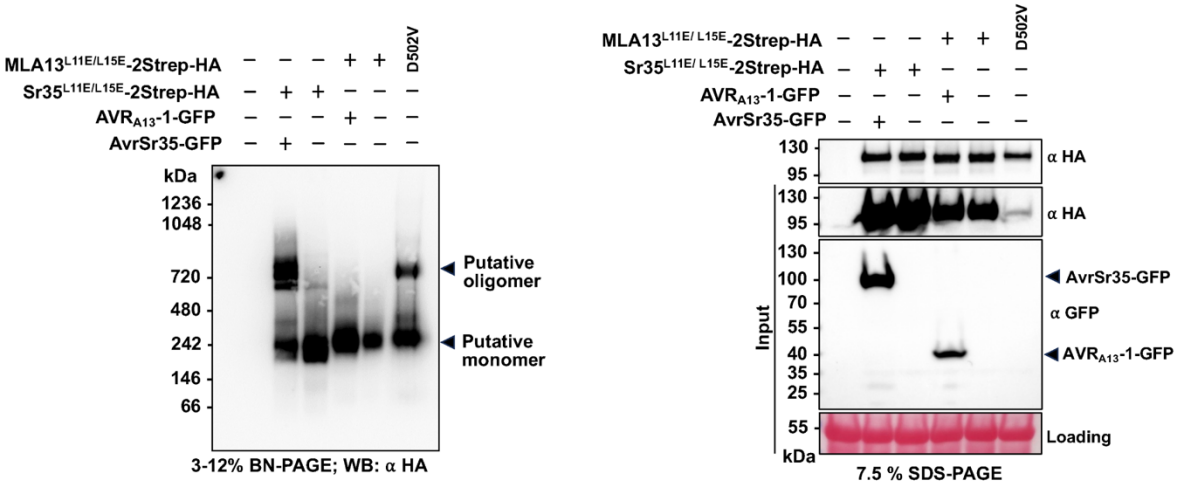

Extended Data Fig. 6 | Blue native-PAGE analysis of MLA13 oligomeric status. C terminal twin Strep-HA-tagged MLA13$^{L11E/L15E}$ or Sr35$^{L11E/L15E}$ were co-expressed with or without C terminally-GFP-tagged matching effectors in *N. benthamiana* leaves. The substitutions in MLA13$^{L11E/L15E}$ and Sr35$^{L11E/L15E}$ were introduced to prevent cell death. Purified protein samples *via* the twin Strep tag were analysed by blue native-PAGE (left panel) with subsequent western blotting. Deduced low-molecular weight receptor complexes, receptor monomers and oligomers are indicated by arrows. SDS-PAGE analysis of the input samples (right panel) was conducted to validate the expression of input proteins. Due to low abundance of MLA13$^{L11E/L15E/D520V}$, we loaded five times the volume of this sample on the blue native-PAGE gel. Ponceau S staining of RuBisCO was used as a loading control (right panel). Two independent experiments were performed with similar results.

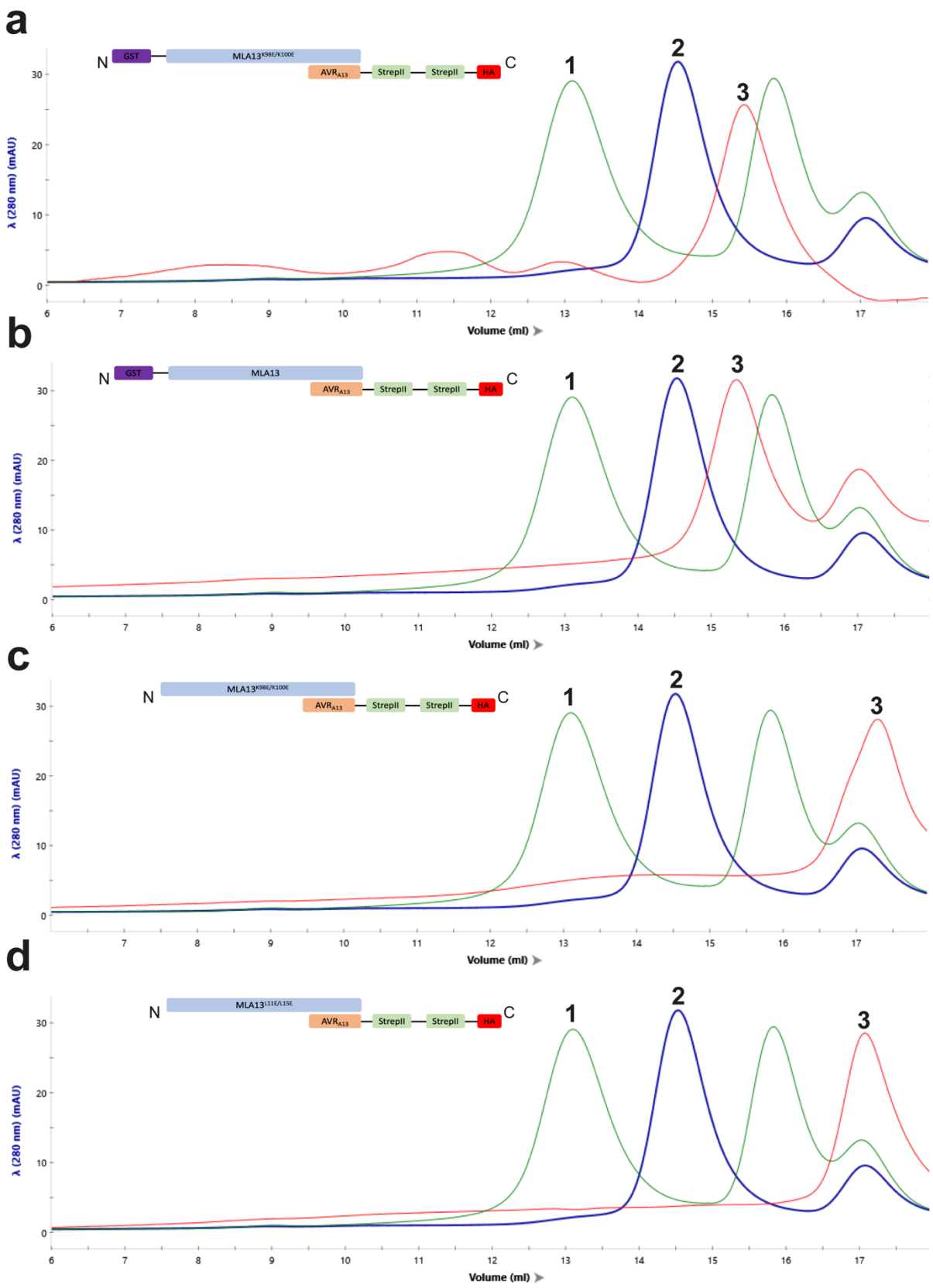

Extended Data Fig. 7 | SEC profiles from purification experiments of various MLA13-AVR$_{A13}$-1 constructs. SEC profiles of affinity-purified Sr35 (Sr35$^{L11E/L15E}$ (no tag) + AvrSr35-2Strep-HA; green trace) and Sr50 (Sr50$^{L11E/L15E}$ (no tag) + HA-2Strep-AvrSr50; blue trace) resistosomes. The blue and green resistosome traces are intended as size references for the traces of various MLA13-AVR$_{A13}$-1 constructs. Single-step affinity purification *via* the twin Strep tagged-effector followed by direct loading on SEC was used for all samples displayed. The Sr35 resistosome, Sr50 resistosome and MLA13-AVR$_{A13}$-1 heterocomplex are labelled as 1, 2 and 3, respectively. The MLA13-AVR$_{A13}$-1 heterocomplex consistently elutes at a later elution volume, indicating the extraction of a lower-order complex even under the exact same condition, tags and substitutions as Sr35 and Sr50 (see panel **d**).

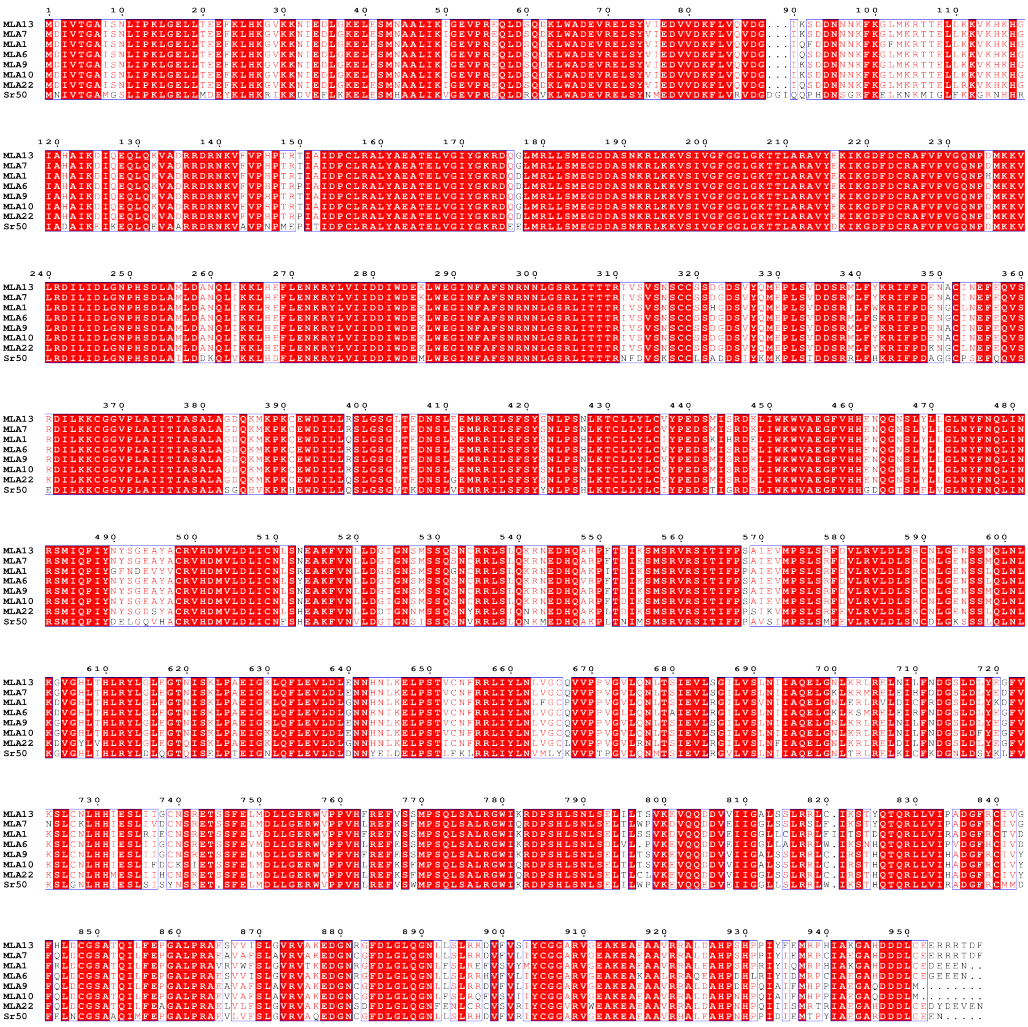

Extended Data Fig. 8 | Amino acid sequence alignment of all the MLAs that recognise a matching *Bh* effector and Sr50. Alignment performed using MUSCLE and visualised using ESPript 3.0.

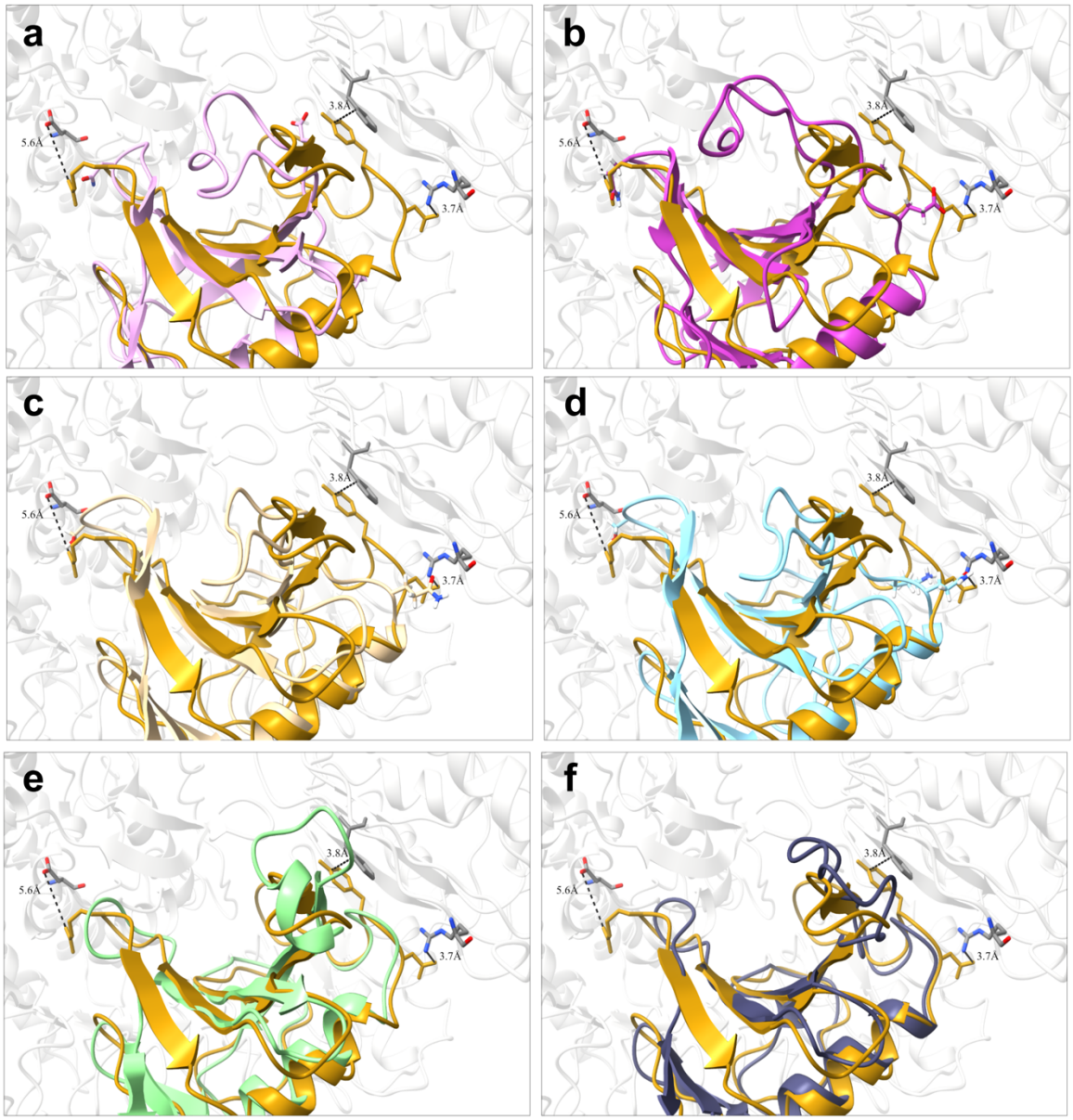

Extended Data Fig. 9 | Structural alignment of AVR$_{A13}$-1 in the heterodimer with the crystal structures of other effectors. Experimentally tested residues on AVR$_{A13}$-1 (dark goldenrod colour) that interact with MLA13 (transparent grey) are highlighted with proximity labels. Aligned effectors include **a,** AVR$_{A6}$, **b,** AVR$_{A7}$-2, **c,** AVR$_{A10}$, **d,** AVR$_{A22}$, **e,** CSEP0064, **f,** AvrPm2.

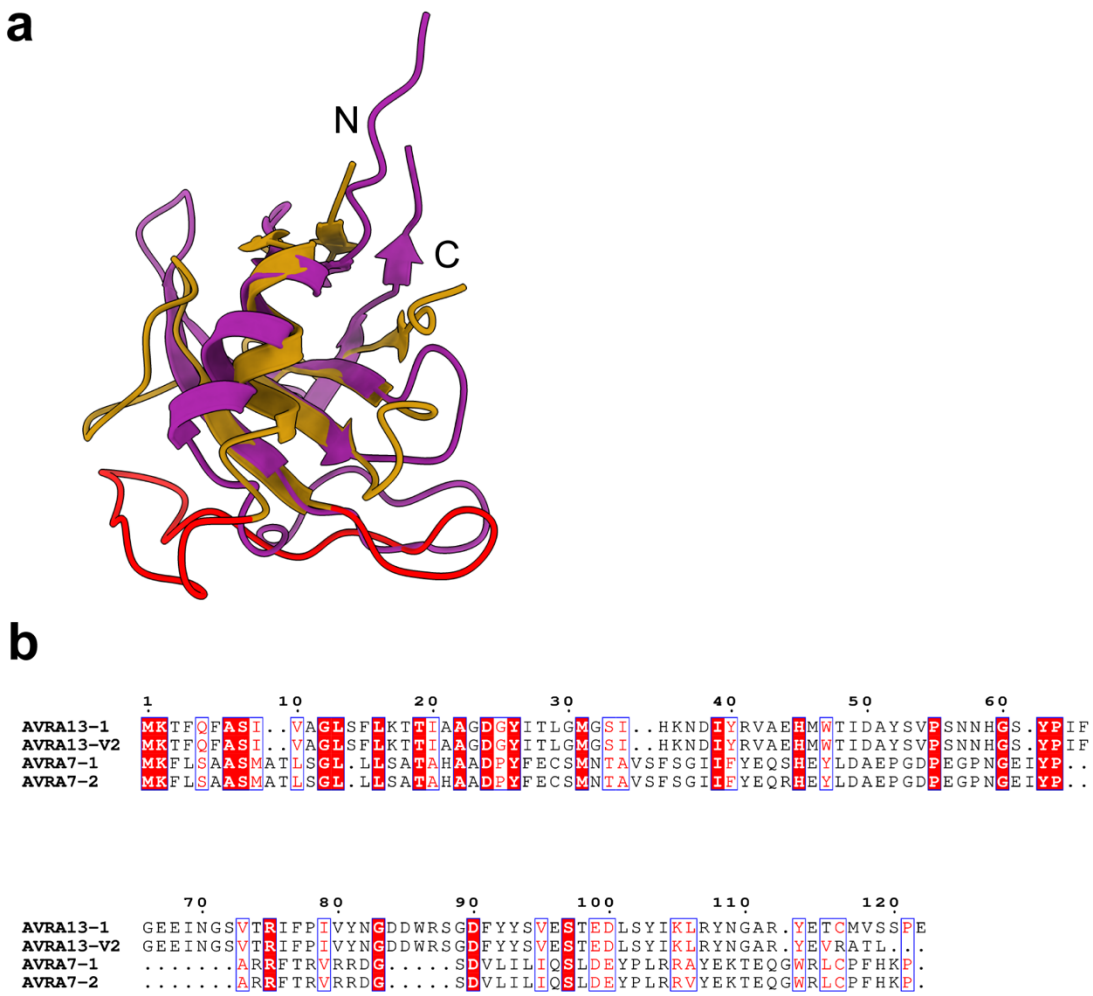

Extended Data Fig. 10 | Structural and sequence alignments of AVR_{A13} and AVR_{A7} variants. a, Structural alignment of AVR_{A13}-1 (dark goldenrod colour) and crystal structure of AVR_{A7}-1 (burgundy colour; PDB: 8OXL). The basal loops of AVR_{A13}-1 are coloured in red. **b,** Sequence alignment of AVR_{A13} and AVR_{A7} variants. Alignment performed using MUSCLE and visualised using ESPript 3.0.

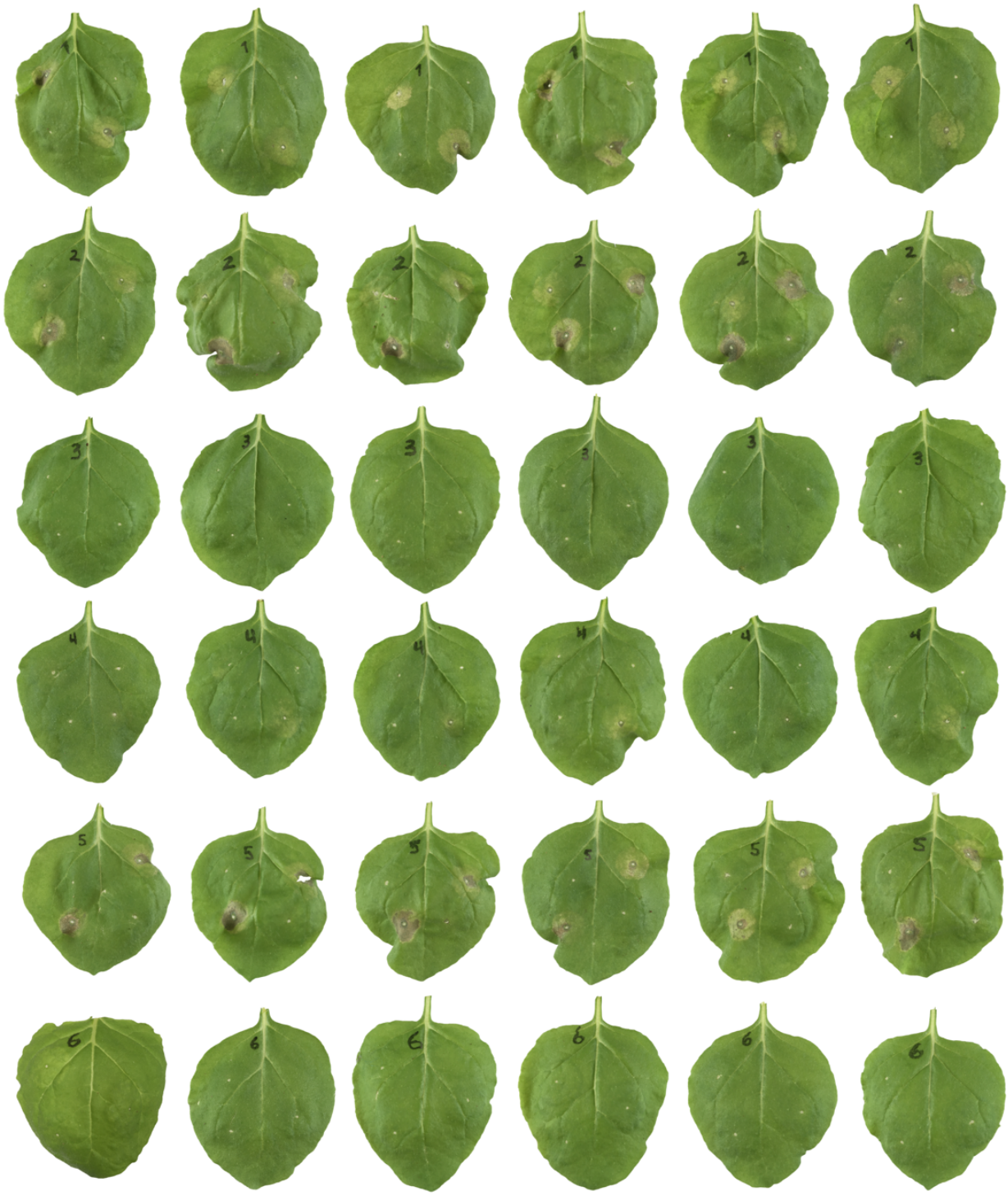

Supplementary Fig. 1 | Six replicates of *Agrobacterium*-mediated co-expression of MLA13 variants with AVR_{A13}-1 and AVR_{A22} in leaves of *N. benthamiana* from Extended Data Fig. 3. Infiltration points described below are ordered sequentially counterclockwise starting in the upper left corner of each leaf series. Leaf #1: MLA13 + AVR_{A13}-1, $MLA13^{L11E/L15E}$ + AVR_{A13}-1, $MLA13^{F99E}$ + AVR_{A13}-1, $MLA13^{K98E/K100E}$ + AVR_{A13}-1; leaf #2: $MLA13^{K98E/F99E/K100E}$ + AVR_{A13}-1, $MLA13^{D502V}$ + AVR_{A13}-1, $MLA13^{L11E/L15E/D502V}$ + AVR_{A13}-1, $MLA13^{K98E/K100E/D502V}$ + AVR_{A13}-1; leaf #3: $MLA13^{K207R}$ + AVR_{A13}-1, GST- MLA13 + AVR_{A13}-1, GST- $MLA13^{D502V}$ + AVR_{A13}-1. Leaves 4-6 are the same as leaves 1-3 except co-expression of AVR_{A22} replaces AVR_{A13}-1.

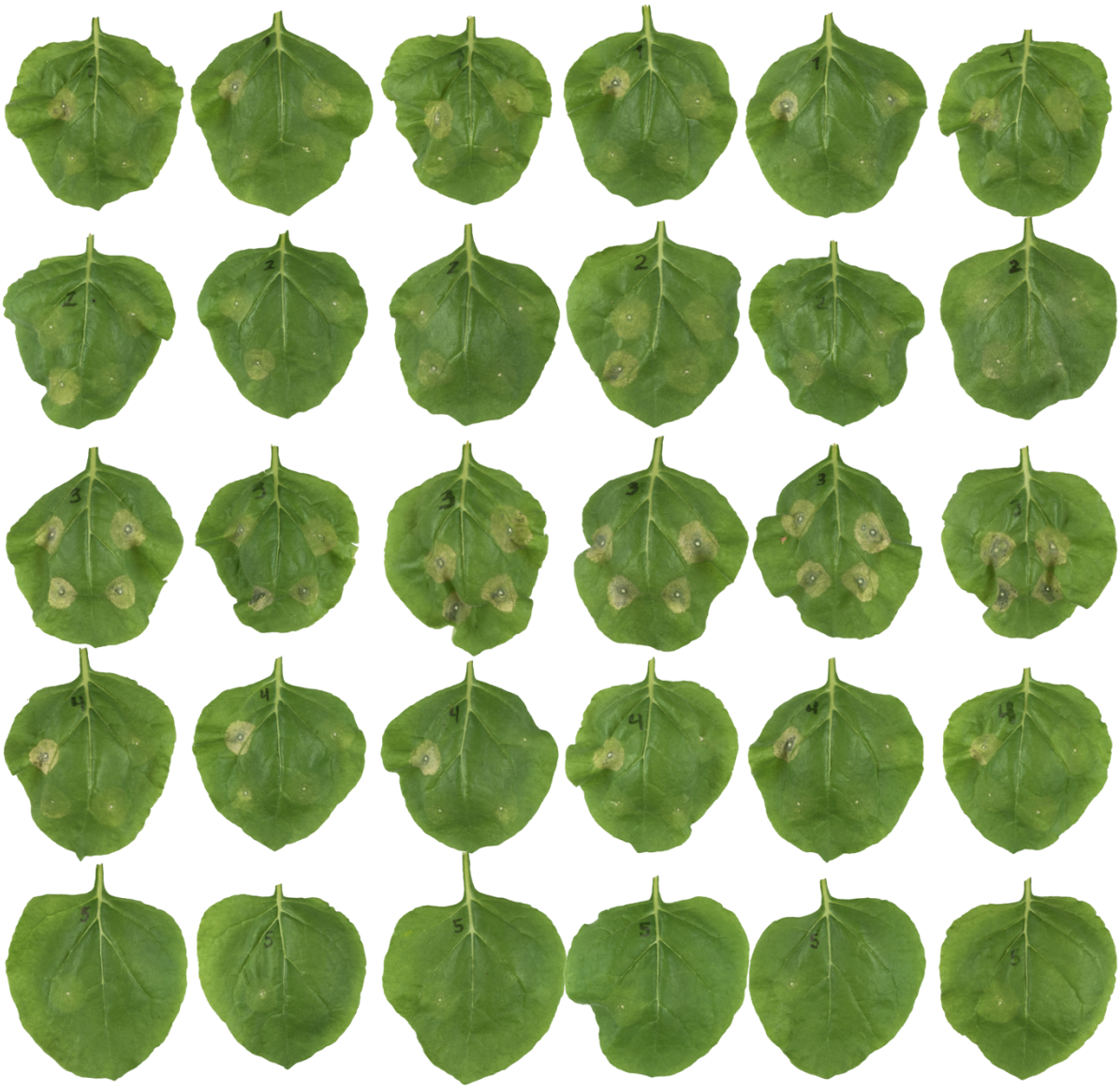

Supplementary Fig. 2 | Six replicates of *Agrobacterium*-mediated co-expression of AVR_{A13}-1 variants with MLA13 in leaves of *N. benthamiana* from Fig.3c. Infiltration points described below are ordered sequentially counterclockwise starting in the upper left corner of each leaf series. Leaf #1: AVR_{A13}-1 WT, AVR_{A22} WT, Y52A, P55A; leaf #2: N58A, H59A, G60A, F65A; leaf #3: G66A, Y81A, N82A, Y108A; leaf #4: N109A, Y52A/G60A, Y52A/F65A, G60A/F65A; leaf #5: Y52A/G60A/F65A.

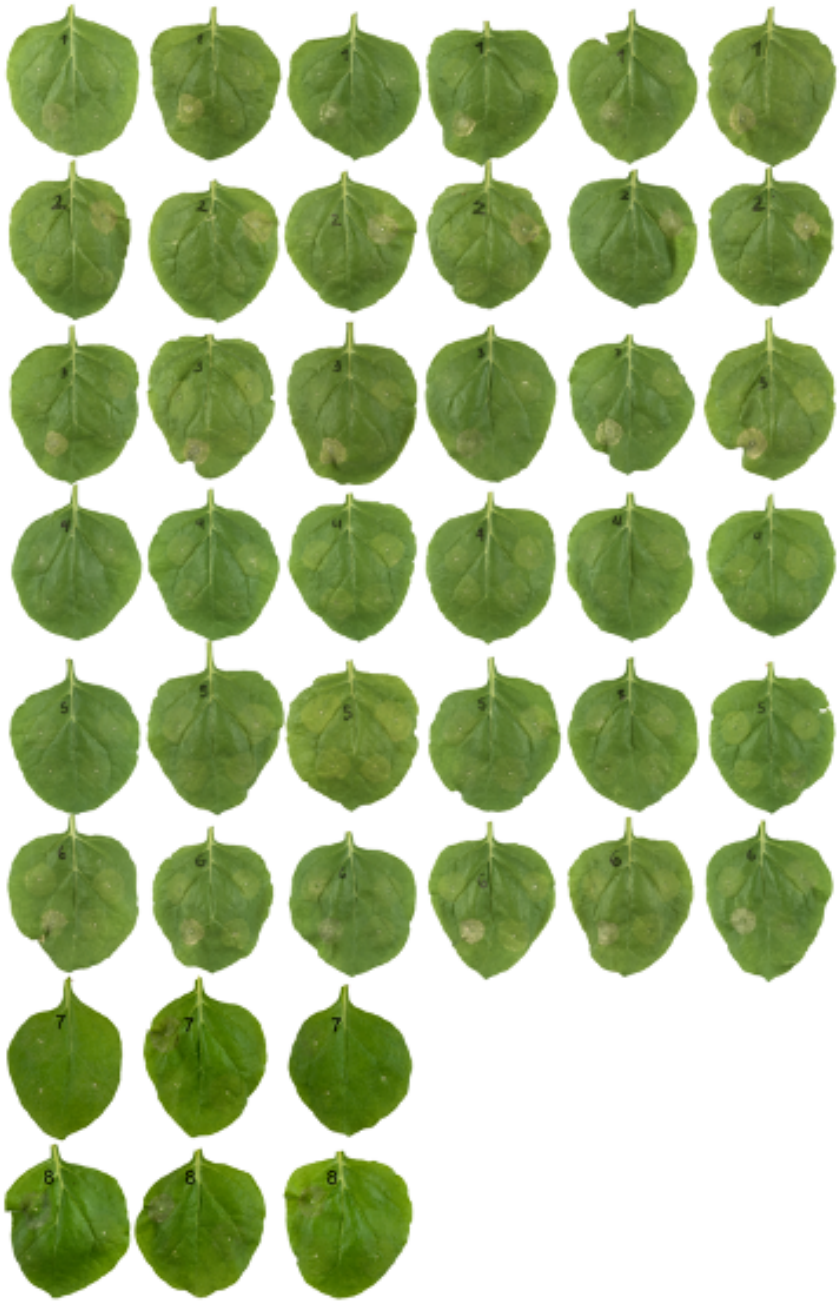

Supplementary Fig. 3 | Replicates of *Agrobacterium*-mediated co-expression of MLA13 variants with AVR_{A13}-1 and AVR_{A22} in leaves of *N. benthamiana* from Fig.4c. Infiltration points described below are ordered sequentially counterclockwise starting in the upper left corner of each leaf series. Leaf #1: MLA13 WT + AVR_{A22}, MLA13 WT + AVR_{A13}-1, Y491A + AVR_{A22}, Y491A + AVR_{A13}-1; leaf #2: Y496A + AVR_{A22}, Y496A + AVR_{A13}-1, H643A +, AVR_{A22}, H643A + AVR_{A13}-1; leaf #3: S902A + AVR_{A22}, S902A + AVR_{A13}-1, Y934A +, AVR_{A22}, Y934A + AVR_{A13}-1; leaf #4: E936A + AVR_{A22}, E936A + AVR_{A13}-1, Y491A/H643A +, AVR_{A22}, Y491A/H643A + AVR_{A13}-1; leaf #5: H643A/E936A + AVR_{A22}, H643A/E936A + AVR_{A13}-1, Y491A/E936A +, AVR_{A22}, Y491A/E936A + AVR_{A13}-1; leaf #6: S902A/F935A + AVR_{A22}, S902A/F935A + AVR_{A13}-1, Y491A/H643A/E936A +, AVR_{A22}, Y491A/H643A/E936A + AVR_{A13}-1; relevant infiltration points on leaves 7 and 8 start at position two; leaf #7: F900A + AVR_{A22}, F900A + + AVR_{A13}-1; leaf #8: R938A + AVR_{A22}, R938A + AVR_{A13}-1.

Supplementary Fig. 4 | Replicates of *Agrobacterium*-mediated co-expression of MLA7 and MLA7^{L902S} with effector variants in *N. benthamiana* as tested in Fig.5b. Leaf #1 and leaf #2 are co-expressed with *Mla7* WT and *Mla7*^{L902S}, respectively. Infiltration points described below are ordered sequentially counterclockwise starting in the upper left corner of each leaf series: *AVR*$_{a22}$, *AVR*$_{a7}$*-1, AVR*$_{a7}$*-2, AVR*$_{a13}$*-1, AVR*$_{a13}$*-V2*.

Supplementary Table 1 | Statistical output from cryo-EM data processing and structural model building.

Sample conditions		
Grid type	Quantifoil Cu R2/4 (200 mesh) + Graphene Oxide	
Cryo-EM data collection		
Microscope	Titan Krios G3i	
Voltage (kV)	300	
Spherical aberration (mm)	2.7	
Condenser C2 aperture (µm)	70	
Objective aperture size (µm)	100	
Camera	Falcon III	
Pixel size	0.862	
Total dose (electron*Å^{-2})	42	
Number of frames	42	
Images per hole	3	
Energy filter	None	
Defocus range (µm)	-2.0 to -0.3	
# micrographs collected	8,188	
# micrographs used	5,897	
Cryo-EM data processing		
software	cryosparc v4.4.1+patch240110	
Particles after 2D classification after 3D sorting	 115,686 48,191	
Resolution (FSC 0.143, Å)	3.8	
Model building and refinement		
Software for building	Coot 0.9.4.7 EL	
Residues build MLA13 AVRa13	 2-131,143-541,555-956 25-122	
Software for refinement	PHENIX 1.21 - 5207	
Composition (#) Chains Atoms Residues Water Ligands	 2 8127 (Hydrogens: 0) Protein: 1029 0 0	
Bonds (RMSD) Length (Å) (# > 4σ) Angles (°) (# > 4σ)	 0.002 (0) 0.518 (1)	
MolProbity score	2.04	
Clash score	8.96	
Ramachandran plot (%) Outliers Allowed Favored	 0.10 10.19 89.72	
Rama-Z (Z-score, RMSD) whole (N = 1021) helix (N = 331) sheet (N = 156) loop (N = 534)	 -2.06 (0.26) -0.17 (0.29) -0.63 (0.46) -2.39 (0.25)	
Rotamer Outliers (%)	0.0	
Peptide plane (%) Cis proline/general Twisted proline/general	 2.8/0.0 0.0/0.0	
CaBLAM outliers (%)	6.81	
Supplied Resolution (Å)	3.5	
Resolution Estimates (Å) d 99 (full) d model d FSC model (0/0.143/0.5)	Masked 2.5 2.2 1.7/2.0/3.7	Unmasked 2.5 2.2 1.7/2.0/3.7
Model vs. Data CC (mask CC (box) CC (peaks) CC (volume)	 0.71 0.71 0.69 0.72	

Chapter 3: A versatile protocol for purifying recombinant protein from *Nicotiana benthamiana*

A versatile protocol for purifying recombinant proteins from *Nicotiana benthamiana*

Aaron W. Lawson[1], Arthur Macha[2], Ulla Neumann[3], Monika Gunkel[2], Jijie Chai[1,2,3], Elmar Behrmann[2], Paul Schulze-Lefert[1,5]

Corresponding authors: Jijie Chai, Elmar Behrmann, Paul Schulze-Lefert

Affiliations

[1]Department of Plant Microbe Interactions, Max Planck Institute for Plant Breeding Research, Cologne 50829, Germany
[2]Institute of Biochemistry, University of Cologne, Cologne 50674, Germany
[3]Central Microscopy, Max Planck Institute for Plant Breeding Research, Cologne 50829, Germany
[4]School of Life Sciences, Westlake University, Hangzhou 310031, China
[5]Cluster of Excellence on Plant Sciences (CEPLAS), Max Planck Institute for Plant Breeding Research and University of Cologne, Germany

Abstract

Structural biology is an indispensable tool in many research areas to uncover molecular mechanisms underlying the regulation of biological processes. Although structural modelling tools become increasingly powerful in their predictions, especially due to the inclusion of deep-learning approaches, experimentally resolved structures are still irreplaceable to guide structure-function studies through site-directed mutagenesis. Major obstacles to experimental structural studies of regulatory protein heterocomplexes persist such as the necessity of high protein concentration and purity in conditions that are compatible with downstream analyses such as cryogenic electron microscopy (cryo-EM). The use of *Nicotiana benthamiana* leaves as a transient expression system for recombinant proteins has become an increasingly attractive approach as the plant is inexpensive to cultivate, grows rapidly, allows fast experimental turnaround and is easily scalable compared to other established systems such as insect cell cultures. We present here a robust and versatile protocol exemplified for the purification of five heterocomplexes composed of immunoreceptors and their associated pathogen effectors ranging in size from ~660 kD to ~140 kD from *N. benthamiana*, followed by electron microscopy. Using our plant-based protocol, we verified the structure of the insect cell-derived wheat Sr35 resistosome, while co-purifying and co-resolving a ~140 kD homodimer of the AvrSr35 effector of the fungus *Puccinia graminis* f sp *tritici* (*Pgt*). In most cases, only a single epitope tag is needed for heterocomplex purification, reducing complications that come with multiple epitope tags and two-step affinity purifications. We highlight codon usage, signal peptide fusion and epitope tag choice among other factors critical for recombinant protein expression in *N. benthamiana* leaves.

Introduction

Structural biology is a key technology in the life sciences that offers fundamental insights into the molecular mechanisms of life. By uncovering the 3D architecture of

proteins and protein complexes, structural biology tools enable a deeper understanding of biological processes. Recent interest in the field is documented by a ~33-fold increase in Electron Microscopy Data Bank (EMDB) entries released in the resolution range of 3-4 Å from 2015-2023 (emdataresource.org)[1,2]. The equipment needed for performing such experiments are becoming more widely accessible and data processing has become more user friendly. Although technologies to acquire and process EM data are constantly improving, significant biochemical barriers persist for resolving some of the most challenging protein complexes[3]. The purification of some proteins can be limited by low expression levels, incompatible expression conditions and unknown extraction conditions that maintain protein stability[3].

Selecting a suitable expression system is a major consideration for each protein purification project[4]. Well-established expression systems such a *E. coli*, yeast, mammalian and insect cell cultures have shown remarkable results while each one has their limitations[4]. For example, insect cell cultures are commonly used for expressing challenging, large protein complexes, however, this system can be cumbersome when optimising an expression/purification protocol due to comparatively low experimental turnaround time. For example, insect cell culture expression can require up to four weeks from cloning to purification due to iterative infection and scaling steps, significantly delaying optimisation of critical parameters such as placement of epitope tags. Moreover, cell culture expression systems are susceptible to microbial contamination, risking the viability of stock cultures and weeks of preparation and resources such as costly insect cell culture media. Alternatively, facile *Agrobacterium tumefaciens*-mediated transient transformation of *Nicotiana benthamiana* leaves has been an attractive approach for the production of biopharmaceuticals and is more recently popularised for experiments involving large protein complexes for structural studies[5]. For example, the *N. benthamiana* disease resistance complex, termed the ROQ1 resistosome, among other resistance complexes, were purified and resolved using transient expression in *N. benthamiana* leaves[6-10]. Although one published method exists for guiding the expression and purification of recombinant protein complexes from *N. benthamiana* for structural studies, optimised parameters that can be generally applied for the purification of a range of different proteins while yielding higher protein concentration and purity is lacking[11].

Here we present how codon alteration of target sequences for expression in *N. benthamiana* or *Spodoptera frugiperda* result in striking increases in protein yield compared to expressing native sequences in *N. benthamiana leaves*. In addition, we show how our *N. benthamiana* expression and purification protocol is applicable to a range of diverse proteins and complexes. We demonstrate this with the purification of both the wheat Sr35 resistosome and the *Puccinia graminis* f sp *tritici* (*Pgt*) AvrSr35 homodimer using a single-step affinity chromatography approach followed by size exclusion chromatography[12,13]. In addition, we highlight the versatility of the protocol through the purification of the wheat Sr50 resistosome, the barley MLA13-AVR_{A13}-1 heterodimer and a MLA3-Pwl2 heterocomplex[14].

Development of the protocol and key considerations

Identifying critical parameters for the *N. benthamiana* expression and purification system was central to developing this protocol and its extension to a diverse range of protein classes and conformations. Firstly, we found that changing codon usage of the target nucleotide sequence for expression in *N. benthamiana* or *S. frugiperda*

significantly elevates protein accumulation. Codon alteration does however come with potential risks such as unintended changes to post-translational modification sites, conformation and function of the target protein which needs to be considered during preliminary trials[15]. Mitigating high concentrations of polyphenols in *N. benthamiana* leaf extract is also integral to formulating a buffer condition that is benign to the target protein. The oxidising environment and high concentration of polyphenols in leaf extracts requires the use of additives to minimise deleterious effects on target proteins. To mitigate these harsh lysate conditions, we added various concentrations of polyvinylpyrrolidone (PVP) and polyvinylpolypyrrolidone (PVPP) to sequester polyphenols, but found that these polymers severely reduced the yield of the target protein[16]. Alternatively, we found that the use of the dithiothreitol (DTT) as a reducing agent was suitable for preventing oxidising conditions in the lysate. Moreover, we found that increasing the concentration of DTT up to 50 mM can increase the yield of some proteins tested, however, integrity of the protein was not assessed when using elevated DTT concentrations.

The choice of epitope tag and terminal on which it is fused to the target proteins were critical considerations when developing this protocol. Upon testing several epitope tags (i.e. His, FLAG, GST, Strep-tag®II) we found that the Twin-Strep-tag® was the most suitable. We then generated two Gateway-compatible expression vectors that encode a N- or C-terminal Twin-Strep-tag® in the vector backbone (pGWB402SC and pGWB402SN). Notable advantages of the Twin-Strep-tag® include its relatively small size, reducing the risk of interference with native protein conformations. Additionally, Twin-Strep-tag® and the Strep-Tactin® XT affinity resin used here are seemingly stable in the presence of reducing agents in the lysate such as DTT, unlike other tag-resin combinations such as FLAG. The Twin-Strep-tag® system is also desirable due to low operating costs of the Strep-Tactin® XT affinity resin and biotin as an elution agent compared to the use of costly peptides. Moreover, combing the Twin-Strep-tag® system with the use of BioLock, a product used for masking non-target biotinylated proteins, results in remarkably pure target protein samples, an essential attribute for samples intended for structural analysis.

Results

Codon alteration for different expression systems drastically increases protein yield from *N. benthamiana leaves*

The effect of codon alteration on protein yield was tested *via* western blot (WB) band intensity and found to drastically increase the yield of proteins from a broad range of species and protein classes when expressed in *N. benthamiana* leaves. Firstly, we found that *Hordeum vulgare Mla3* codon altered for expression in *N. benthamiana* resulted in a ~53-fold increase in WB band intensity compared to that of the native sequence (Fig. 1). Counterintuitively, codon alteration of *Mla3* for expression in *Spodoptera frugiperda* resulted in a ~120-fold increase in WB band intensity compared to that of the original barley coding sequence (Fig. 1), indicating that other mechanisms than codon adjustment to the non-native expression host influence recombinant protein yield in *N. benthamiana*. Conversely, codon alteration of *Arabidopsis thaliana MLKL1* for expression in *N. benthamiana* was higher (~106-fold) than when codon usage was altered for expression in *S. frugiperda* (~90-fold) (Fig. 1). Similarly, human SARM1 accumulated to higher levels when codon altered for expression in *N. benthamiana* (~26-fold) than when codon altered for expression

in *S. frugiperda* (~21-fold; Fig. 1) when compared to the native codon sequence (Fig. 1). In addition, codon altering wheat (*Triticum monococcum*) *Sr35* and *A. thaliana RPP1* for expression in *N. benthamiana* resulted in ~49-fold and ~11-fold increases in band intensity compared to the native coding sequences, respectively (Extended Data Fig. 1). We also tested the effect of codon alteration on the protein yield of a fungal effector protein *Blumeria graminis* AVR_{a22}. Consistent with the aforementioned results with NLR receptors and MLKL, codon alteration of AVR_{a22} for expression in *N. benthamiana* resulted in a ~20-fold increase in steady-state protein levels compared to that of the native sequence (Extended Data Fig. 1). We conclude that codon alteration is a major factor determining the yield of recombinant proteins in *N. benthamiana*. All replicates and loading controls are reported in Extended Data Fig. 2.

Expression of the signal peptide can increase protein accumulation of effector proteins

Expressing *Bg*AVR_{A22} with the signal peptide was found to increase protein yield ~40-fold when compared to expressing the protein without the signal peptide (Fig. 1b). Functionality of *Bg*AVR_{A22} with the signal peptide was assessed by co-expression with the matching receptor MLA22 and found to result in an enhanced cell death response when compared to co-expression of the receptor with *Bg*AVR_{A22} without the signal peptide (Extended Data Fig. 3c). Similarly, expressing *Mo*Pwl2 with the signal peptide was found to increase protein yield ~2-fold when compared to expressing the protein without the signal peptide (Fig. 1b). Functionality of *Mo*Pwl2 with the signal peptide was assessed by co-expression with MLA3 and found to result in a reduced cell death response when compared to co-expression of the receptor with *Bg*AVR_{A22} without the signal peptide (Extended Data Fig. 3d).

The Sr35 resistosome and AvrSr35 homodimer are purified from a single extraction from *N. benthamiana leaves*

The co-expression of Sr35 (codon altered for expression in *S. frugiperda*) and AvrSr35 (native sequence) in leaves of *Nb* resulted in the oligomerisation and extraction of both the Sr35 resistosome and AvrSr35 homodimer[12,13]. Introduction of the substitutions $Sr35^{L11E/L15E}$ allowed for protein accumulation while preventing *in planta* cell death. Expression of $Sr35^{L11E/L15E}$ without an epitope tag reduced potential interference of the tag with protein folding and oligomerization as well as potential complications arising from a second-step affinity chromatography purification, including reduced protein yield. Further, AvrSr35 was expressed with the C-terminally-fused Twin-Strep-HA tag. A single-step affinity purification *via* the Twin-Strep-tag on AvrSr35 resulted in the enrichment of both AvrSr35 and Sr35 with low levels of residual off-target proteins (Fig. 2a). The sample was then analysed by size exclusion chromatography (SEC) which resulted in the elution of two distinctly separated molecules (Fig. 2b). Subsequent SDS-PAGE of individual SEC fractions indicated that the higher molecular weight peak marked the elution of the Sr35 resistosome while the subsequent, lower molecular weight peak indicated the elution of the AvrSr35 homodimer (Fig. 2b). Negative staining and transmission electron microscopy (TEM) images of the fractions containing putative Sr35 resistosomes revealed the presence of homogenous, pentamer-shaped particles, suggesting the presence of the Sr35 resistosome (Fig. 2c). Fractions putatively containing the AvrSr35 homodimer were not analysed by negative staining and TEM, but rather directly with cryo-EM (Fig. 2e).

Cryo-EM analysis of the Sr35 resistosome sample resulted in the acquisition of 1,272 movies of which 1,226 high-quality micrographs were selected for further processing (Extended Data Fig. 3). Putative particles amounted to 163,541 of which 68,164 were used for map building. The global resolution of the unmasked resistosome was 2.6 Å (Fig. 2d). The distal, LRR bound AvrSr35 proteins were least resolved, resulting in C1 local refinement and a masked, global resolution of 2.5 Å (Extended Data Fig. 4). Our Sr35 resistosome map purified from *N. benthamiana* is virtually indistinguishable from the previously reported cryo-EM structures obtained from material overexpressed in insect cells and *E. coli*, although our map comprised only 70k particles from 1,200 movies compared to 798k particles from 5,292 micrographs in Förderer *et al.* (2022) and 558k particles from 3,194k micrographs in Zhao *et al.* (2022; Extended Data Fig. 5a)[17,18]. Cryo-EM analysis of the putative AvrSr35 homodimer sample resulted in the acquisition of 4,004 movies of which 3,896 high-quality micrographs were selected for further processing (Extended Data Fig. 6). Putative particles amounted to 463,010 of which 250,926 were high-quality and used for map building. The global resolution of the resulting AvrSr35 homodimer was 3.2 Å (Fig. 2e). Interestingly, we found that our cryo-EM density map of the AvrSr35 homodimer presents a different subunit orientation that is rotated six degrees from the interface compared to that of the crystallised homodimer reported by Zhao *et al* (2022; Extended Data Fig. 5b)[18].

A pentameric Sr50 resistosome is purified from leaves of *N. benthamiana*

Co-expression of wheat Sr50 (codon altered for expression in *S. frugiperda*) and AvrSr50 (native sequence) in leaves of *Nb* resulted in the oligomerisation and extraction of a putative pentameric Sr50 resistosome. Similar to Sr35, introduction of the substitutions $Sr50^{L11E/L15E}$ allowed for protein accumulation while preventing *in planta* cell death. $Sr50^{L11E/L15E}$ was expressed with C-terminally-fused Twin-Strep-HA tags while AvrSr50 was expressed without an epitope tag to reduce potential tag interference with proper folding of the native protein and potential complications arising from a second-step affinity chromatography. It is notable that expression and purification of Sr50 and AvrSr50 with the same tag format as the Sr35 resistosome did not result in the purification of a resistosome, highlighting the importance of testing the placement of the Twin-Strep tag on various terminals of the two proteins. A single-step affinity purification *via* the Twin-Strep-tag on $Sr50^{L11E/L15E}$ resulted in the enrichment of both $Sr50^{L11E/L15E}$ and AvrSr50 with low levels of off-target proteins (Fig. 3a). The sample was then analysed by SEC which resulted in the elution of an oligomerized receptor, the putative Sr50 resistosome (Fig. 3b). Negative staining and TEM images of the sample containing putative Sr50 resistosomes indeed revealed the presence of homogenous, pentamer-shaped particles suggesting the purification of the Sr50 resistosome (Fig. 3c).

An MLA13-AVR_{A13}-1 heterodimer is purified and resolved from leaves of *N. benthamiana*

Co-expression of barley MLA13 (codon altered for expression in *S. frugiperda*) and *Bg* AVR_{A13}-1 (without signal peptide; codon altered for expression in *N. benthamiana*) resulted in the isolation of and structural resolution of a stable heterodimer as reported by Lawson *et al*. (2022).[14] Expression of MLA13 with the substitutions $MLA13^{K98E/K100E}$ prevented *in planta* cell death while promoting protein accumulation. Similar to the purification of the aforementioned resistosomes, a first-step affinity purification *via* the C-terminally-fused Twin-Strep tag on AVR_{A13}-1

247 resulted in the enrichment of both MLA13 and AVR_{A13}-1 (Fig. 4a). Contrary to the
248 purification of the aforementioned resistosomes, a second-step affinity purification
249 was performed *via* the N-terminally-fused GST tag on MLA13, resulting in the
250 enrichment of both proteins (Fig. 4a). The sample was then analysed using SEC and
251 the peak fraction eluting at ~15.5 mL was imaged using negative staining and TEM
252 (Fig. 4b,c). The pre-SEC sample was used for analysis by cryo-EM to resolve the
253 structure of the MLA13-AVR_{A13}-1 heterodimer[14].
254
255 **An MLA3-Pwl2 heterocomplex is purified from leaves of *N. benthamiana***
256 Co-expression of barley MLA3 (codon altered for expression in *S. frugiperda*) and
257 the *Magnaporthe oryzae* effector Pwl2 (without signal peptide; native sequence)
258 resulted in the copurification of a heterocomplex with a SEC elution profile
259 resembling a deduced receptor-effector heterodimer. Expression of MLA3 with the
260 substitutions $MLA3^{K98E/K100E}$ prevented *in planta* cell death while promoting protein
261 accumulation. Similar to the purification of the aforementioned resistosomes, a
262 single-step, affinity purification *via* the C-terminally-fused Twin-Strep tag on Pwl2
263 resulted in the enrichment of both N-terminal GST-tagged $MLA3^{K98E/K100E}$ and Pwl2
264 (Fig. 4d). The sample was then concentrated and analysed using SEC revealing the
265 co-elution of both MLA3 and Pwl2 at a volume of~15 mL, similar to that of the
266 MLA13-AVR_{A13}-1 heterodimer.
267

268 Materials

269

270 Biological materials

271 - Chemically competent *E. coli* (DH5α) cells.
272 - Electrocompetent *A. tumefaciens* cells (GV3101 (pMP90))
273 - Wild-type *N. benthamiana* plants
274

275 Reagents

276 - TE buffer (Thermo Fisher, cat. no. 12090015)
277 - LR Clonase (Thermo Fisher, cat. no. 117910430)
278 - Expression vector plasmid DNA (pGWB402SC, pGWB402SN and pGWB424)
279 - LB broth (Carl Roth, cat. no. X968.1)
280 - Agar (Carl Roth, cat. no. 2266.1)
281 - Spectinomycin dihydrochloride pentahydrate (spectinomycin; Sigma-Aldrich
282 cat. no. S4014)
283 - Gentamicin sulfate (gentamycin; Sigma-Aldrich, cat. no. G4918)
284 - Rifampicin (Sigma-Aldrich, cat. no. R3501)
285 - Kanamycin (Sigma-Aldrich, cat. no. K1876)
286 - NucleoSpin Plasmid, Mini Kit for Plasmid DNA (Machery-Nagel, cat. no.
287 740588.50)
288 - Magnesium chloride (Carl Roth, cat. no. KK36.1)
289 - MES monohydrate (Carl Roth, cat. no. 6066.3)
290 - Acetosyringone (Sigma-Aldrich, cat. no. D134406)
291 - DTT (Thermo Fisher, cat. no. R0861)
292 - Sodium chloride (Carl Roth, cat. no. 9265.2)
293 - Tris (Carl Roth, cat. no. 5429.2)
294 - Glycerol (Carl Roth, cat. no. 7530.4)

- Tween 20 (polysorbate 20; Sigma-Aldrich, cat. no. P1379)
- Protease inhibitor mix P (Serva, cat. no. 39103.01)
- BioLock (IBA, cat. no. 2-0205-050)
- Strep-Tactin XT Sepharose (Cytiva, cat. no. 29401324)
- Glutathione Sepharose 4B resin (Cytiva, cat. no. 17075601)
- Biotin (Sigma-Aldrich, cat. no. B4501)
- L-Glutathione reduced (Roth, cat. no. 6382.1)
- SDS PAGE running buffer (Bio-Rad, cat. no. 1610732)
- Uranyl acetate (Science Services, cat. no. E22400-1)
- Liquid ethane

Equipment

- Protein LoBind Tubes: 1.5 mL, 5 mL 15 mL, 50 mL (Eppendorf, cat. nos. 0030108132, 0030108302, 0030122216 and 0030122240, respectively)
- One millilitre infiltration syringes
- TGX FastCast Acrylamide Kit (BioRad, cat. no. 1610173)
- Superose 6 Increase 10/300 GL size exclusion chromatography column (Cytiva, cat. no. GE29-0915-96)
- HPLC
- Negative staining TEM grids (Electron Microscopy Services, cat. nos. CF400-Cu-50)
- Graphene oxide cryo-EM grids (Science Services, cat. no. ERGOQ200R24Cu50).
- TEM (Talos L120C)
- Cryo-EM (Titan Krios G3)

Procedure

Cloning

• TIMING 2 d

1. The target coding DNA with or without stop codons is first transferred from entry/donor vector plasmid DNA into pGWB402SC, pGWB402SN or pGWB424 using the Gateway cloning system. Constructs to be coimmunoprecipitated *via* interaction with the epitope-tagged construct should be cloned into pGWB402SC with a stop codon. To do so, mix 2 μL TE buffer, 1 μL of 100 ng/μL entry/donor vector plasmid DNA, 1 μL of 100 ng/μL expression vector plasmid DNA and 1 μL of LR clonase in a 1.5 mL tube and incubate at 25 °C for 1 h. Add 50 μL of chemically competent *E. coli* (DH5α) cells to the reaction on ice followed by heat shock at 42 °C for 30 seconds before returning to ice. Add 500 μL of liquid LB broth and shake at 37 °C for 1 h. Pellet the transformed cells by centrifugation at 2,500 RCF for 3 min, resuspend and plate on LB + agar plates containing 100 μg of spectinomycin. Incubate plates at 37 °C for ~12 h. Pick one colony and grow in 5 mL of liquid LB containing 100 μg of spectinomycin for ~ 8 h. Isolate the plasmid DNA with a plasmid preparation kit and confirm sequence fidelity *via* sanger sequencing.

342 ## Transformation and culturing of *A. tumefaciens*
343 • **TIMING 4 d**
344 2. Thaw 10 μL of electrocompetent *A. tumefaciens* cells (GV3101 (pMP90)) on ice
345 and add 1 μL of 100 ng/μL expression vector plasmid DNA. Add the 11 μL to an
346 electroporation cuvette and electroshock according to cuvette and pulser
347 manufacturer guidelines. Resuspend transformed cells in 500 μL of liquid LB
348 broth and shake at 28 °C for 1 h. Plate an optimised volume of the culture on LB
349 + agar plates containing spectinomycin (100 μg/mL), gentamycin (25 μg/mL),
350 rifampicin (50 μg/mL) and kanamycin (25 μg/mL) and grown for two days at 28 °C
351 3. Inoculate a 10 mL starter culture of liquid LB broth containing the above
352 antibiotics with 3-4 colonies and shake at 28 °C for ~14 h.
353 4. Inoculate a 350 mL final culture of liquid LB broth containing the above antibiotics
354 with 2 mL of the starter culture and grow for ~ 14 h until the culture is in
355 logarithmic growth phase.
356 5. Pellet the final culture by centrifugation at 3,500 RCF for 15 min at 28 °C.
357 Resuspend the pellet in 60 mL of infiltration buffer (10 mM MES (pH 5.6), 10 mL
358 $MgCl_2$ and 500 μM acetosyringone). Measure, dilute and combine each individual
359 construct so that they have an OD_{600} of 1 in the final suspension.
360
361 ## *N. benthamiana* leaf infiltration and transient gene expression
362 • **TIMING 2 d**
363 6. Poke ~6 holes through the top of the 3-4 leaves closest to the top of the plant and
364 infiltrate the bacterial suspension into the holes *via* the adaxial side of the leaf.
365 Poke and infiltrate more holes until the entire leaf is infiltrated. Approximately 84
366 leaves will amount to ~100 g harvested leaf tissue.
367 7. Incubate the infiltrated plants in the dark at ~25 °C for ~24 h.
368 8. Transfer the plants back to normal growing conditions for a total of 48 h post
369 infiltration.
370 9. Harvest the infiltrated leaves by wrapping 25 g bunches in tin foil, freeze in liquid
371 nitrogen and store at -80 °C
372
373 ## Single-step affinity purification (100 g leaf tissue)
374 • **TIMING 8 h**
375 10. Prepare fresh lysis buffer (Buffer A; 200 mL) and wash buffer (Buffer B; 200 mL)
376 at room temperature by combining the following:
377 a. Buffer A:
378 i. 50 mM Tris-HCl (pH 7.4), 150 mM NaCl, 5% glycerol, 0.5%
379 Tween 20, 2 vials of Protease Inhibitor P, 10 mM DTT, 5%
380 BioLock and ddH_2O to 200 mL.
381 b. Buffer B:
382 i. 50 mM Tris-HCl (pH 7.4), 150 mM NaCl, 0.1% Tween 20, 2 mM
383 DTT and ddH_2O to 200 mL.
384 11. Adjust the pH of both Buffer A and Buffer B to 7.4 with HCl.
385 12. Sterile filter and split Buffer B into two separate flasks and cool to 4 °C. Buffer A
386 remains at room temperature.
387 13. Prepare the elution buffer (Buffer C) by adding 50 mM biotin to 10 mL Buffer B
388 while maintaining pH 7.4 with NaOH. Sterile filter and store at 4 °C.
389 14. Place a large mortar and pestle on ice and precool with liquid nitrogen.

15. Pulverise 2 × 25-gram frozen leaf bundles by pounding them several times between two hard surfaces. Add the particulate to the precooled mortar and pestle. Grind the leaf tissue to a fine powder while retaining its frozen state.
16. Add the pulverised leaf tissue to Buffer A while agitating rapidly on a magnetic stirrer.
17. Repeat steps 15 and 16 and let defrost to 4 °C while rotating at room temperature.
18. Once defrosted, centrifuge the lysate at 30,000 RCF for 15 min in 2 × 250 mL tubes and strain through a double layer of mira cloth. Repeat for a total of two times.
19. Partition the clarified lysate into 5 × 50 mL tubes.
20. Equilibrate 500 μL of StrepTactin XT resin by gently mixing it in 15 mL Buffer B and collecting by centrifugation at 200 RCF for 2 min.
21. Resuspend the collected resin with 5 mL lysate and distribute evenly across the 5 × 50 mL tubes of lysate.
22. Gently rotate the 5 × 50 mL tubes end-over-end for 30 minutes for protein binding to the resin (no noticeable yield difference between 30 min and 2 h binding times).
23. Collect the resin by centrifuging the 50 mL tubes at 200 RCF for 3 min.
24. Gently remove the lysate, gently resuspend each resin pellet with 1 mL of Buffer B and transfer the resin suspension to a 15 mL tube. Repeat to ensure complete resin retrieval.
25. Fill the resin-containing 15 mL tube with Buffer B and gently mix. Collect resin by centrifuging.
26. Remove Buffer B supernatant and repeat a total of 3 times.
27. Resuspend the resin with 1 mL of Buffer B and transfer to a 1.5 mL tube. Collect the resin by centrifuging at 100 g for 1 min. Repeat to ensure complete retrieval of the resin from the 15 mL tube.
28. Remove the final Buffer B supernatant and add 500 μL of Buffer C to the resin. Gently rotate end-over-end at 4 °C for 30 min.
29. Isolate the resin by centrifugation at 100 RCF for 1 min, store the protein-containing supernatant and add 500 μL more of Buffer E. Repeat a total of 5 times as to collect a total of 5 × 500 μL of protein sample.
30. Centrifuge all 5 eluates at 16,000 RCF for 1 min to remove any residual resin and remove supernatant. Combine all eluates.
31. Analyse protein purity and concentration and proceed to size exclusion chromatography if second-step affinity purification is not applicable.
32. Maintain the sample at 4 °C.

Second-step affinity purification (only necessary if using two different epitope tags)

- **TIMING 4 h**

33. Equilibrate Glutathione Sepharose 4B (GST) resin by adding 150 μL resin to 5 mL Buffer B in a 5 mL tube. Gently mix the suspension and isolate the resin by centrifuging at 100 RCF for 1 min before removing the supernatant (Buffer B).
34. Add the eluate from step no. 30 to the 5 mL tube containing the GST resin and gently rotate end-over-end at 4 °C for 2 h.
35. Prepare the GST elution buffer (Buffer D) by adding 50 mM reduced glutathione to 10 mL Buffer B while maintaining pH 7.4. Sterile filter and store at 4 °C.

36. Following binding to the GST resin, isolate the resin by centrifuging at 100 RCF for 1 min and remove the supernatant (flow through).
37. Transfer the resin to a 1.5 mL tube by resuspending in 1 mL Buffer B followed by isolating the resin by centrifuging at 100 RCF for 1 min. Wash the 5 mL tube with one more millilitre of Buffer B and add it to the 1.5 mL tube containing the resin. Isolate the resin by centrifuging at 100 RCF for 1 min. Add 150 μL Buffer D and rotate end-over-end at 4 °C for 2 h.
38. Following elution, isolate the resin by centrifuging at 100 RCF for 1 min. Remove the supernatant and centrifuge it at 16,000 RCF for 1 min to remove any residual resin.
39. Analyse protein purity and concentration.
40. Proceed to either SEC or directly to TEM and cryo-EM grid preparation.
41. Maintain the sample at 4 °C.

SEC analysis

• **TIMING 2 h**

42. Concentrate the final eluate to ~500 μL and load it into a 500 μL HPLC loop.
43. Run the sample on a Superose 6 Increase 10/300 GL column at 0.3 mL/min while collecting 500 μL fractions.
44. Analyse protein purity and concentration of the elution fractions.
45. Maintain the samples at 4 °C.

Negative staining and TEM

• **TIMING 20 min**

46. Serial-dilute the fraction/sample of interest in Buffer B.
47. Glow discharge EM grids according to manufacturer's guidelines.
48. Apply 6 μL to a grid and let incubate for 1 min.
49. Remove the excess sample by gently touching the edge of the grid to a piece of filter paper until no visible excess sample remains on the grid. Ensure that the grid does not completely dry.
50. Apply 6 μL of 1% uranyl acetate to the grid and let incubate for 1 min.
51. Remove the excess uranyl acetate by gently touching the edge of the grid to a piece of filter paper until no visible excess stain remains on the grid, allowing for gradient-wise stain application.
52. Allow grid air dry for 10 minutes before storage.

Cryo-EM grid preparation

• **TIMING 20 min**

53. Pre-cool and humidify a plunge freezer to 4 °C and 100% humidity.
54. Apply 3 μL of a highly concentrated sample to a graphene oxide grid and incubate the sample on the grid for 10 sec.
55. Blot the grid for 3 to 6 sec before plunge freezing into liquid ethane.
56. Store the grids at -80 °C until cryo-EM analysis.

Data availability

The EM maps for the Sr35 resistosome and AvrSr35 homodimer have been deposited in the EMDB under the accession codes XXX and XXX.

Acknowledgements

We thank the greenhouse team at MPIPZ for their expertise in providing high-quality *N. benthamiana* plants. We thank Neysan Donnelly for critical comments on an early version of this manuscript. We thank Arthur Macha, Petra Koechner, Sabine Haigis, Elke Logemann, Milena Malisic, Florian Kuemmel, Li Liu, Wen Song and Nitika Mukhi for their intellectual and experimental contributions. This work was funded by the Max-Planck-Gesellschaft (P.S.-L.), the Deutsche Forschungsgemeinschaft (DFG, German Research Foundation) in the Collaborative Research Centre Grant (SFB-1403 – 414786233 B08 to P.S.-L. and J.C.), Germany's Excellence Strategy CEPLAS (EXC-2048/1, project 390686111 to P.S.-L.), the Ministry of Culture and Science of the State of North Rhine-Westphalia (iHEAD to P.S.-L. and E.B.). We acknowledge access to the cryo-EM infrastructure of StruBiTEM (Cologne, funded by DFG Grant INST 216/949-1 FUGG), and to the computing infrastructure of CHEOPS (Cologne, funded by DFG Grant INST 216/512/1 FUGG).

Author contributions

P.S.-L., J.C., E.B. and A.W.L. conceived the study; A.W.L. performed experiments; U.N. and M.G. performed electron microscopy screening; A.W.L., E.B., J.C. and P.S.-L. analysed data; A.M. performed structural model building; P.S.-L., E.B. and A.W.L. wrote the manuscript.

Competing interests

The authors declare no competing interests.

References

1 Lawson, C. L. *et al.* EMDataBank unified data resource for 3DEM. *Nucleic Acids Res* **44**, D396-403 (2016). https://doi.org/10.1093/nar/gkv1126

2 Kühlbrandt, W. Biochemistry. The resolution revolution. *Science* **343**, 1443-1444 (2014). https://doi.org/10.1126/science.1251652

3 Takizawa, Y. *et al.* While the revolution will not be crystallized, biochemistry reigns supreme. *Protein Sci* **26**, 69-81 (2017). https://doi.org/10.1002/pro.3054

4 Schütz, A. *et al.* A concise guide to choosing suitable gene expression systems for recombinant protein production. *STAR Protoc* **4**, 102572 (2023). https://doi.org/10.1016/j.xpro.2023.102572

5 Yao, J., Weng, Y., Dickey, A. & Wang, K. Y. Plants as Factories for Human Pharmaceuticals: Applications and Challenges. *Int J Mol Sci* **16**, 28549-28565 (2015). https://doi.org/10.3390/ijms161226122

6 Martin, R. *et al.* Structure of the activated ROQ1 resistosome directly recognizing the pathogen effector XopQ. *Science* **370**, eabd9993 (2020). https://doi.org/doi:10.1126/science.abd9993

7 Liu, F. *et al.* The activated plant NRC4 immune receptor forms a hexameric resistosome. *bioRxiv*, 2023.2012.2018.571367 (2024). https://doi.org/10.1101/2023.12.18.571367

8 Selvaraj, M. *et al.* Activation of plant immunity through conversion of a helper NLR homodimer into a resistosome. *bioRxiv*, 2023.2012.2017.572070 (2023). https://doi.org/10.1101/2023.12.17.572070

9 Madhuprakash, J. *et al.* A disease resistance protein triggers oligomerization of its NLR helper into a hexameric resistosome to mediate innate immunity. *bioRxiv*, 2024.2006.2018.599586 (2024). https://doi.org/10.1101/2024.06.18.599586

10 Liu, F. *et al.* Activation of the helper NRC4 immune receptor forms a hexameric resistosome. *Cell* (2024). https://doi.org/10.1016/j.cell.2024.07.013

11 Martin, R., Liu, F. & Staskawicz, B. Isolation of Protein Complexes from Tobacco Leaves by a Two-Step Tandem Affinity Purification. *Curr Protoc* **2**, e572 (2022). https://doi.org/10.1002/cpz1.572

12 Liu, M.-X., Zhao, Y.-B., Li, Z.-K., Chen, T.-T. & Ouyang, S. Assembly and purification of AvrSr35-induced Sr35 resistosome and determination of its structure by cryo-EM. *STAR Protocols* **3** (2022). https://doi.org/10.1016/j.xpro.2022.101796

13 Förderer, A. *et al.* A wheat resistosome defines common principles of immune receptor channels. *Nature* **610**, 532-539 (2022). https://doi.org/10.1038/s41586-022-05231-w

14 Lawson, A. W. *et al.* The barley MLA13-AVR_{A13} heterodimer reveals principles for immunoreceptor recognition of RNase-like powdery mildew effectors. *bioRxiv*, 2024.2007.2014.603419 (2024). https://doi.org/10.1101/2024.07.14.603419

15 Mauro, V. P. & Chappell, S. A. A critical analysis of codon optimization in human therapeutics. *Trends Mol Med* **20**, 604-613 (2014). https://doi.org/10.1016/j.molmed.2014.09.003

16 Ranatunge, I., Adikary, S., Dasanayake, P., Fernando, C. D. & Soysa, P. Development of a Rapid and Simple Method to Remove Polyphenols from Plant Extracts. *Int J Anal Chem* **2017**, 7230145 (2017). https://doi.org/10.1155/2017/7230145

17 Förderer, A. *et al.* A wheat resistosome defines common principles of immune receptor channels. *Nature* **610**, 532-539 (2022). https://doi.org/10.1038/s41586-022-05231-w

18 Zhao, Y. B. *et al.* Pathogen effector AvrSr35 triggers Sr35 resistosome assembly via a direct recognition mechanism. *Sci Adv* **8**, eabq5108 (2022). https://doi.org/10.1126/sciadv.abq5108

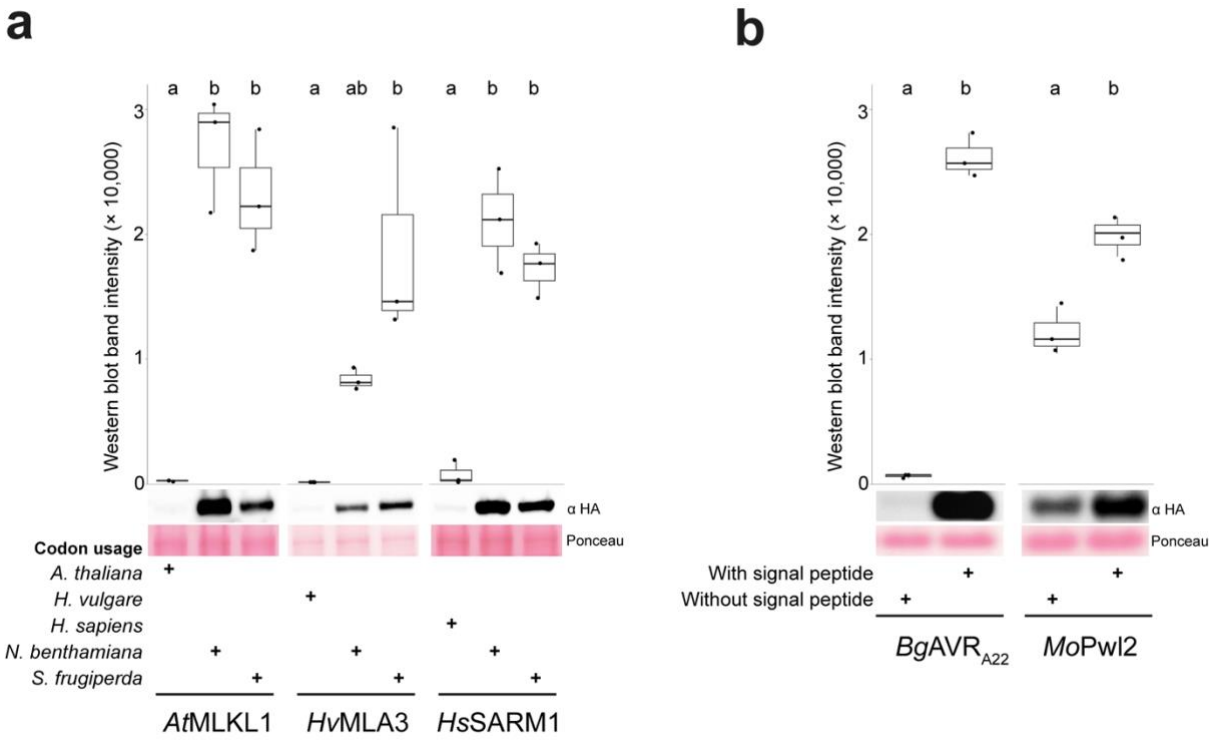

Fig. 1 | Codon alteration and signal peptides increase protein yield from transient expression in leaves of *N. benthamiana*. a, Transient expression comparison of native versus codon altered sequences *via* western blot band intensity. All samples were processed using the same method. Three replicates were performed for each treatment. A one-way ANOVA was performed followed by the Tukey's test. Differing letters indicate statistical difference ($p < 0.05$). All replicates and loading controls are reported in Extended Data Fig. 5. **b,** Transient expression comparison of *Bg*AVR$_{A22}$ and *Mo*Pwl2 with and without their signal peptides *via* western blot band intensity. All samples were processed using the same method. Three replicates were performed for each treatment. A one-way ANOVA was performed followed by the Tukey's test. Differing letters indicate statistical difference ($p < 0.05$).

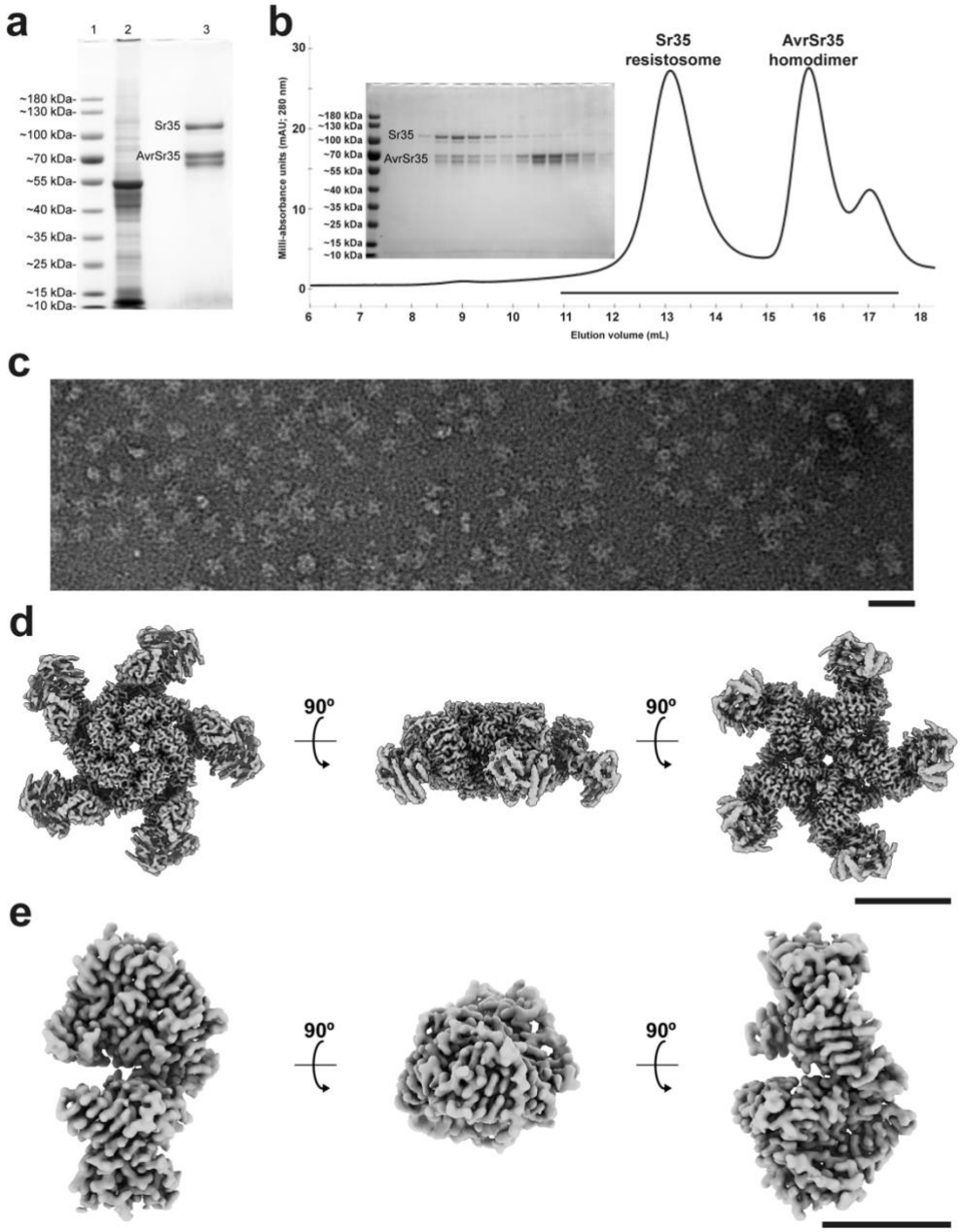

Fig. 2 | Purification and cryo-EM density maps of the Sr35 resistosome and the AvrSr35 homodimer extracted from leaves of *N. benthamiana*. a, CBB-stained SDS PAGE gel of a single-step affinity purification of C-terminal Twin-Strep-HA-tagged AvrSr35 and untagged $Sr35^{L11E/L15E}$. Lane #1: molecular weight ladder. Lane #2: total lysate (5 μL loaded). Lane #3: Enrichment of AvrSr35 *via* the Twin-Strep-HA tag co-enriches untagged $Sr35^{L11E/L15E}$ (45 μL/2.5 mL loaded). **b,** SEC profile of the concentrated sample stained in (**a**) displaying the separation and elution of the Sr35 resistosome and AvrSr35 homodimer. Inset CBB-stained SDS PAGE gel displays fractions eluted along the black line on the x-axis. **c,** Negative staining EM micrograph of a diluted sample of the 13 mL elution fraction from (**b**). Black line represents 50 nm. **d,** Three orientations of the Sr35 resistosome cryo-EM density map (global resolution of 2.7 Å) from a concentrated sample of the 13 mL elution fraction in (**b**). Black line represents 10 nm. **e,** Three orientations of the AvrSr35 cryo-EM density map (global resolution of 3.5 Å) from a concentrated sample of the 15.5 mL elution fraction in (**b**). Black line represents 10 nm.

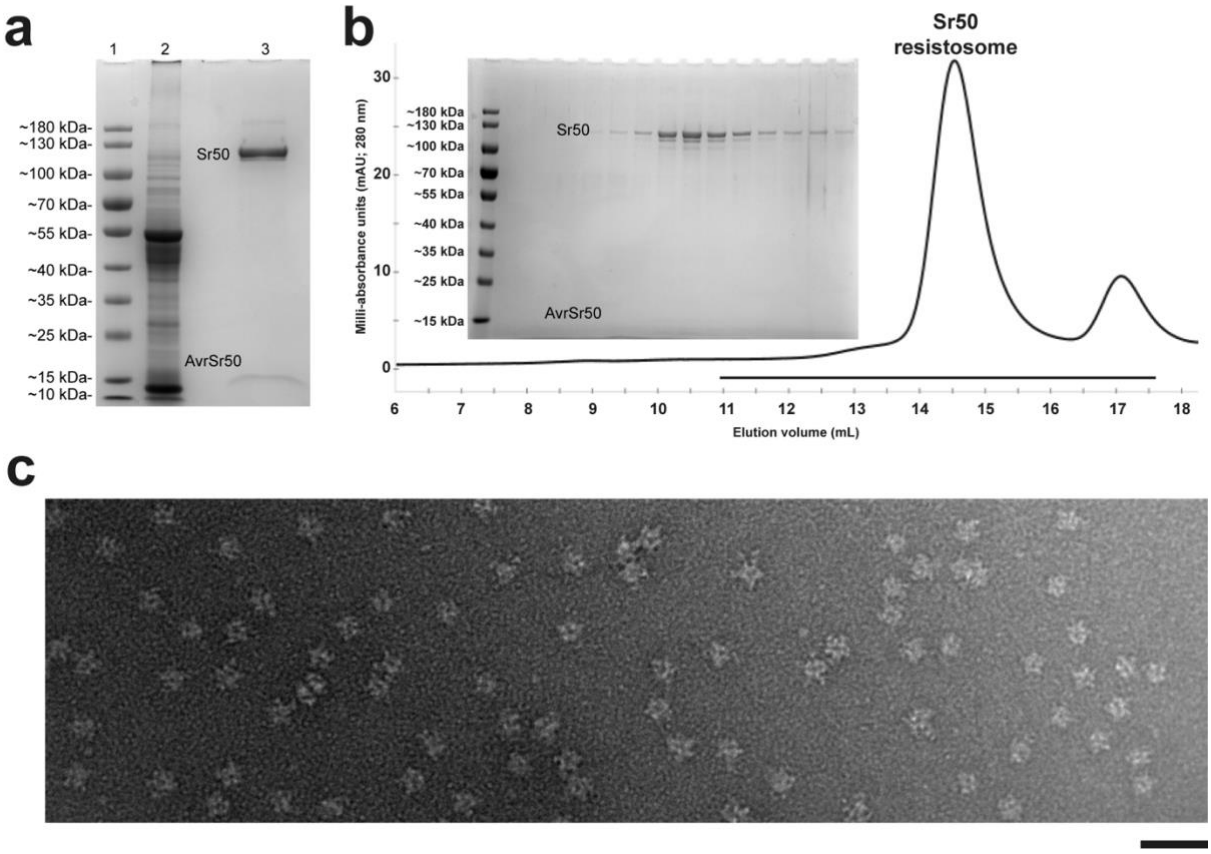

Fig. 3 | Purification and negative staining of the Sr50 resistosome extracted from leaves of *N. benthamiana*. a, CBB-stained SDS PAGE gel of a single-step affinity purification of C-terminal Twin-Strep-HA-tagged Sr50 and untagged AvrSr50. Lane #1: molecular weight ladder. Lane #2: total lysate (5 μL loaded). Lane #3: Enrichment of Sr50 $^{L11E/L15E}$ *via* the C-terminal Twin-Strep-HA tag co-enriches untagged AvrSr50 (45 μL/2.5 mL loaded). **b,** SEC profile of the sample stained in (**a**) displaying the elution peak of the Sr50 at ~14.5 mL. Inset CBB-stained SDS PAGE gel displays fractions eluted along the black line on the x-axis. Low staining intensity of AvrSr50 due to its low molecular weight and inability to bind sufficient CBB. **c,** Negative staining EM micrograph of a diluted sample from the 14.5 mL elution fraction in (**b**) shows pentameric, star-shaped particles. Black line represents 50 nm.

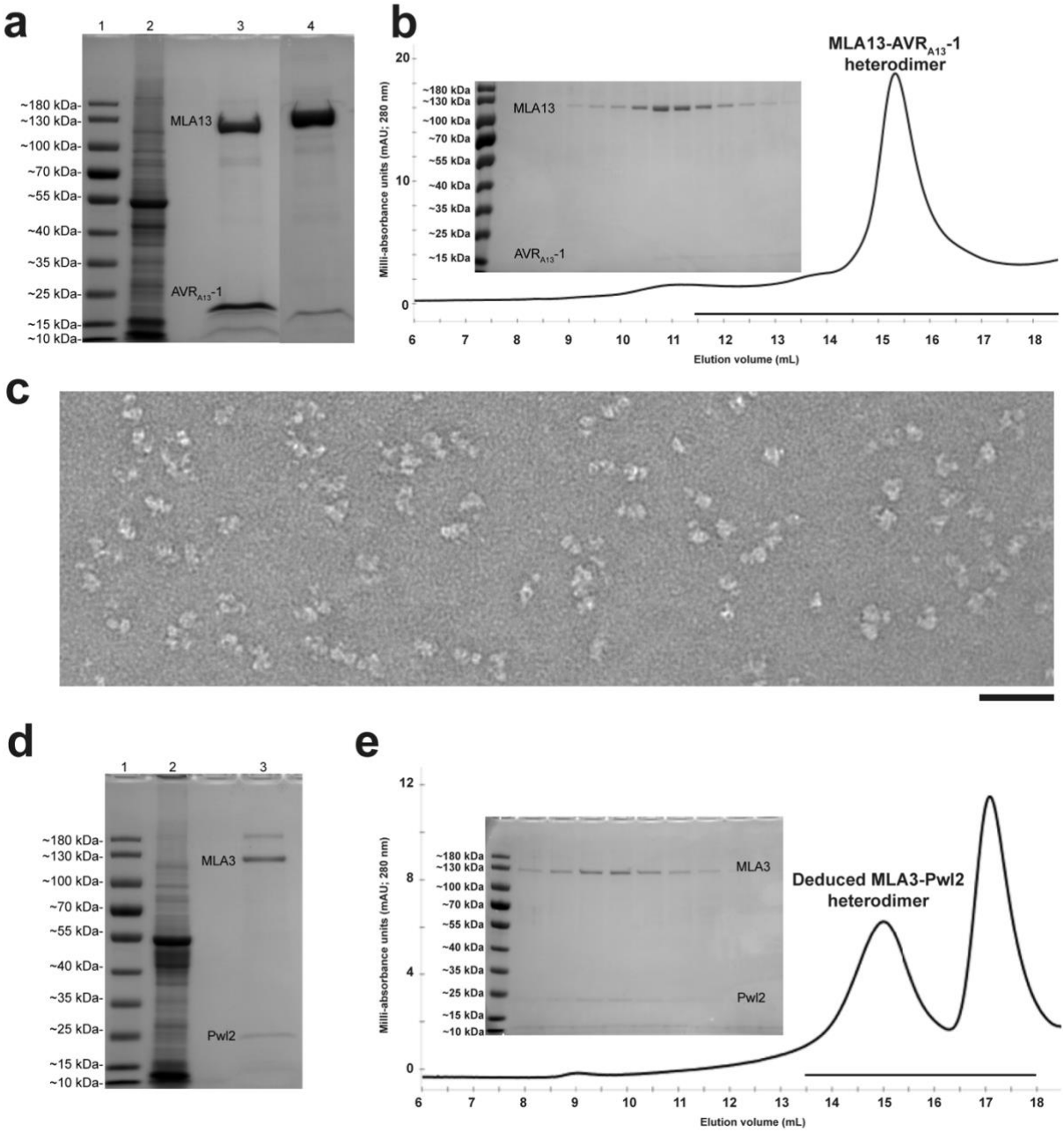

Fig. 4 | Purification and negative staining of the MLA13-AVR$_{A13}$-1 heterodimer and MLA3-Pwl2 heterocomplex extracted from leaves of *N. benthamiana*. a, CBB-stained SDS PAGE gel of a two-step affinity purification of C-terminal Twin-Strep-HA-tagged AVR$_{A13}$-1 and N-terminal GST-tagged MLA13$^{K98E/K100E}$. Lane #1: molecular weight ladder. Lane #2: total lysate (5 μL loaded). Lane #3: Enrichment of AVR$_{A13}$-1 *via* the C-terminal Twin-Strep-HA tag co-enriched MLA13$^{K98E/K100E}$. Lane #4: A second-step affinity purification *via* the N-terminal GST tag on MLA13$^{K98E/K100E}$ sequentially co-enriched AVR$_{A13}$-1, suggesting a 1:1 molar ratio. **b,** SEC profile of the concentrated sample stained in lane #4 of (**a**) displaying the elution peak of the heterodimer at ~15.5 mL. Inset CBB-stained SDS PAGE gel displays fractions eluted along the black line on the x-axis. **c,** Negative staining EM micrograph of a diluted sample from the 15.5 mL elution fraction in (**b**). Black line represents 50 nm. **d,** CBB-stained SDS PAGE gel of a two-step affinity purification of C-terminal Twin-Strep-HA-tagged Pwl2 and N-terminal GST-tagged MLA3$^{K98E/K100E}$. Lane #1: molecular weight ladder. Lane #2: total lysate (5 μL loaded). Lane #3: Enrichment of Pwl2 *via* the C-terminal Twin-Strep-HA tag co-enriched MLA3$^{K98E/K100E}$. **e,** SEC profile of the concentrated sample stained in lane #3 of (**d**) displaying the elution peak of the heterocomplex at ~15 mL. Inset CBB-stained SDS PAGE gel displays fractions eluted along the black line on the x-axis.

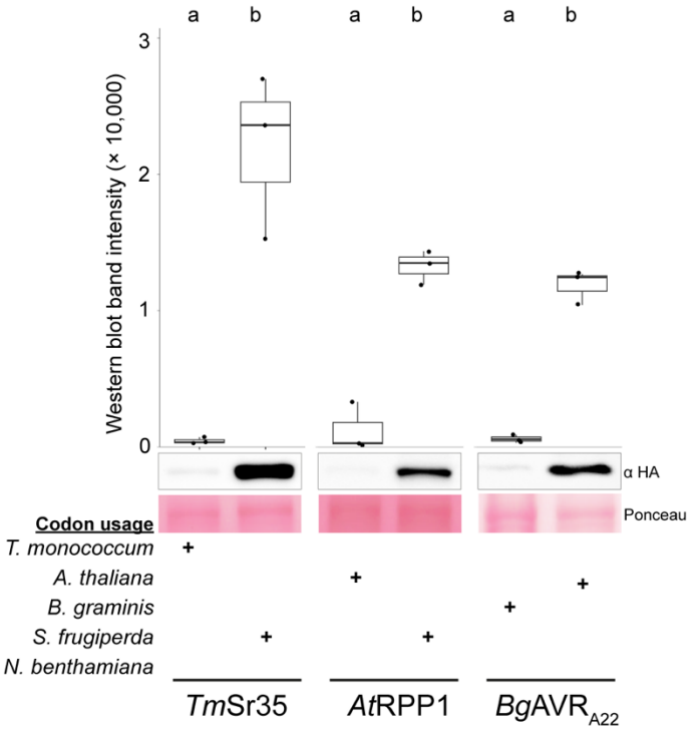

Extended Data Fig. 1 | Codon alteration drastically increases protein yield from transient expression in leaves of *N. benthamiana*. a, Transient expression comparison of native versus codon altered sequences *via* western blot band intensity. All samples were processed using the same method. Three replicates were performed for each treatment. A one-way ANOVA was performed followed by the Tukey's test. Differing letters indicate statistical difference ($p < 0.05$). All replicates and loading controls are reported in Extended Data Fig. 5.

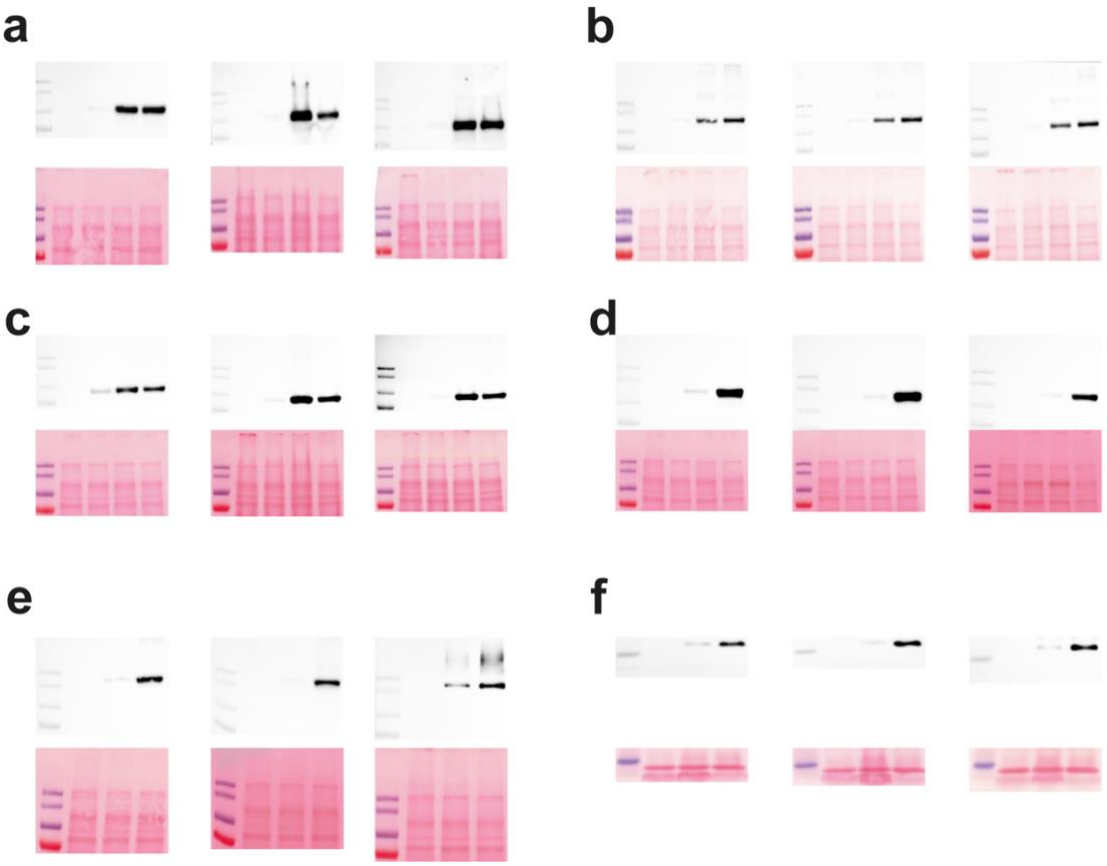

Extended Data Fig. 2 | Replicates of western blot data reported in Fig. 1 and Extended Data Fig. 1 and accompanying Ponceau stained membranes for loading controls. a, MLKL1 replicates. **b,** MLA3 replicates. **c,** SARM1 replicates. **d,** Sr35 replicates. **e,** RPP1 replicates. **f,** AVR_{A22} replicates.

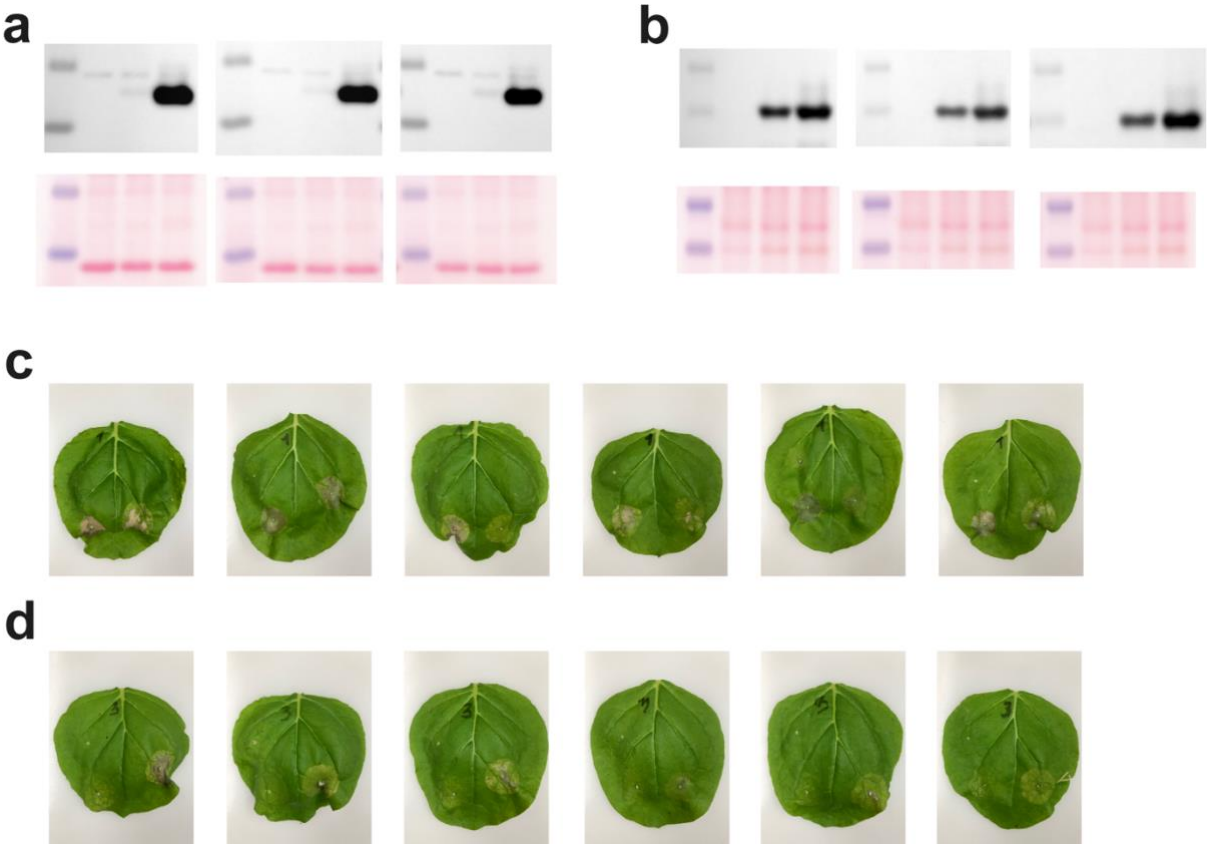

Extended Data Fig. 3 | Replicates of western blot data, accompanying Ponceau stained membranes for loading controls and cell death assays reported in Fig. 1b. a, *Bg*AVR$_{A22}$ replicates. Lane #1: ladder. Lane #2: empty vector. Lane #3: *Bg*AVR$_{A22}$ without signal peptide. Lane #4: *Bg*AVR$_{A22}$ with signal peptide. **b,** *Mo*Pwl2 replicates. Lane #1: ladder. Lane #2: empty vector. Lane #3: Pwl2 without signal peptide. Lane #4: Pwl2 with signal peptide replicates. **c,** Co-expression of *Bg*AVR$_{A22}$ with and without the signal peptide with MLA22-4×MYC tag. Top left corner: empty vector + MLA22-4×MYC. Bottom left corner: *Bg*AVR$_{A22}$ without signal peptide + MLA22-4×MYC. Bottom right corner: *Bg*AVR$_{A22}$ with signal peptide + MLA22-4×MYC. **d,** Co-expression of *Mo*Pwl2 with and without the signal peptide with MLA3-4×MYC tag. Top left corner: empty vector + MLA3-4×MYC. Bottom left corner: *Mo*Pwl2 without signal peptide + MLA3-4×MYC. Bottom right corner: *Mo*Pwl2 with signal peptide + MLA3-4×MYC.

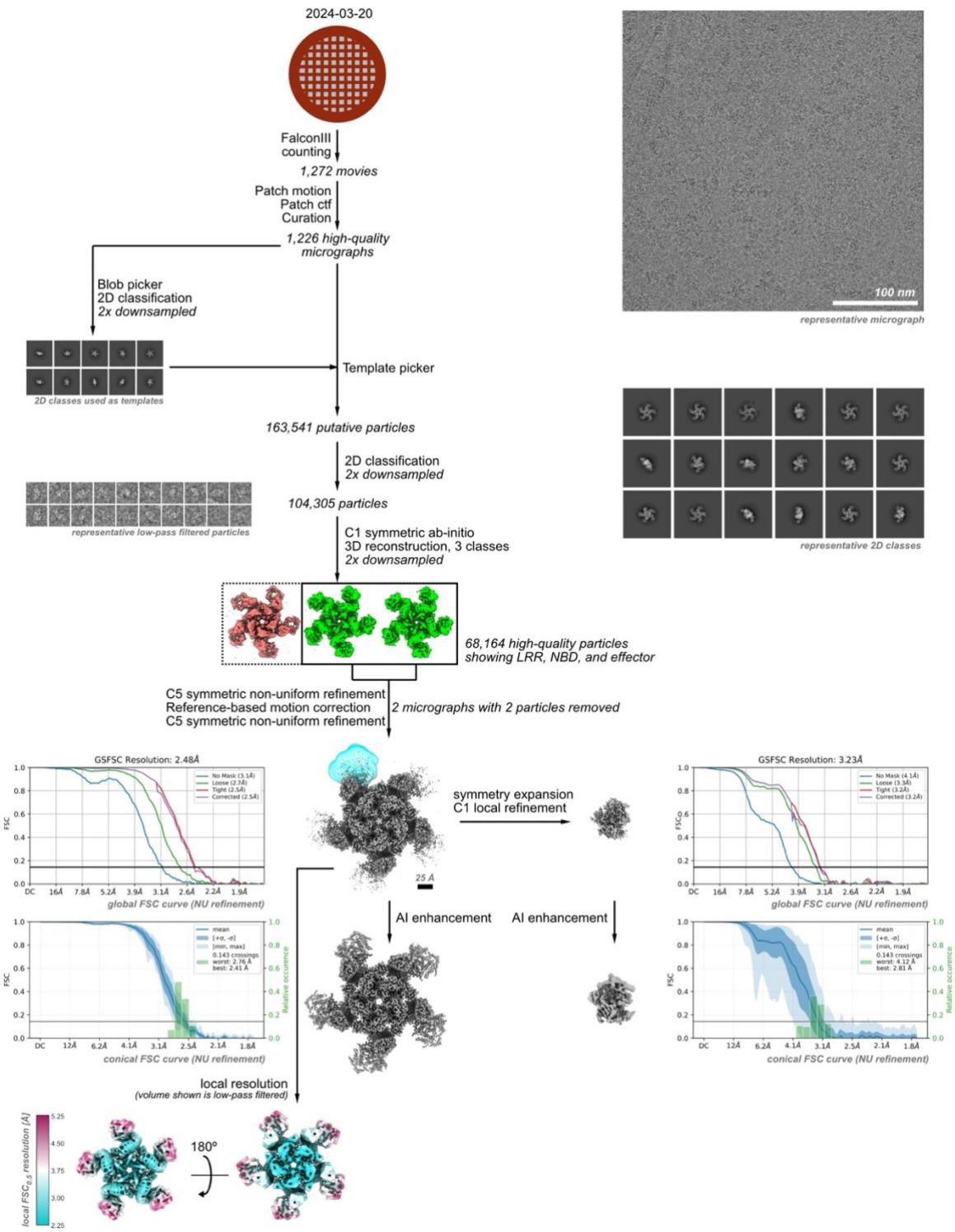

Extended Data Fig. 4 | Workflow of cryo-EM data acquisition and analysis of the Sr35 resistosome. A single dataset was collected on a 300 kV cryo-electron microscope, and movies were selected for low per-frame drift rates, good CTF scores, and low astigmatism. Particles were first picked using a blob picker, and then subjected to unsupervised 2D classification. Representative classes showing protein-like structures were used for a template picker. Detected putative particles were curated using unsupervised 2D classification, selecting for particles with protein-like density and resolutions better than 10 Å. The selected particles were further curated using *ab-initio* reconstruction, sorting them into three distinct populations. From these, all particles contributing to a structure showing clear density for LRR, NBD and effector (shown in green and highlighted by a thicker box outline) were combined and refined in 3D using a non-uniform refinement algorithm applying C5 symmetry and relying on reference-based motion correction, resulting in a map with a uniform resolution of 2.5 Å. To improve the density for the effector protein a local mask was used for a C1 symmetric local refinement after symmetry expansion. For visualisation the maps were further sharpened using DeepEMhancer.

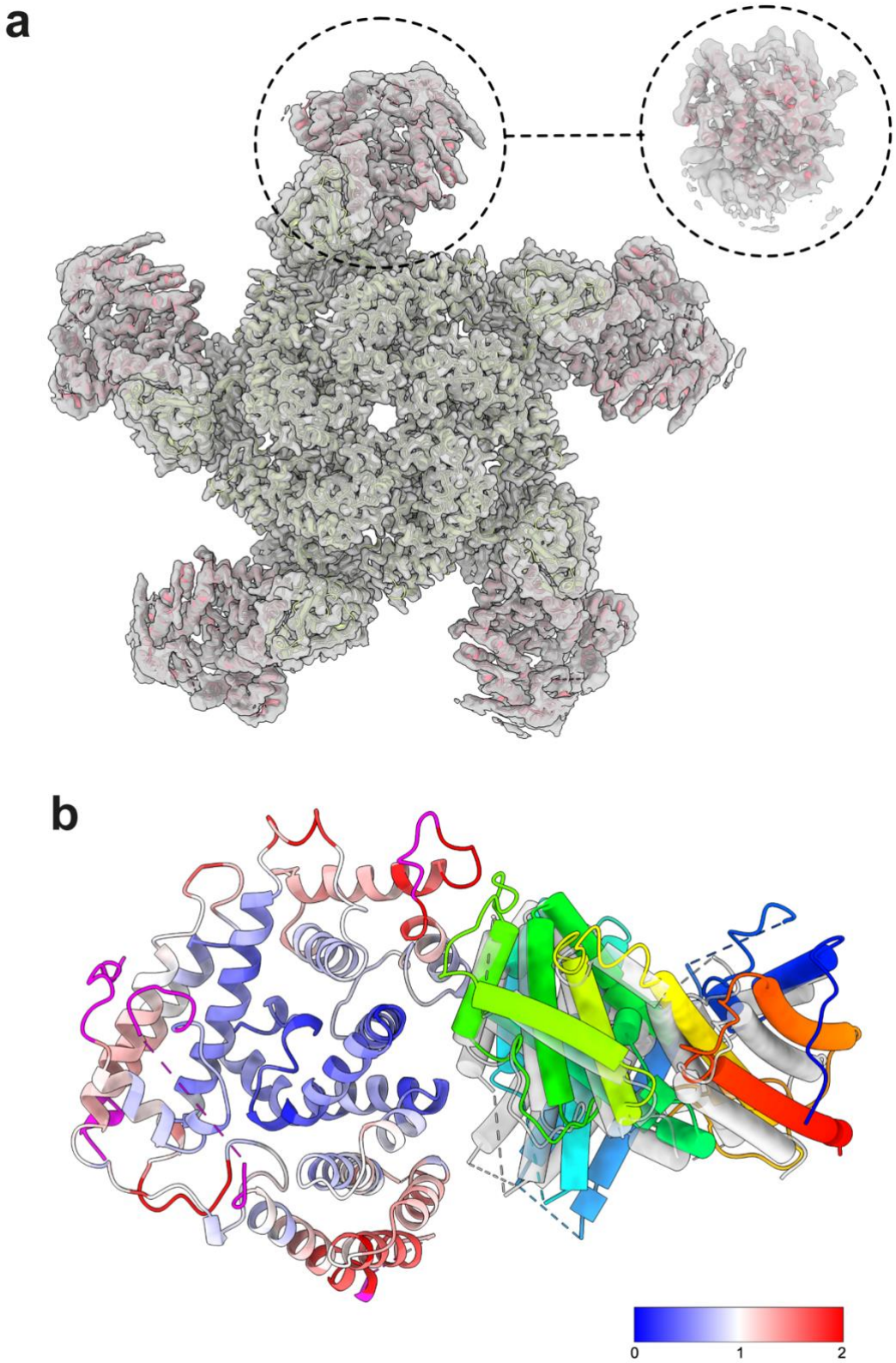

Extended Data Fig. 5 | Comparisons with previously reported structures of the Sr35 resistosome and AvrSr35 homodimer. a, Comparison of our cryo-EM map with the published cryo-EM structure of Sr35 (PDB: 7XE0). Sr35 is shown in green, while AvrSr35 is shown in red. The circular insert shows the fit of AvrSr35 into the map obtained by focussed refinement. **b,** Comparison of the cryo-EM derived atomic model of AvrSr35 with the published crystal structure (PDB: 7XDS). The left subunit is shown in cartoon representation and coloured by RMSD deviation to the published crystal structure. Newly modelled residues are coloured in magenta. The right subunit is shown in a pipes-and-planks representation and coloured in rainbow from N-terminus to C-terminus. To show the 6° difference in the orientation of the subunits in the dimer, the crystal structure is shown in transparent white.

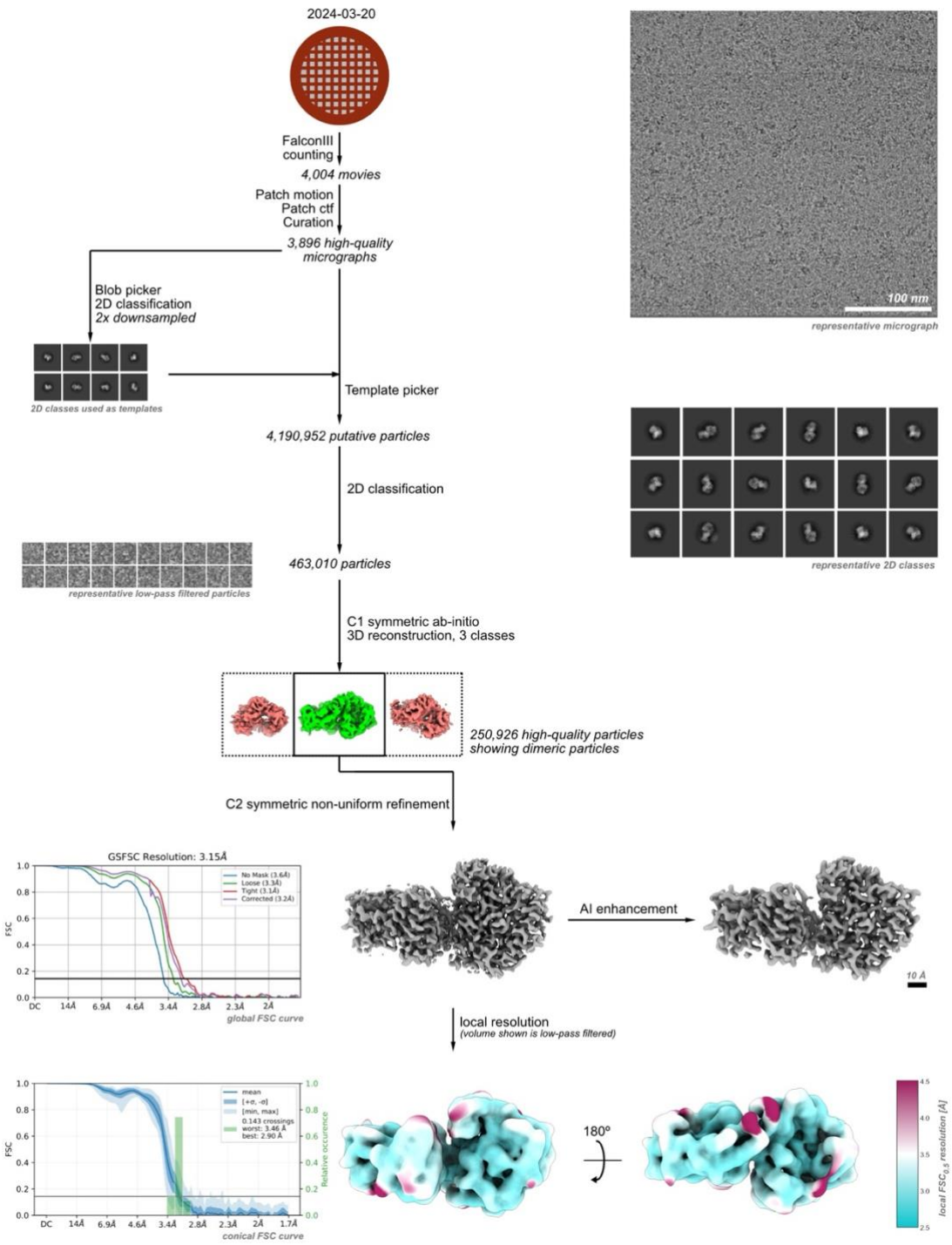

Extended Data Fig. 6 | Workflow of cryo-EM data acquisition and analysis of the AvrSr35 homodimer. A single dataset was collected on a 300 kV cryo-electron microscope, and movies were selected for low per-frame drift rates, good CTF scores, and low astigmatism. Particles were first picked using a blob picker, and then subjected to unsupervised 2D classification. Representative classes showing protein-like structures were used for a template picker. Detected putative particles were curated using unsupervised 2D classification, selecting for particles with protein-like density and resolutions better than 10 Å. The selected particles were further curated using ab-initio reconstruction, sorting them into 3 distinct populations. From these, all particles contributing to a structure showing clearly dimeric particles (shown in green and highlighted by a thicker box outline) were combined and refined in 3D using a non-uniform refinement algorithm applying C2 symmetry, resulting in a map with a uniform resolution of 3.1 Å. For model building the map was further sharpened using DeepEMhancer.

General discussion

Resolving the Sr35 resistosome extends our understanding of heteromeric immunocomplexes from the model system *A. thaliana*'s ZAR1 resistosome to the first cryo-EM structure of a resistosome from a staple crop[43,44]. Our results not only revealed differences but also commonalties between immunocomplexes from highly divergent monocotyledonous and dicotyledonous species. Electrophysiology results suggest that the formation of a Ca^{2+} permeable non-selective ion channel, possibly *via* resistosome pore formation at the plasma membrane, is a conserved cell death-inducing mechanism shared between the two CNL immunocomplexes despite ~150 million years of evolutionary divergence between wheat and Arabidopsis. The lack of resolution of the α1-helix at the N-terminal of Sr35 indeed raises curiosities about its conformation in comparison to that of the ZAR1 resistosome which forms a cone-like structure believed to associate with the plasma membrane[15]. Co-expression of Sr35 and AvrSr35, however, seemingly co-localise at the endoplasmic reticulum, prompting the need for further research into the functional diversity among plant resistosomes[22]. Similarly, the NRC4 resistosome lacks resolution of the α1-helix, questioning the stability of these domains in the absence of a lipid bilayer, e.g. the plasma membrane or endoplasmic reticulum, and how they differ from the ZAR1 resistosome[13]. Alternatively, the substitutions $Sr35^{L15E/L19E}$ and $NRC4^{L9E}$ introduced to abolish cell death activity could contribute to destabilise the CC domain. Although Ca^{2+} influx seem to be a common output of plant resistosome activation, cellular processes downstream of Ca^{2+} influx and of other ions preceding cell death remain poorly understood. Pore formation could simply lead to membrane rupture or cytotoxicity, resulting in cell death. Alternatively, unidentified, downstream Ca2+-binding proteins s may be the *bona fide* executers of the HR response[45]. One candidate is the Ca^{2+} calmodulin binding transcription activator (CAMTA) family for which experimental evidence suggests a function as convergence point for PRR- and NLR-triggered immune responses[46,47]. The pentameric conformation of Sr35 was believed to represent a common principle of plant resistosomes until the recent discovery of the hexamerisation of NRC4, cautioning the field of plant NLR biology to remain open to non-pentameric conformations of activated plant immunoreceptors[13]. However, an important functional difference between NRC4, Sr35 and ZAR1 is that NRC4 acts downstream of sensor NLRs in immune signalling as helper NLR, whereas the latter two are directly or indirectly involved in pathogen recognition (sensor NLRs). The Sr35 resistosome represents the first structure of a CNL immunocomplex in plants that directly binds its cognate effector, AvrSr35, revealing the interface in the LRR domain and prompting us to explore gain/loss of recognition mutants. Using information from the interface, we were able to engineer gain-of-function receptor variants from an orphan Sr35 homolog in wheat to recognise AvrSr35. Although this is a step in the direction of rational structure-guided design of NLRs, it did not yet exemplify broadened effector recognition capability which is thought to result in more durable disease resistance.

Resolving the cryo-EM structure of the barley MLA13-AVR_{A13} heterodimer raises questions regarding the non-pentameric conformation and its physiological relevance. A key question for the future remains whether the stable heterodimer has an immunostimulatory function and represents an intermediate complex on the path to a putative MLA13 resistosome or is a protomer of a disassembled putative MLA13 resistosome. Having successfully purified both the Sr35 and Sr50 resistosome using the same method as the MLA13-AVR_{A13} heterodimer and having tested various cell death-preventing substitutions in the receptor and epitope tag fusions, I conclude

that the lack of a detectable MLA13 resistosome can be explained by its instability and inability to be purified from *N. benthamiana*. If the stable heterodimer represents an intermediate complex, I also conclude that the transition from the intermediate complex to a pentameric resistosome is differentially regulated among different sensor CNLs. Further exploration of the former hypothesis will require introducing alternative substitutions in MLA13 to test if the current substitutions (L11E/L15E and K98E/K100E) result in non-native conformation or complex instability. In support of the latter hypothesis, the wheat CNL Pm2a and its cognate effector AvrPm2 from *Bg* were recently found to require interaction with the wheat zinc finger transcription factor TaZF for mediating cell death and immunity to powdery mildew, prompting the idea that MLA13-AVR_{A13}-mediated immunity may require additional factors or pathways[48]. Moreover, preliminary, unpublished data suggests that some barley CNLs are capable of triggering a cell death response in human HEK293 cells while MLA13-AVR_{A13} cannot, suggesting that additional, plant-specific factors are required for reconstituting cell death in such a heterologous system. Notably, purification and characterization of the MLA3-Pwl2 heterocomplex by size exclusion chromatography suggests an apparent molecular weight indicative of a deduced heterodimer. This suggests the receptor conformation in the MLA13-AVR_{A13} heterodimer may be a common feature of other activated MLA recognition specificities. Clearly, the physiological relevance of activated, non-pentameric CNL heterocomplexes such as the MLA13-AVR_{A13} heterodimer needs to be clarified due to recent discoveries of non-canonical immune complexes such as the NRC4 hexamer[13]. This requires the generation of transgenic barley plants expressing MLA13 with K98E/K100E substitutions from its native promoter and pathogen infection experiments with *Bg* strains containing or lacking AVR_{A13}-1.

Long-standing evidence supporting direct MLA recognition of *Bg* AVR_As is finally verified by the structure of the MLA13-AVR_{A13}-1 heterodimer[27,28]. Moreover, the heterodimer structurally clarifies previous evidence that some AVR_As are recognised by their matching MLAs *via* their basal loops[28,29]. Although resolving the interface of additional MLA-AVR_{As} is required to conclude that basal loop recognition is a common feature of MLA interactions, we hypothesise that receptor targeting of this structurally diversified region of the effector may be to avoid non-target recognition of structurally similar, host RNases resulting in receptor autoactivity. Our mutagenesis and cell death results of the interface also highlights the physiological relevance of AVR_{A13}-1 recognition and finally opened the door to structure-guided design of MLAs for broadened effector recognition. Designing the $MLA7^{L902S}$ gain-of-function mutant to not only recognise AVR_{A13}-1 but also the virulent variant AVR_{A13}-V2 illustrates how a a single base gene edit can be used to broaden effector recognition capabilities to a non-cognate effector and a virulence effector. AVR_{A13}-1 is expressed in a worldwide collection of characterised *Bg* strains, extending the utility of the engineered receptor and its capability to recognise effector variants that escape receptor recognition in the field. Additionally, the minimalistic alteration of using a single base edit is potentially desirable in the context of legislation of genetically modified plants in some jurisdictions. Before extending such findings to the field, the $MLA7^{L902S}$ mutant needs to be tested for gain of immunity through the generation of transgenic barley lines followed by pathogen infection assays.

Extension of our findings in this thesis to future research questions such as resolving the cryo-EM structures of additional MLA-AVR_A pairs is facilitated through the development of a robust and versatile protocol for purifying transiently expressed proteins from leaves of *N. benthamiana.* Our protocol reveals basic parameters that

are essential not only for high *in planta* expression but also for formulating conditions that are suitable for maximising protein yield while maintaining sample purity. While predictive tools such as AlphaFold are gaining popularity, resolving experimental structures remains indispensable for not only answering biological questions but also for shaping the utility and veracity of modelling algorithms.

General references

1 Jones, J. D. & Dangl, J. L. The plant immune system. *Nature* **444**, 323-329 (2006). https://doi.org/10.1038/nature05286

2 Hao, G., Tiley, H. & McCormick, S. Chitin Triggers Tissue-Specific Immunity in Wheat Associated With Fusarium Head Blight. *Front Plant Sci* **13**, 832502 (2022). https://doi.org/10.3389/fpls.2022.832502

3 Yuan, M., Ngou, B. P. M., Ding, P. & Xin, X. F. PTI-ETI crosstalk: an integrative view of plant immunity. *Curr Opin Plant Biol* **62**, 102030 (2021). https://doi.org/10.1016/j.pbi.2021.102030

4 Jones, J. D., Vance, R. E. & Dangl, J. L. Intracellular innate immune surveillance devices in plants and animals. *Science* **354** (2016). https://doi.org/10.1126/science.aaf6395

5 Saur, I. M. L., Panstruga, R. & Schulze-Lefert, P. NOD-like receptor-mediated plant immunity: from structure to cell death. *Nature Reviews Immunology* **21**, 305-318 (2020). https://doi.org/10.1038/s41577-020-00473-z

6 Kroj, T., Chanclud, E., Michel-Romiti, C., Grand, X. & Morel, J.-B. Integration of decoy domains derived from protein targets of pathogen effectors into plant immune receptors is widespread. *New Phytologist* **210**, 618-626 (2016). https://doi.org/https://doi.org/10.1111/nph.13869

7 Jubic, L. M., Saile, S., Furzer, O. J., El Kasmi, F. & Dangl, J. L. Help wanted: helper NLRs and plant immune responses. *Current Opinion in Plant Biology* **50**, 82-94 (2019). https://doi.org/https://doi.org/10.1016/j.pbi.2019.03.013

8 Feehan, J. M., Castel, B., Bentham, A. R. & Jones, J. D. G. Plant NLRs get by with a little help from their friends. *Current Opinion in Plant Biology* **56**, 99-108 (2020). https://doi.org/https://doi.org/10.1016/j.pbi.2020.04.006

9 Xi, Y., Cesari, S. & Kroj, T. Insight into the structure and molecular mode of action of plant paired NLR immune receptors. *Essays Biochem* **66**, 513-526 (2022). https://doi.org/10.1042/ebc20210079

10 Wang, J. *et al.* Reconstitution and structure of a plant NLR resistosome conferring immunity. *Science* **364** (2019). https://doi.org/10.1126/science.aav5870

11 Martin, R. *et al.* Structure of the activated ROQ1 resistosome directly recognizing the pathogen effector XopQ. *Science* **370**, eabd9993 (2020). https://doi.org/doi:10.1126/science.abd9993

12 Ma, S. *et al.* Direct pathogen-induced assembly of an NLR immune receptor complex to form a holoenzyme. *Science* **370** (2020). https://doi.org/10.1126/science.abe3069

13 Liu, F. *et al.* Activation of the helper NRC4 immune receptor forms a hexameric resistosome. *Cell* (2024). https://doi.org/10.1016/j.cell.2024.07.013

14 Wang, J. *et al.* Ligand-triggered allosteric ADP release primes a plant NLR complex. *Science* **364** (2019). https://doi.org/10.1126/science.aav5868

15 Bi, G. *et al.* The ZAR1 resistosome is a calcium-permeable channel triggering plant immune signaling. *Cell* **184**, 3528-3541.e3512 (2021). https://doi.org/10.1016/j.cell.2021.05.003

16 Ma, S. *et al.* Oligomerization-mediated autoinhibition and cofactor binding of a plant NLR. *Nature* (2024). https://doi.org/10.1038/s41586-024-07668-7

17 Edae, E. A. *et al.* The genetics of Ug99 stem rust resistance in spring wheat variety 'Linkert'. *Front Plant Sci* **15**, 1343148 (2024). https://doi.org/10.3389/fpls.2024.1343148
18 Karelov, A. *et al.* Wheat Genes Associated with Different Types of Resistance against Stem Rust (Puccinia graminis Pers.). *Pathogens* **11** (2022). https://doi.org/10.3390/pathogens11101157
19 Upadhyaya, N. M. *et al.* Genomics accelerated isolation of a new stem rust avirulence gene-wheat resistance gene pair. *Nat Plants* **7**, 1220-1228 (2021). https://doi.org/10.1038/s41477-021-00971-5
20 Outram, M. A. *et al.* AvrSr27 is a zinc-bound effector with a modular structure important for immune recognition. *New Phytol* **243**, 314-329 (2024). https://doi.org/10.1111/nph.19801
21 Ortiz, D. *et al.* The stem rust effector protein AvrSr50 escapes Sr50 recognition by a substitution in a single surface-exposed residue. *New Phytol* **234**, 592-606 (2022). https://doi.org/10.1111/nph.18011
22 Salcedo, A. *et al.* Variation in the AvrSr35 gene determines Sr35 resistance against wheat stem rust race Ug99. *Science* **358**, 1604-1606 (2017). https://doi.org/10.1126/science.aao7294
23 Arndell, T. *et al.* Pooled effector library screening in protoplasts rapidly identifies novel Avr genes. *Nat Plants* **10**, 572-580 (2024). https://doi.org/10.1038/s41477-024-01641-y
24 Pedersen, C. *et al.* Structure and evolution of barley powdery mildew effector candidates. *BMC Genomics* **13**, 694 (2012). https://doi.org/10.1186/1471-2164-13-694
25 Seeholzer, S. *et al.* Diversity at the Mla powdery mildew resistance locus from cultivated barley reveals sites of positive selection. *Mol Plant Microbe Interact* **23**, 497-509 (2010). https://doi.org/10.1094/mpmi-23-4-0497
26 Lu, X. *et al.* Allelic barley MLA immune receptors recognize sequence-unrelated avirulence effectors of the powdery mildew pathogen. *Proceedings of the National Academy of Sciences* **113** (2016). https://doi.org/10.1073/pnas.1612947113
27 Saur, I. M. L. *et al.* Multiple pairs of allelic MLA immune receptor-powdery mildew AVRA effectors argue for a direct recognition mechanism. *eLife* **8** (2019). https://doi.org/10.7554/eLife.44471
28 Bauer, S. *et al.* The leucine-rich repeats in allelic barley MLA immune receptors define specificity towards sequence-unrelated powdery mildew avirulence effectors with a predicted common RNase-like fold. *PLOS Pathogens* **17** (2021). https://doi.org/10.1371/journal.ppat.1009223
29 Cao, Y. *et al.* Structural polymorphisms within a common powdery mildew effector scaffold as a driver of coevolution with cereal immune receptors. *Proceedings of the National Academy of Sciences* **120** (2023). https://doi.org/10.1073/pnas.2307604120
30 Bettgenhaeuser, J. *et al.* The barley immune receptor Mla recognizes multiple pathogens and contributes to host range dynamics. *Nat Commun* **12**, 6915 (2021). https://doi.org/10.1038/s41467-021-27288-3
31 Brabham, H. J. *et al.* Barley MLA3 recognizes the host-specificity effector Pwl2 from Magnaporthe oryzae. *Plant Cell* **36**, 447-470 (2024). https://doi.org/10.1093/plcell/koad266

32 Zdrzałek, R. *et al.* Bioengineering a plant NLR immune receptor with a robust binding interface toward a conserved fungal pathogen effector. *Proc Natl Acad Sci U S A* **121**, e2402872121 (2024). https://doi.org/10.1073/pnas.2402872121
33 Leng, Y. *et al.* A barley MLA receptor is targeted by a non-ribosomal peptide effector of the necrotrophic spot blotch fungus for disease susceptibility. *bioRxiv*, 2023.2012.2013.571418 (2023). https://doi.org/10.1101/2023.12.13.571418
34 Liu, Y. *et al.* A designer rice NLR immune receptor confers resistance to the rice blast fungus carrying noncorresponding avirulence effectors. *Proceedings of the National Academy of Sciences* **118**, e2110751118 (2021). https://doi.org/doi:10.1073/pnas.2110751118
35 Cesari, S. *et al.* New recognition specificity in a plant immune receptor by molecular engineering of its integrated domain. *Nature Communications* **13**, 1524 (2022). https://doi.org/10.1038/s41467-022-29196-6
36 Zhang, X. *et al.* The effector recognition by synthetic sensor NLR receptors requires the concerted action of multiple interfaces within and outside the integrated domain. *bioRxiv*, 2022.2008.2017.504349 (2022). https://doi.org/10.1101/2022.08.17.504349
37 Maidment, J. H. R. *et al.* Effector target-guided engineering of an integrated domain expands the disease resistance profile of a rice NLR immune receptor. *eLife* **12**, e81123 (2023). https://doi.org/10.7554/eLife.81123
38 Zhang, X. *et al.* The synthetic NLR RGA5HMA5 requires multiple interfaces within and outside the integrated domain for effector recognition. *Nature Communications* **15**, 1104 (2024). https://doi.org/10.1038/s41467-024-45380-2
39 De la Concepcion, J. C. *et al.* Polymorphic residues in rice NLRs expand binding and response to effectors of the blast pathogen. *Nature Plants* **4**, 576-585 (2018). https://doi.org/10.1038/s41477-018-0194-x
40 De la Concepcion, J. C. *et al.* Protein engineering expands the effector recognition profile of a rice NLR immune receptor. *eLife* **8**, e47713 (2019). https://doi.org/10.7554/eLife.47713
41 Gómez De La Cruz, D., Zdrzałek, R., Banfield, M. J., Talbot, N. J. & Moscou, M. J. Molecular mimicry of a pathogen virulence target by a plant immune receptor. *bioRxiv*, 2024.2007.2026.605320 (2024). https://doi.org/10.1101/2024.07.26.605320
42 Tamborski, J., Seong, K., Liu, F., Staskawicz, B. J. & Krasileva, K. V. Altering Specificity and Autoactivity of Plant Immune Receptors Sr33 and Sr50 Via a Rational Engineering Approach. *Mol Plant Microbe Interact* **36**, 434-446 (2023). https://doi.org/10.1094/mpmi-07-22-0154-r
43 Zhao, Y. B. *et al.* Pathogen effector AvrSr35 triggers Sr35 resistosome assembly via a direct recognition mechanism. *Sci Adv* **8**, eabq5108 (2022). https://doi.org/10.1126/sciadv.abq5108
44 Förderer, A. *et al.* A wheat resistosome defines common principles of immune receptor channels. *Nature* **610**, 532-539 (2022). https://doi.org/10.1038/s41586-022-05231-w
45 Köster, P., DeFalco, T. A. & Zipfel, C. Ca(2+) signals in plant immunity. *Embo j* **41**, e110741 (2022). https://doi.org/10.15252/embj.2022110741
46 Xiao, P., Feng, J. W., Zhu, X. T. & Gao, J. Evolution Analyses of CAMTA Transcription Factor in Plants and Its Enhancing Effect on Cold-tolerance. *Front Plant Sci* **12**, 758187 (2021). https://doi.org/10.3389/fpls.2021.758187

47 Jacob, F. *et al.* A dominant-interfering camta3 mutation compromises primary transcriptional outputs mediated by both cell surface and intracellular immune receptors in Arabidopsis thaliana. *New Phytologist* **217**, 1667-1680 (2018). https://doi.org/https://doi.org/10.1111/nph.14943

48 Manser, B. *et al.* Wheat zinc finger protein TaZF interacts with both the powdery mildew AvrPm2 protein and the corresponding wheat Pm2a immune receptor. *Plant Commun* **5**, 100769 (2024). https://doi.org/10.1016/j.xplc.2023.100769

Acknowledgments

I would like to express my deepest gratitude to my friends and family for their unwavering love and support throughout this journey. I am especially thankful to Prof. Dr. Schulze-Lefert for his steadfast support during my studies and his remarkable dedication to the success of his students, postdoctoral fellows, and the broader scientific community. I am also deeply grateful to Prof. Dr. Jane Parker and Prof. Dr. Jijie Chai for their guidance and support as members of my Thesis Advisory Committee (TAC). My sincere thanks go to everyone at the MPIPZ and the entire PSL department for their continuous support. The achievements in this thesis are a testament to the incredible people who have inspired and supported me.

Erklärung zur Dissertation
gemäß der Promotionsordnung vom 12. März 2020

Diese Erklärung muss in der Dissertation enthalten sein.
(*This version must be included in the doctoral thesis*)

„Hiermit versichere ich an Eides statt, dass ich die vorliegende Dissertation selbstständig und ohne die Benutzung anderer als der angegebenen Hilfsmittel und Literatur angefertigt habe. Alle Stellen, die wörtlich oder sinngemäß aus veröffentlichten und nicht veröffentlichten Werken dem Wortlaut oder dem Sinn nach entnommen wurden, sind als solche kenntlich gemacht. Ich versichere an Eides statt, dass diese Dissertation noch keiner anderen Fakultät oder Universität zur Prüfung vorgelegen hat; dass sie - abgesehen von unten angegebenen Teilpublikationen und eingebundenen Artikeln und Manuskripten - noch nicht veröffentlicht worden ist sowie, dass ich eine Veröffentlichung der Dissertation vor Abschluss der Promotion nicht ohne Genehmigung des Promotionsausschusses vornehmen werde. Die Bestimmungen dieser Ordnung sind mir bekannt. Darüber hinaus erkläre ich hiermit, dass ich die Ordnung zur Sicherung guter wissenschaftlicher Praxis und zum Umgang mit wissenschaftlichem Fehlverhalten der Universität zu Köln gelesen und sie bei der Durchführung der Dissertation zugrundeliegenden Arbeiten und der schriftlich verfassten Dissertation beachtet habe und verpflichte mich hiermit, die dort genannten Vorgaben bei allen wissenschaftlichen Tätigkeiten zu beachten und umzusetzen. Ich versichere, dass die eingereichte elektronische Fassung der eingereichten Druckfassung vollständig entspricht."

Teilpublikationen:
Förderer, A. et al. A wheat resistosome defines common principles of immune receptor channels. Nature 610, 532-539 (2022). https://doi.org/10.1038/s41586-022-05231-w
Lawson, A. W. et al. The barley MLA13-AVR_{A13} heterodimer reveals principles for immunoreceptor recognition of RNase-like powdery mildew effectors. bioRxiv, 2024.2007.2014.603419 (2024). https://doi.org/10.1101/2024.07.14.603419
Lawson, A. W. et al. A versatile protocol for purifying recombinant proteins from Nicotiana benthamiana. (to be uploaded on bioRxiv).

Datum, Name und Unterschrift

13.08.2024, Aaron Lawson,

Declaration for the doctoral thesis (dissertation)
according to the doctoral regulations published 12th March 2020

Non-official English translation of the "Erklärung zur Dissertation"
(*The German version must be included in the doctoral thesis*)

"I hereby declare that I have completed the present dissertation independently and without the use of any aids or literature other than those referred to. All passages that have been taken, either literally or in sense, from published and unpublished works, are marked as such. I declare that this dissertation has not been submitted to any other faculty or university; that - apart from the partial publications and included articles and manuscripts listed below - it has not yet been published, and that I will not publish the dissertation before completing my doctorate without the permission of the PhD Committee. I am aware of the terms of the doctoral regulations. In addition, I hereby declare that I am aware of the "Regulations for Safeguarding Good Scientific Practice and Dealing with Scientific Misconduct" of the University of Cologne, and that I have observed them during the work on the thesis project and the written doctoral thesis. I hereby commit myself to observe and implement the guidelines mentioned there in all scientific activities. I assure that the submitted electronic version is identical to the submitted printed version".

Partial publications of the thesis:
Förderer, A. et al. A wheat resistosome defines common principles of immune receptor channels. Nature 610, 532-539 (2022). https://doi.org/10.1038/s41586-022-05231-w
Lawson, A. W. et al. The barley MLA13-AVR_{A13} heterodimer reveals principles for immunoreceptor recognition of RNase-like powdery mildew effectors. bioRxiv, 2024.2007.2014.603419 (2024). https://doi.org/10.1101/2024.07.14.603419
Lawson, A. W. et al. A versatile protocol for purifying recombinant proteins from Nicotiana benthamiana. (to be uploaded on bioRxiv).

Date, name, and signature
13.08.2024, Aaron Lawson,

Erklärung zum Gesuch um Zulassung zur Promotion
gemäß der Promotionsordnung vom 12. März 2020

1. Zugänglichkeit von Daten und Materialien

Die Dissertation beinhaltet die Gewinnung von Primärdaten oder die Analyse solcher Daten oder die Reproduzierbarkeit der in der Dissertation dargestellten Ergebnisse setzt die Verfügbarkeit von Datenanalysen, Versuchsprotokollen oder Probenmaterial voraus.

☐ Trifft nicht zu
☑ Trifft zu.
In der Dissertation ist dargelegt wie diese Daten und Materialien gesichert und zugänglich sind (entsprechend den Vorgaben des Fachgebiets beziehungsweise der Betreuerin oder des Betreuers).

2. Frühere Promotionsverfahren

Ich habe bereits einen Doktortitel erworben oder ehrenhalber verliehen bekommen.
Oder: Für mich ist an einer anderen Fakultät oder Universität ein Promotionsverfahren eröffnet worden, aber noch nicht abgeschlossen.
Oder: Ich bin in einem Promotionsverfahren gescheitert.
☑ Trifft nicht zu
☐ Zutreffend
Erläuterung:

3. Straftat

Ich bin <u>nicht</u> zu einer vorsätzlichen Straftat verurteilt worden, bei deren Vorbereitung oder Begehung der Status einer Doktorandin oder eines Doktoranden missbraucht wurde.

Ich versichere, alle Angaben wahrheitsgemäß gemacht zu haben.

Datum	Name	Unterschrift
13.08.2024	Aaron Lawson	

Declaration on the application for admission to the doctoral examinations
according to the doctoral regulations published 12th March 2020

1. Accessibility of data and materials

The dissertation involves the acquisition of primary data or the analysis of such data or the reproducibility of the results presented in the dissertation requires the availability of data analyses, experimental protocols or sample material.

☐ not applicable

☑ applicable
I have described in the dissertation how these data and materials are secured and accessible (according to the specifications of the subject area or supervisor).

2. Previous doctoral examinations

I have already obtained a doctorate or been awarded an honorary doctoral degree.

Or: A doctoral examination has been opened at another faculty or university, but not yet completed.

Or: I have failed in a doctoral examination.

☑ not applicable

☐ applicable
explanatory note:

3. Criminal offense

I have <u>not</u> been convicted of a deliberate criminal offence in the preparation or commission of which the status as a doctoral candidate was abused.

I declare that all information provided is truthful.

Date	Name	Signature
13.08.2024	Aaron Lawson	